# ADVANCED SIGNAL PROCESSING METHODS FOR SATELLITE RADIOMETER CHANNELS

SSEC NO.75.07.S1

A REPORT

from the space science and engineering center
the university of wisconsin-madison
madison, wisconsin

# ADVANCED SIGNAL PROCESSING METHODS FOR SATELLITE RADIOMETER CHANNELS

Final Report on
NOAA Grant 3-35372 for GOES Systems Studies
Task A

by

F. G. Stremler
Seshadri Iyengar
Amarnath Sethuraman

Space Science and Engineering Center
The University of Wisconsin
Madison, Wisconsin

1 July 1975

Table of Contents

# Chapter 1

## INTRODUCTION

This report describes work completed on Grant 3-35372, Task A, in the 1974-1975 fiscal year.

Work in progress in the 1973-1974 year was continued on the use of the 8x8 Walsh transform for the encoding of visual channel data of a geostationary orbiting experimental satellite. Emphasis has been placed on the use of the data for meteorological purposes using both visual and computer interpretation. Only those methods which are judged to be readily adaptable to satellite hardware within the very near future are considered in these studies.

Chapter 4 presents work done on the choices of encoding the 8x8 Walsh transform array and their effect on performance. Attention has been paid to the preservation of pertinent detail in the various types of imagery important to meteorological interpretations as well as to those methods applicable to a mechanization of this approach.

Chapter 3 presents work done on the investigations of the use of symmetry classifications in Walsh transform encoding. Both the theoretical considerations giving rise to symmetry conditions and the results of forced symmetry are given.

The results of both Chapters 3 and 4 are supported with computer results and photographic reconstructions resulting from computer simulations. This portion of the work is now essentially complete.

Chapter 2 presents work done on the Advanced Very High Resolution Radiometer (AVHRR) problem for Tiros N. An approximation is made to the given MTF data for the radiometer. From this an instantaneous field of

view (IFOV) is defined. Bounds on the optimum performance for estimating step radiance changes are derived assuming a step radiance level change and a S/N ratio normalized to the step change. Some work on algorithms for an estimator is also included.

Two papers prepared for external publication based on our past work are included in the appendices.

## Chapter 2

## ESTIMATION OF RADIANCE STEP SIZE WITHIN A LIMITED IFOV FOR AN AVHRR

Development of radiometers with greatly increased spatial resolution, particularly in the infrared, raises questions on the estimation of peak detected radiance levels within a restricted number of instantaneous fields of view (IFOV). Therefore an investigative effort has been directed toward the estimation of the peak detected radiance value given a very restricted time (or spatial) limited observation interval. An objective of this study is that if given the net modulation transfer function (MTF) of the scanner system and the signal-to-noise ratio , how well can the peak value be estimated from measurements within only one or two IFOV's. We assume here that the radiometer has been viewing a long uniform cloud deck and suddenly encounters a clear and complete break in the cloud deck. Later approaches can take such effects as cloud layers, cloud edges, etc. into account in the analyses.

This work is directed specifically to the known requirements for the TIROS N spacecraft. Specifications of TIROS N which are pertinent to this work are listed in Table 2.1 [from GSFC Specifications, July 1974]. A conversion chart based on these specifications and relating spatial frequency at the subsatellite point to the satellite scanner frequency is shown in Figure 2.1.

Table 2.1

AVHRR Specifications for TIROS N

| | |
|---|---|
| Nominal orbit: | circular, altitude of 450 ± 50 n mi |
| Scan system rotation rate: | 360 rpm |
| Radiometer resolution (IFOV): | 0.59 n mi @subsatellite point |
| Quantizing accuracy: | 10-bit (1:1024) |
| Max. sampling rate/channel | 40 kHz |
| Max. step overshoot: | 2%, with less than one cycle "ringing" |
| Modulation Transfer Function (MTF) | |
| for specified subsatellite target size: | 1.00 @11.8 n mi , 0.75 @1.18 n mi |
| | 0.50 @0.88 n mi, 0.30 @0.59 n mi |
| Min. target contrast for 0.59 n mi resolution: | 30:1 |
| Max. radiance input | 80-100% Albedo |

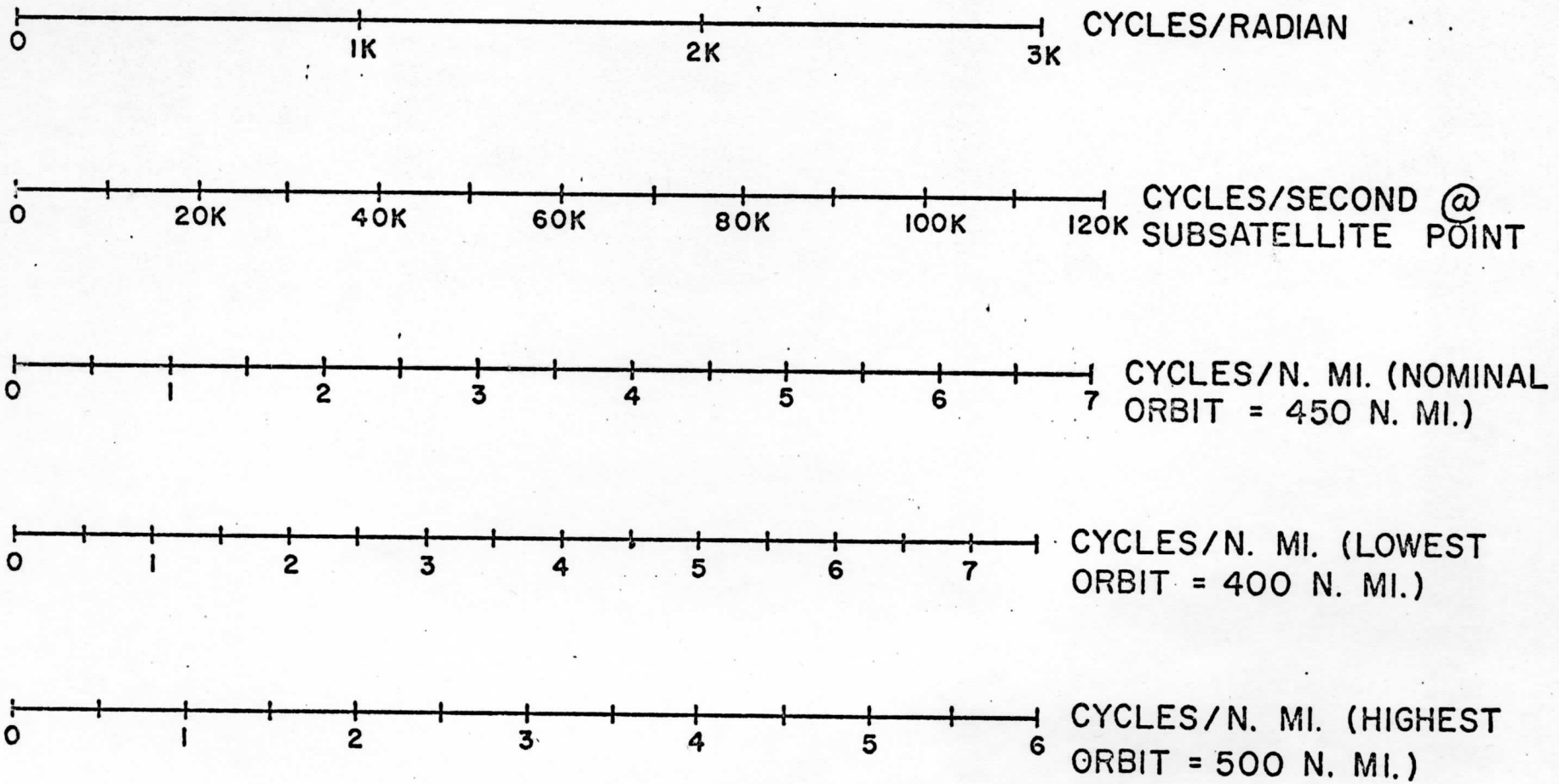


Figure 2.1 Conversion Chart of TIROS N Spectral Data
(Note: subsatellite point assumed with a satellite scanner angular rate of 360 rpm)

The problem described in the preceding paragraphs is basically a problem in the dynamic (transient) behavior of the scanner response. It is complicated by the fact that the observable data is sampled and limited by the MTF of the system. A model for simulation of the overall problem is shown in Figure 2.2. The detector noise is assumed to be a zero-mean Gaussian white noise source with a specified variance. Aperture and optics effects are restricted to those described by the MTF, and cloud edge effects and transmission noise are second-order effects and can be neglected in a first approach to the problem.

Because the data is sampled, a pre-sampling filter is used prior to the sampling operation to reduce the effects of spectral fold-over or aliasing.. This filtering operation will have phase as well as magnitude effects on the spectral components of the signal whereas the MTF will weight the magnitudes only. Therefore we begin by considering several different pre-sampling filters and then the effects of the required MTF will be similar to a second filter placed in cascade with the pre-sampling filter.

Let the frequency transfer function of the pre-sampling filter be $H(\omega)$. The impulse response of the filter is the inverse Fourier transform of $H(\omega)$:

$$h(t) = F^{-1}\{H(\omega)\}$$

$$h(t) = \frac{1}{2\pi}\int_{-\infty}^{\infty} H(\omega)\exp(jt\omega)d\omega \qquad (2.1)$$

It is assumed that $H(\omega)$ describes a low pass filter.

The frequency at which $H(\omega)$ is down from $H(0)$ by 3 dB is labelled as the -3dB bandwidth, B. The rise time, $t_r$, of the system response is that time required for the output to go from 10% to 90% of an output level change resulting from a step input. For low pass filters of order greater than second order, a fairly good approximation to the rise time is:

$$t_r \approx (2B)^{-1} \qquad (2.2)$$

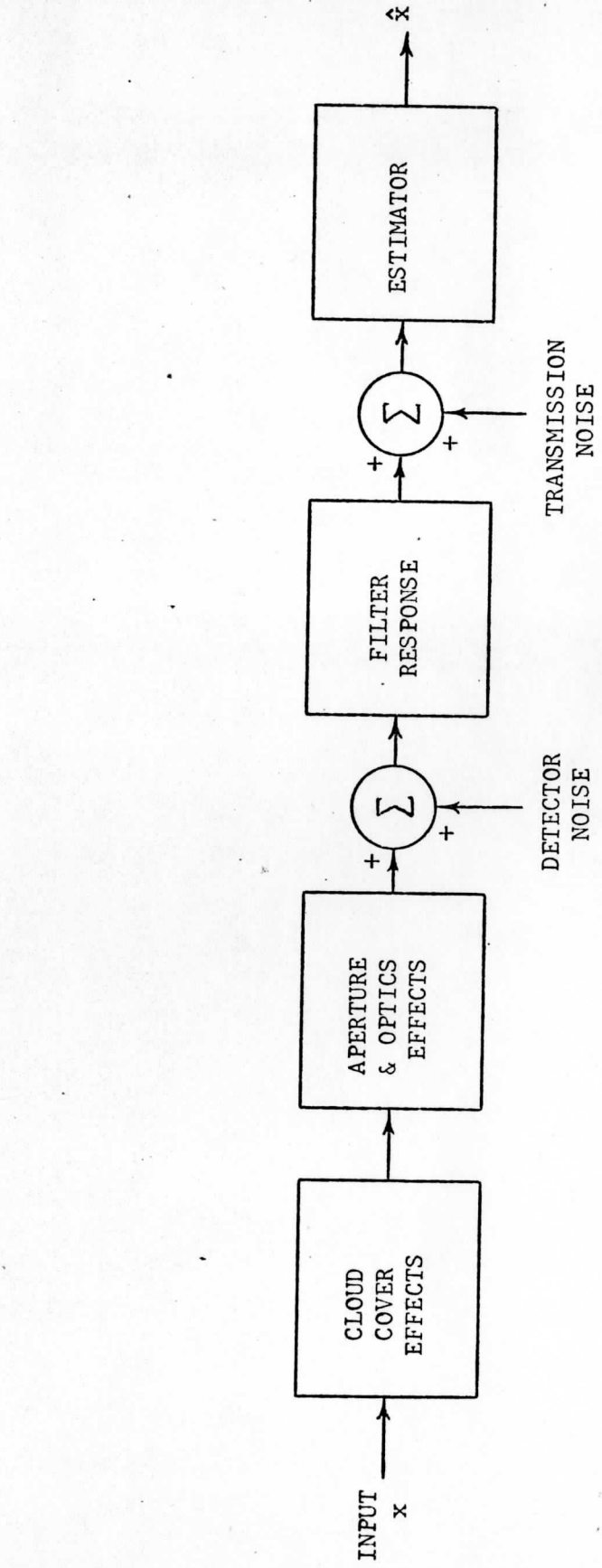


Figure 2.2 AVHRR Simulation Model.

For linear systems, the rise time can also be expressed as that time required for the indefinite integral of the system impulse response to go from 10% to 90% of its final value. This can be expressed as:

$$\int_o^{t_o} h(t)dt = 0.1 \int_o^{\infty} h(t)dt;$$

$$\int_o^{t_1} h(t)dt = 0.9 \int_o^{\infty} h(t)dt;$$

$$t_r = t_1 - t_o \tag{2.3}$$

The effective width, $\Delta$, of the impulse response will be taken as a measure of the IFOV of the system. On a mean-square basis, we define $\Delta$ as:

$$\Delta = \left[ \frac{\int_o^{\infty} (t-\bar{t})^2 \, |h(t)|^2 dt}{\int_o^{\infty} |h(t)|^2 dt} \right]^{1/2} \tag{2.4}$$

where $\bar{t}$ is the mean delay time defined by:

$$\bar{t} = \frac{\int_o^{\infty} t|h(t)|^2 dt}{\int_o^{\infty} |h(t)|^2 dt} \tag{2.5}$$

Combining Equations 2.3 and 2.4, a fairly reasonable approximation is that:

$$\Delta \approx t_r \tag{2.6}$$

so that Equation 2.2 can be rewritten as:

$$\Delta \approx (2B)^{-1} \tag{2.7}$$

The specification of an IFOV of 0.59 n mi therefore sets the minimum presampling filter bandwidth at about 0.85 cycles per n mi. Note that it is actually

the combination of the MTF of the optics and the presampling filter which must meet this condition.

Signals passing through the filter must also meet the requirements of the sampling theorem. Choosing $f_s$ to be the sampler frequency (i.e., repetition rate), we insist that:

$$f_s \geq 2B \tag{2.8}$$

It is convenient to normalize this by defining a dimensionless parameter k such that:

$$k = f_s/(2B) \tag{2.9}$$

For a Nyquist (minimum) sampling rate, k = 1; for all practical systems, k > 1.

A primary consideration in sampling theory is the relative amount of spectral fold-over or aliasing which occurs when input signals are not sufficiently band-limited prior to sampling. Consider the magnitude frequency transfer functions of three typical fifth-order presampling filters as shown in Figure 2.3. All three are normalized to their -3 dB bandwidths and the corresponding transfer functions can be found in [Stremler, Redinbo et al. 1974, p. 3-9]. A convenient measure of the relative amount of aliasing energy present is [ibid., p. 3-14]:

$$\% \text{ aliasing} = \frac{\int_o^{\omega_s/2} \omega^2 S_y(\omega - \omega_s)\,d\omega}{\int_o^{\omega_s/2} \omega^2 S_y(\omega)\,d\omega} \tag{2.10}$$

where $S_y(\omega)$ is the power spectral density of the signal at the sampler and $\omega_s$ is the sampler frequency in radian frequency.

As the worst-case assumption, we let $S_y(\omega)$ represent white noise filtered by the presampling filter so that:

$$S_y(\omega) = N_o|H(\omega)|^2 \tag{2.11}$$

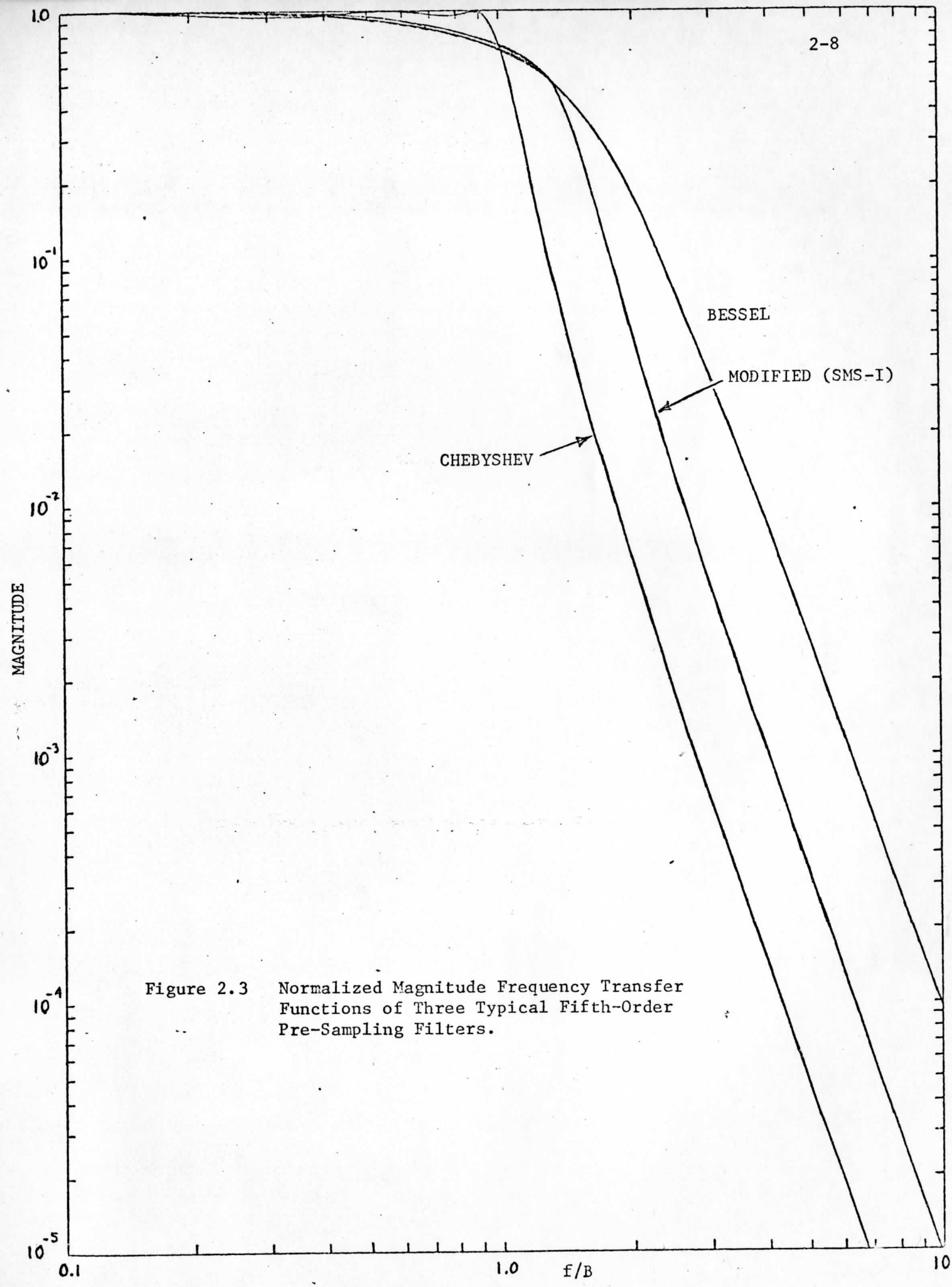


Figure 2.3 Normalized Magnitude Frequency Transfer Functions of Three Typical Fifth-Order Pre-Sampling Filters.

Converting to a discrete frequency (integer) parameter n and shifting the frequency axis for convenience in using numerical computation procedures, Equations 2.10, 2.11 become:

$$\% \text{ aliasing} = \frac{\sum_{n=1}^{M/2} (n - M/2)^2 |H(n + M/2)|^2}{\sum_{n=1}^{M/2} n^2 |H(n)|^2} \qquad (2.12)$$

where M is the (integer) sampling frequency.

Results of the computation of Equation 2.12 for the three filter characteristics shown in Figure 2.3 are shown in Figure 2.4 and displayed as a function of: $k = f_s(2B)$. While the advantages of the sharp cutoff Chebyshev filter are obvious here it must be remembered that these filters also have considerable step overshoot and ringing. Therefore the relative amount of aliasing is but one of several constraints on the problem. For a given type of filter, larger values of k are advantageous. However, the consequence of larger values of k are that more bandwidth is needed to transmit the digitally-encoded values, and some compromise is usually necessary. For example, the choice for the SMS-I visual scanners is: $k = 500/450 = 1.11$.

The problem of aliasing is brought up here because the choice of the sampling parameter k has another effect on the problem under consideration. From Equations 2.6, 2.7 we have that $\Delta \approx t_r \approx (2B)^{-1}$ and from Equation 2.9 we have: $f_s = k(2B)$. The number of sample points available in the observed data at the estimator during one IFOV is then:*

$$\frac{t_r}{t_s} = \frac{1/(2B)}{1/(2kB)} = k \qquad (2.13)$$

Therefore there are only k sample points available in each IFOV. In a typical situation k would be chosen between about 1.1 and 1.5. This places a rather

* The bandwidth of the MTF is about one-half that assumed for the pre-sampling filter so this result is a pessimistic one.

Figure 2.4 Percent Aliasing of the Pre-Sampling Filters shown in Fig. 2.3

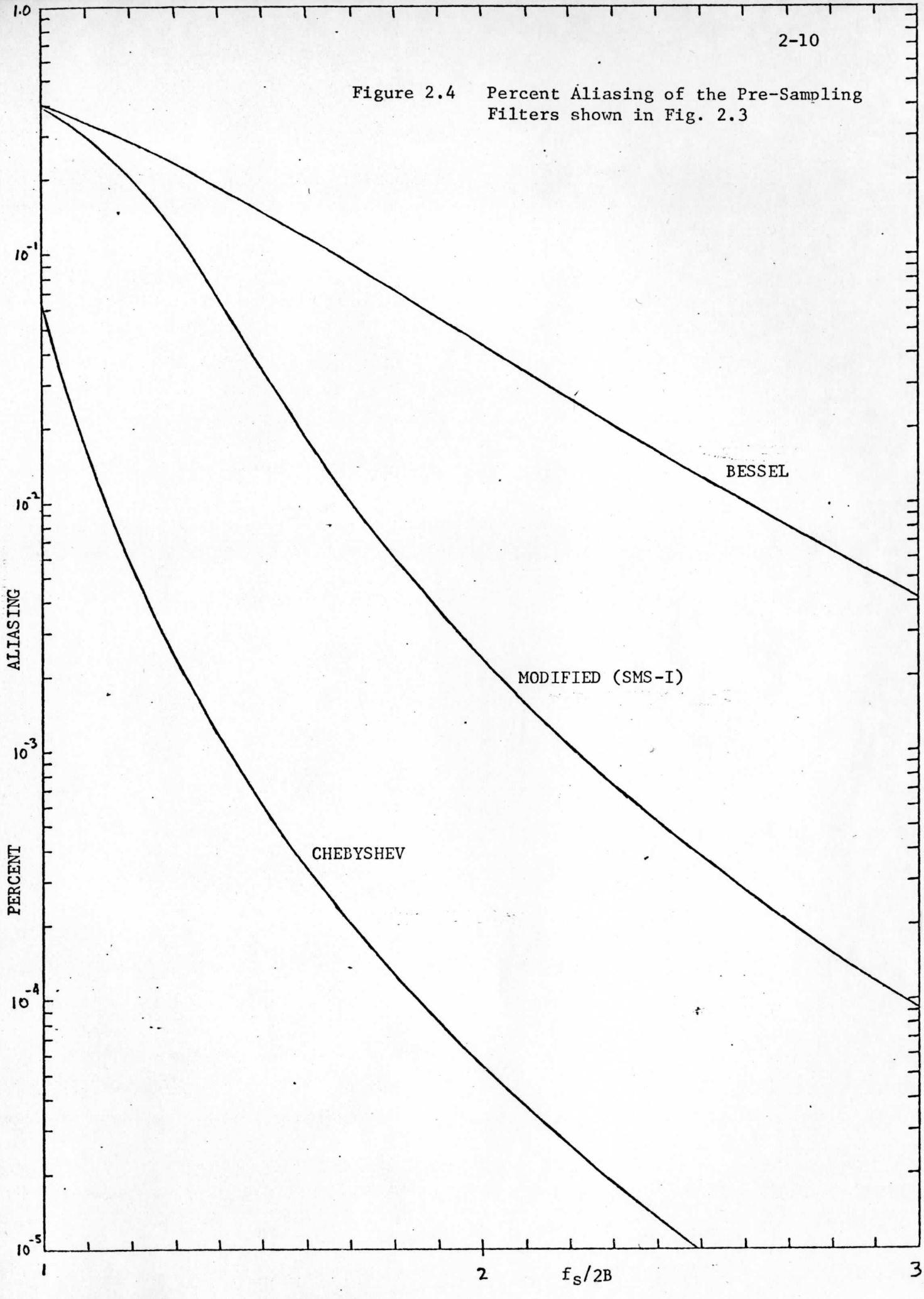

severe constraint on the problem under consideration because there are only a few sample points available. The more conventional type of estimator uses multiple sample points to compute covariance matrices and then proceeds to estimate future values based on past history. In contrast, we are required to make estimates based on 1-3 sample points.

This problem would be extremely difficult under the above conditions were it not for the fact that there is some a priori information available--the system impulse response. Our approach has narrowed to the use of as much of this a priori information as possible rather than to rely on the more general adaptive computational techniques. Because everything in the system is linear and time-invariant, our approach here is in the use of linear time-invariant systems.

One method which lends itself to this approach is that using least-squares filtering. A possible model for the problem under consideration is shown in Figure 2.5. The noiseless input signal f(t) is observed through a system whose desired impulse response is p(t) and is compared, on a mean-square error basis, to the signal plus additive noise when observed through the actual system. If the statistics of the signal and the noise are stationary (at least wide-sense stationary), the problem can be formulated in terms of their power spectral densities.

We shall designate the operation of convolution by " $\circledast$ "; referring to Figure 2.5, the ideal filtering of the signal is:

$$z(t) = f(t) \circledast p(t) \tag{2.14}$$

We assume that the signal and the noise are statistically independent and additive:

$$y(t) = f(t) + n(t) \tag{2.15}$$

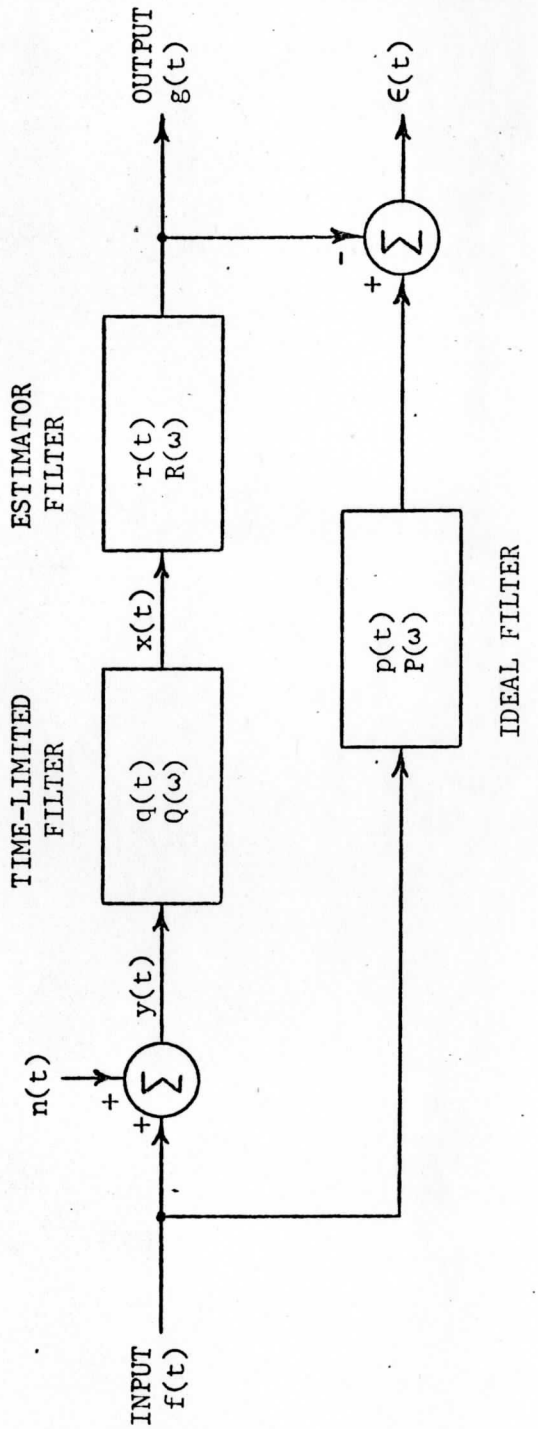


Figure 2.5 Model of the Least-Squares Problem

The filtering performed by the response q(t) of the actual system is time-limited to (0,T) so that:

$$x(t) = [q(t) \circledast y(t)]_{t=0}^{t=T} \tag{2.16}$$

This integral equation is difficult to solve exactly for the finite limits [Van Trees, 1968; Sage and Melsa, 1971]. Therefore we assume a high S/N condition and allow observations of past data. Within these restrictions, Eq 2.16 can be rewritten as

$$x(t) = \{q(t)\ \text{rect}[(t-T/2)/T]\} \circledast y(t) \tag{2.17}$$

where

$$\text{rect}\ (t/T) = \begin{cases} 1, & |t/T| < 1/2 \\ 0 & \text{otherwise} \end{cases}$$

and the mean-square estimator is described by r(t); its output is the estimated value:

$$g(t) = x(t) \circledast r(t) \tag{2.18}$$

We now let p(t) = g(t) for all t. (We could also include a predictor here if we are not willing to allow some delay to obtain our estimate.) The error in the estimate is:

$$\varepsilon(t) = z(t) - g(t)$$

$$\varepsilon(t) = f(t) \circledast p(t) - q(t)\text{rect}[(t-T/2)/T] \circledast y(t) \circledast r(t)$$

$$\varepsilon(t) = f(t) \circledast p(t) - h(t) \circledast y(t)$$

where:

$$h(t) = q(t)\text{rect}[(t-T/2)/T] \circledast r(t) \tag{2.19}$$

Next the autocorrelation of the error can be written in terms of the auto- and crosscorrelations of f(t), y(t). Taking a Fourier transform yields an equation in terms of the power spectral densities:

$$S_\varepsilon(\omega) = S_f(\omega)|P(\omega)|^2 + S_y(\omega)|H(\omega)|^2 - S_{fy}(\omega)P(\omega)H^*(\omega)$$

$$- S_{yf}(\omega)P^*(\omega)H(\omega) \tag{2.20}$$

The optimum choice of H(ω) [and therefore of R(ω)] minimizes the mean-square error:

$$\overline{\epsilon^2} = \frac{1}{2\pi} \int_{-\infty}^{\infty} S_\varepsilon(\omega) d\omega \tag{2.21}$$

This is now set up in a fairly standard problem in least-squares filtering for which the solution can be expressed as [Brown, 1963]:

$$H(\omega) = \frac{S_f(\omega)}{S_f(\omega) + S_n(\omega)} P(\omega) \tag{2.22}$$

Relating this to the problem at hand, the required estimator filter is:

$$R(\omega) = \frac{S_f(\omega)}{S_f(\omega) + S_n(\omega)} \frac{Q(\omega)}{Q(\omega)\exp(-j\omega T/2) \circledast T\mathrm{Sa}(\omega T/2)} \tag{2.23}$$

where: $\mathrm{Sa}(x) \triangleq (\sin x)/x$. The resulting minimum mean-square error is:

$$\overline{\epsilon^2} = \frac{1}{2\pi} \int_{-\infty}^{\infty} \frac{S_f(\omega) S_n(\omega)}{S_f(\omega) + S_n(\omega)} |Q(\omega)|^2 d\omega \tag{2.24}$$

For step function input signals, $S_f(\omega) = S/\omega^2$, where S is indicative of signal strength. Also let $S_n(\omega) = N$ (a constant) with signal and noise uncorrelated. Then Equation 2.24 simplifies to:

$$\overline{\epsilon^2} = \frac{1}{2\pi} \int_{-\infty}^{\infty} \frac{SN}{S + N\omega^2} |Q(\omega)|^2 d\omega \tag{2.25}$$

where $Q(\omega)$ is the overall frequency transfer function of the scanner response. For high S/N ratios, the minimum mean-square error is therefore determined only by the overall system frequency transfer function $Q(\omega)$ and the narrower (i.e., less bandwidth) the transfer function $Q(\omega)$ the better were it not for the fact that the spatial resolution is correspondingly degraded. Of course, a larger and larger delay time in the estimation is also encountered but we have not placed a restriction on this here. For low S/N ratios, a first-order filter which is dependent on the value of S/N is also present to help cut down the

effects of the noise. (This is a result of the assumptions made earlier and can be disregarded here.) Note that this approach does not state if the optimum filter is actually realizable or not but it does yield a minimum error if such a system could be realized with linear time-invariant systems.

The above approach was selected because there are so few data points available and maximum use of all a priori information is desirable. Steps to compute minimum mean-square errors are quite straight-forward, but some difficulty may arise in actually synethesizing an optimum filter.

The above analysis has not specifically considered the effect of the optical system MTF although it was realized that the presampling filter must be chosen within the constraints of the MTF. Table 2.2 summarizes the given data points on the MTF and the use of the frequency scaling factors shown in Figure 2.1 to yield the scanner frequencies.

TABLE 2.2

MTF Data and Frequency Scaling for TIROS N

| MTF value | Δ, n mi | B = 1/2Δ, c/n mi | satellite frequency in kHz: 400 n mi orbit | 450 n mi orbit | 500 n mi orbit |
|---|---|---|---|---|---|
| 1.00 | 11.8 | 0.0424 | 0.639 | 0.719 | 0.799 |
| 0.75 | 1.18 | 0.4237 | 6.390 | 7.189 | 7.987 |
| 0.50 | 0.88 | 0.5682 | 8.568 | 9.639 | 10.710 |
| 0.30 | 0.59 | 0.8475 | 12.780 | 14.377 | 15.975 |

A computer program was used to fit the data points supplied and listed in Tables 2.1, 2.2 to a ratio of tenth-order Chebyshev polynomials. Making use of the fact that the MTF must be an even function of frequency, the resulting best fit (on a minimum mean-square error basis) yields the following transfer function:

$$H_1(f) = \frac{a_o + a_2 f^2 + a_4 f^4 + a_6 f^6 + a_8 f^8 + a_{10} f^{10}}{b_o + b_2 f^2 + b_4 f^4 + b_6 f^6 + b_8 f^8 + b_{10} f^{10}} \quad (2.26)$$

for $|f| \leq 0.9$, where:

$a_o = 1.000$ $\quad b_o = 1.000$

$a_2 = -0.01879$ $\quad b_2 = -0.1262$

$a_4 = -7.2737$ $\quad b_4 = 9.4875$

$a_6 = 20.1259$ $\quad b_6 = -22.4532$

$a_8 = -21.1560$ $\quad b_8 = 21.8397$

$a_{10} = 7.8307$ $\quad b_{10} = -7.7560$

and f is the spatial frequency in cycles per n mi. A plot of Equation 2.26 and the given data points is shown in Figure 2.6. Effects of the MTF will be included in future work using this frequency transfer function.

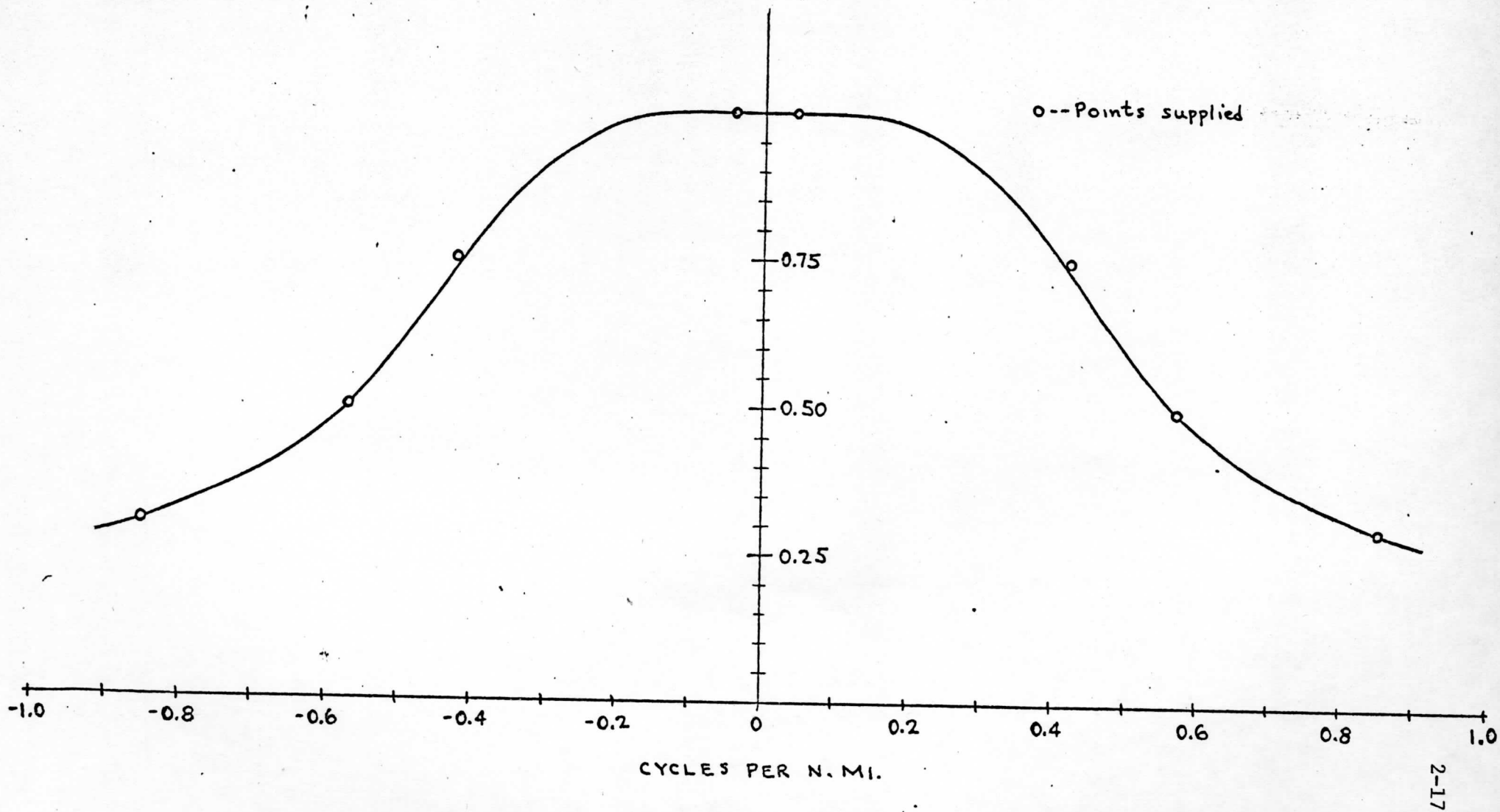


Figure 2.6 Best Fit to given MTF Data with a Ratio of Tenth-Order Chebyshev Polynomials

Because no data was given outside the range: $|f| \leq 0.9$ cycle per n.mi., a simple exponential was fitted at that point so that:

$$H_1(f) = 1.4033 \exp(-1.7839f) \tag{2.27}$$

for $|f| > 0.9$ cycle per n.mi. Using Eqs 2.26, 2.27, the impulse response $h_1(t)$ and step response of the MTF data is calculated:

$$h_1(t) = F^{-1}\{H_1(f)\} \tag{2.28}$$

and:

$$\text{unit step response} = \int_{\infty}^{t} h_1(\tau)\, d\tau \tag{2.29}$$

These are shown in Fig. 2.7.

Use of Eqs 2.26, 2.27 also permits us to calculate the mean-square error for an optimum estimator. We assume a step signal plus zero-mean white Gaussian noise. It is convenient to normalize the noise so that $k\sigma$ is equal to the signal step amplitude. For uncorrelated signal and noise, we can then rewrite Eq. 2.25 as:

$$\overline{\varepsilon^2} = \frac{2}{k^2} \int_o^{\infty} \frac{1}{k^2+(2\pi f)^2} \; |Q(f)|^2 \, df \tag{2.30}$$

Results of a numerical evaluation of this equation when evaluated for the given MTF data over a range 0-1 cycle per n mi is shown in Fig. 2.8.

From these results, it will require a normalized signal-to-noise ratio of about 30 to make an estimate within 0.1% of the true value. This agrees with our earlier assumption of a relatively high S/N ratio.

The optimum minimum-mean-square algorithm requires an estimate of the S/N ratio and the observation interval. The former is not crucial and we can assume a high S/N condition. It is sensitive to mismatches in the

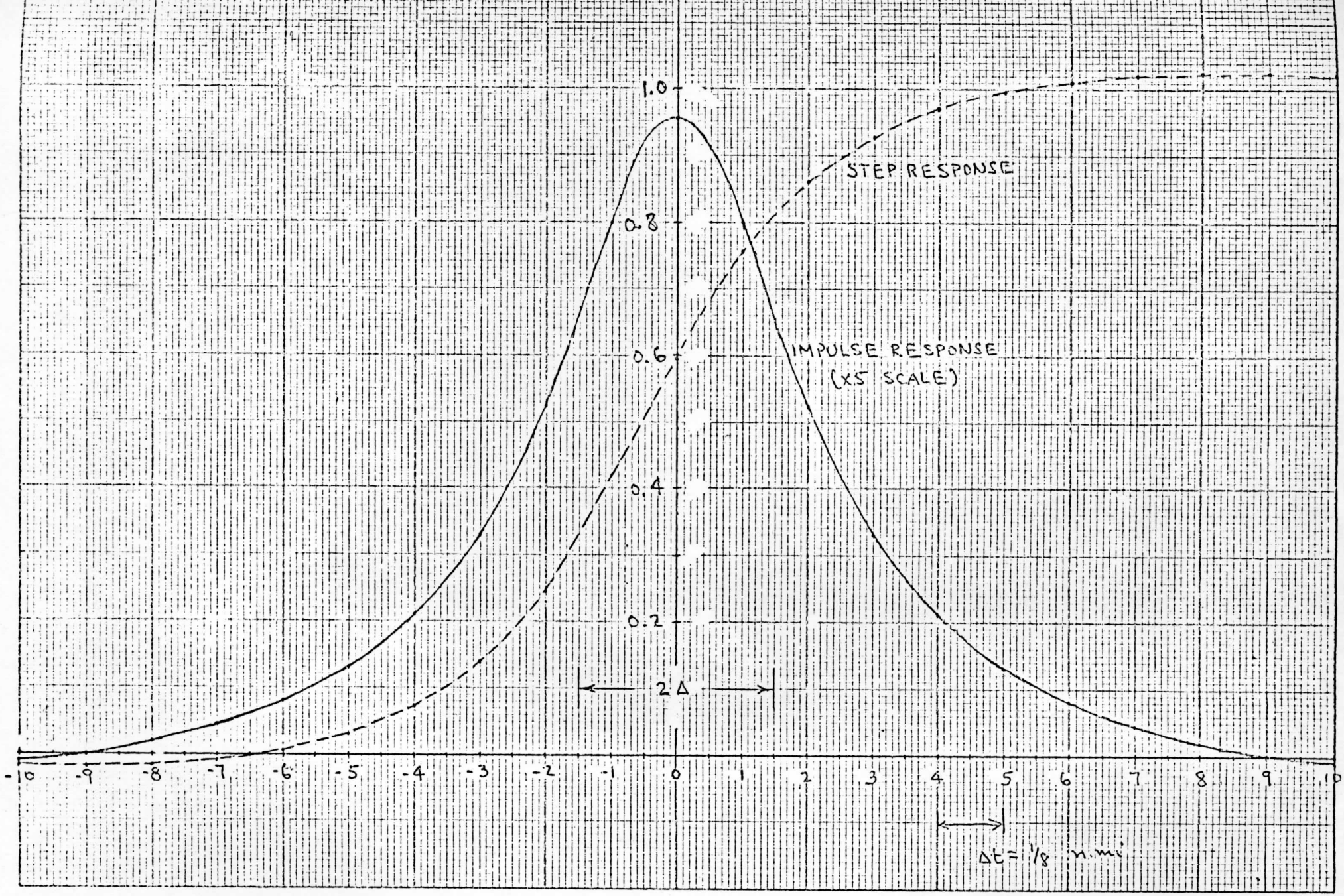


Figure 2.7. Impulse and Step Response of Tiros N Scanner MTF Data

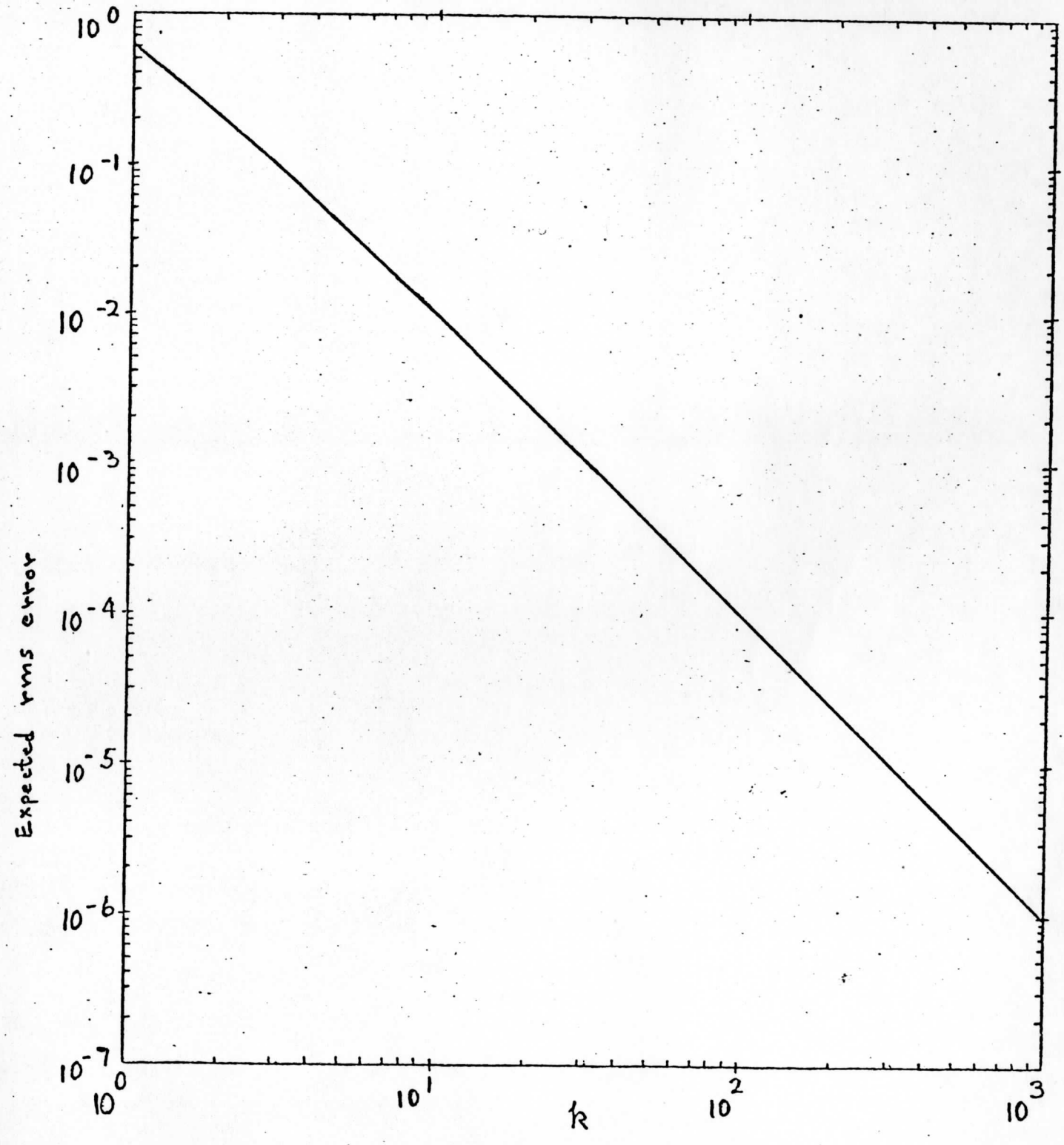


Figure 2.8. Minimum Mean-Square Error for the Optimum Step-Radiance-Level Estimator

length of the observation interval since this sets the gain of the estimator.

At this point it is advantageous that the samples are taken fairly far apart. The estimator algorithm thus will yeild solutions which are considerably in error if one allowable increment in the observation interval is erroneously made. So we simulated the mismatch conditions. The simulation results are discussed below.

Let t=T be the observation interval for which the estimator is designed. Let $t=T_o$ be the actual observation interval assuming that there is no uncertainty about the observation interval. In general $T_o$ is a random parameter and so the probability that $T_o \neq T$ has to be considered. For a non-adaptive estimator which does not estimate $T_o$, T is a constant, possibly arrived at through the use of some 'a priori' information. The condition $T_o \neq T$ is simulated for various assumed values of T, and $T_o$ is used as a parameter for a given value of T. Also to study the worst case, a peak signal (unity) to rms noise (standard deviation of noise) ratio of 10 has been used in the simulation. The error in assuming an S/N of 10 when one uses Eq. 2.17 is not considered to be significant.

While adding uncorrelated Gaussian noise, we considered the models in Figure 2.2 and in Figure 2.5. The former model corresponds to the case of adding detector noise while the latter corresponds to the case of noisy input. For the model in Figure 2.2, the simulation results are obtained for the following cases:

1. The case of addition of noise for all time, and
2. The case of addition of noise only over $0 \leq t \leq T_o$ while the unit step response of Q(w) for $t > T_o$ is assumed to be the unit step response at $t=T_o$ in accordance with Eq. 2.17.

For the model in Figure 2.5, again simulation results are obtained for the following cases.

1. The case of addition of noise response to the unit step response of Q(w) for all time.
2. The case of addition of noise response to the unit step response of Q(w) only over $0 \leq t \leq T_o$ while the unit response of Q(w) for $t > T_o$ is assumed to be the unit step response at $t=T_o$ in accordance with Eq. 2.17.

The following may serve as aids for easy recognition and interpretation of the simulation results.

Model A1: Case (1) of model in Figure 2.2

Model A2: Case (2) of model in Figure 2.2

Model B1: Case (1) of model in Figure 2.5

Model B2: Case (2) of model in Figure 2.5

- Sampling period in the time domain corresponds to a spatial sampling period of 0.068129 n.mile.

- Sampling period in the frequency domain corresponds to a sub-satellite point spatial frequency sampling period of 0.007167 cycles per n.mile.

- The effective width of the impulse response q(t) is about 6 samples.

- The autocorrelation function of the white Gaussian noise generated for the simulation is assumed to be an impulse of strength $\sigma_n^2$ situated at the origin and so $S_f(w) = N = \sigma_n^2$. Note that $\sigma_n^2$ is the variance of the Gaussian noise.

- The signal-to-noise ratio assuming a unit step input is $1/\sigma_n$.

- The overall mean squared error between the ideal step response and the estimated step response is normalized by dividing it by the average energy of the finite duration step response used in the simulation, namely 0.785.

- The optical transfer function Q(w) is non-zero over the spatial frequency range $0 \leq |f| \leq 7.34$ cycles per n.mile.

- The values of the ideal unit step response of Q(w) that are of interest in the simulation are tabulated below.

TABLE 2.3

STEP RESPONSE DATA OF OTF

| Sample Number | 1 | 2 | 3 | 4 | 5 | 6 | 7 | 8 |
|---|---|---|---|---|---|---|---|---|
| Unit Step Response Value | 0 | 0.018 | 0.035 | 0.057 | 0.084 | 0.120 | 0.166 | 0.225 |
| Sample Number | 9 | 10 | 11 | 12 | 13 | 14 | 15 | 16 |
| Unit Step Response Value | 0.300 | 0.390 | 0.490 | 0.592 | 0.685 | 0.762 | 0.824 | 0.872 |

- For each simulation the values of T, $T_o$ and S/N are specified and the corresponding normalized mean squared error is shown. T and $T_o$ are specified in terms of the number of samples since the sampling period (= 0.068129 n.mile) and the unit step response value at the sampling instants are known. For example, T=10 implies that the estimator is optimum if the true observation is 10 samples. A family of graphs showing the relation between the normalized mean squared error (MSE) and S/N with $T_o$ or the "mismatch' as a parameter is desirable. But the range over which the MSE varies is so large that a linear

scale for MSE is not desirable nor is a logarithmic scale. As has been mentioned earlier, the sensitivty of the MSE to the mismatch between T and $T_o$ is more serious and the effect of the noise even for an S/N ratio of 10 is tolerable. The simulation results verify these conclusions. Hence a table showing the relationship between the normlalized MSE and the S/N ratio for T=10 with $T_o$ as a parameter is presented for the model A1 estimator (Table 2.4). Then assuming an S/N ratio of 10 different mismatch conditions are simulated for different values of T and the corresponding normalized MSE values are tabulated in Table 2.5.

From Table 2.4, it is observed that the noise alone by itself is not a serious limitation to the estimation accuracy. But a mismatch by one or two samples introduces a significant estimation error even for a high S/N ratio. The steady state estimator output is found to be considerably in error when compared to unit. Also a decrease in S/N ratio for a given mismatch does not alter the % MSE significantly. In view of these results, we assumed an S/N ratio of 10 for all the 4 models and simulated mismatch conditions for different values of T. The results are shown in Table 2.5

From Table 2.5, it is observed that for a given T and $T_o$ such that $T=T_o$, the models A2 and A4 give rise to negligible estimation error. This can be anticipated because the noise influences the data only over the duration $0 \leq t \leq T_o$. On the otherhand, for a given T and $T_o$ ($T \neq T_o$), all the four models give rise to nearly the same estimation error. Thus we verify that the uncertainty associated with the value of $T_o$ can lead to significant estimation errors if an adaptive estimator capable of estimating $T_o$ is not employed.

TABLE 2.4

% MSE OF MODEL A1 ESTIMATOR

T=10

| S/N Ratio \ $T_o$ | 8 | 9 | 10 | 11 | 12 | 13 |
|---|---|---|---|---|---|---|
| 30 | 17.90 | 5.40 | 0.039 | 6.71 | 27.00 | 57.20 |
| 25 | 17.91 | 5.41 | 0.055 | 6.73 | 27.05 | 57.224 |
| 20 | 17.94 | 5.44 | 0.083 | 6.755 | 27.07 | 57.268 |
| 15 | 18.00 | 5.55 | 0.142 | 6.810 | 27.11 | 57.358 |
| 10 | 18.16 | 5.66 | 0.300 | 6.960 | 27.24 | 57.59 |

TABLE 2.5

% MSE OF ESTIMATOR FOR FOUR MODELS

S/N Ratio = 10

| T \ $T_o$ | | 8 | 9 | 10 | 11 | 12 | 13 | 14 | 15 |
|---|---|---|---|---|---|---|---|---|---|
| 9 | Model A1 | 6.15 | 0.51 | 9.14 | 41.39 | 96.00 | | | |
| | Model A2 | 6.16 | 0.009 | 9.127 | 40.00 | 95.86 | | | |
| | Model B1 | 6.754 | 0.762 | 10.07 | 41.97 | 97.22 | | | |
| | Model B2 | 6.167 | 0.017 | 9.15 | 40.90 | 96.00 | | | |
| 10 | Model A1 | 18.16 | 5.66 | 0.30 | 6.960 | 27.24 | | | |
| | Model A2 | 17.89 | 5.378 | 0.008 | 6.662 | 26.95 | | | |
| | Model B1 | 18.163 | 5.965 | 0.478 | 6.918 | 26.22 | | | |
| | Model B2 | 17.890 | 5.41 | 0.006 | 6.66 | 27.00 | | | |
| 11 | Model A1 | | 15.37 | 4.44 | 0.207 | 4.50 | 15.86 | | |
| | Model A2 | | 15.20 | 4.26 | 0.009 | 4.283 | 15.63 | | |
| | Model B1 | | 15.38 | 4.50 | 0.322 | 4.67 | 16.08 | | |
| | Model B2 | | 15.19 | 4.26 | 0.016 | 4.31 | 15.65 | | |
| 12 | Model A1 | | | 11.87 | 3.11 | 0.145 | 2.58 | 8.35 | |
| | Model A2 | | | 11.75 | 2.99 | 0.011 | 2.43 | 8.19 | |
| | Model B1 | | | 11.88 | 3.166 | 0.238 | 2.70 | 8.50 | |
| | Model B2 | | | 11.75 | 2.98 | 0.018 | 2.437 | 8.20 | |
| 13 | Model A1 | | | | 8.18 | 1.953 | 0.120 | 1.39 | 4.22 |
| | Model A2 | | | | 8.10 | 1.856 | 0.015 | 1.275 | 4.10 |
| | Model B1 | | | | 8.215 | 2.00 | 0.195 | 1.481 | 4.325 |
| | Model B2 | | | | 8.09 | 1.856 | 0.019 | 1.278 | 4.102 |

It is also noted that the estimation error for a given mismatch between T and $T_o$ depends on T i.e. smaller for higher values of T.

Since the different mismatch conditions are equally likely if no "a priori" information about $T_o$ is available, the estimation error is averaged for each of the possibilities a) $|T-T_o|=0$ b) $|T-T_o|=1$ c) $|T-T_o|=2$ (actually the estimation MSE is not an even function of $T-T_o$ but depends on T). Table 2.6 has the averaged % MSE for different values of $|T-T_o|$.

To give an idea of the performance of the different estimators, we have plotted in Figure 2.9 the estimated step response corresponding to Models $A_1$ and $B_1$ along with the ideal step response for T = 10, $T_o$ = 10 and S/N Ratio = 10 (The continuous curve corresponds to Model $A_1$ while the dashed curve corresponds to Model $B_1$). The estimated step response corresponding to Models $A_2$ and $B_2$ have not been plotted as they very closely follow the ideal step response.

TABLE 2.6

Averaged % MSE of Estimator for
Different Values of $|T-T_o|$

S/N Ratio = 10

| $\|T-T_o\|$ (No.of Samples) | Averaged % MSE | | | |
|---|---|---|---|---|
| | Model A1 | Model A2 | Model B1 | Model B2 |
| 0 | 0.2564 | 0.0104 | 0.399 | 0.076 |
| 1 | 4.541 | 4.445 | 4.72 | 4.451 |
| 2 | 16.53 | 16.44 | 16.90 | 16.543 |

FIGURE 2.9

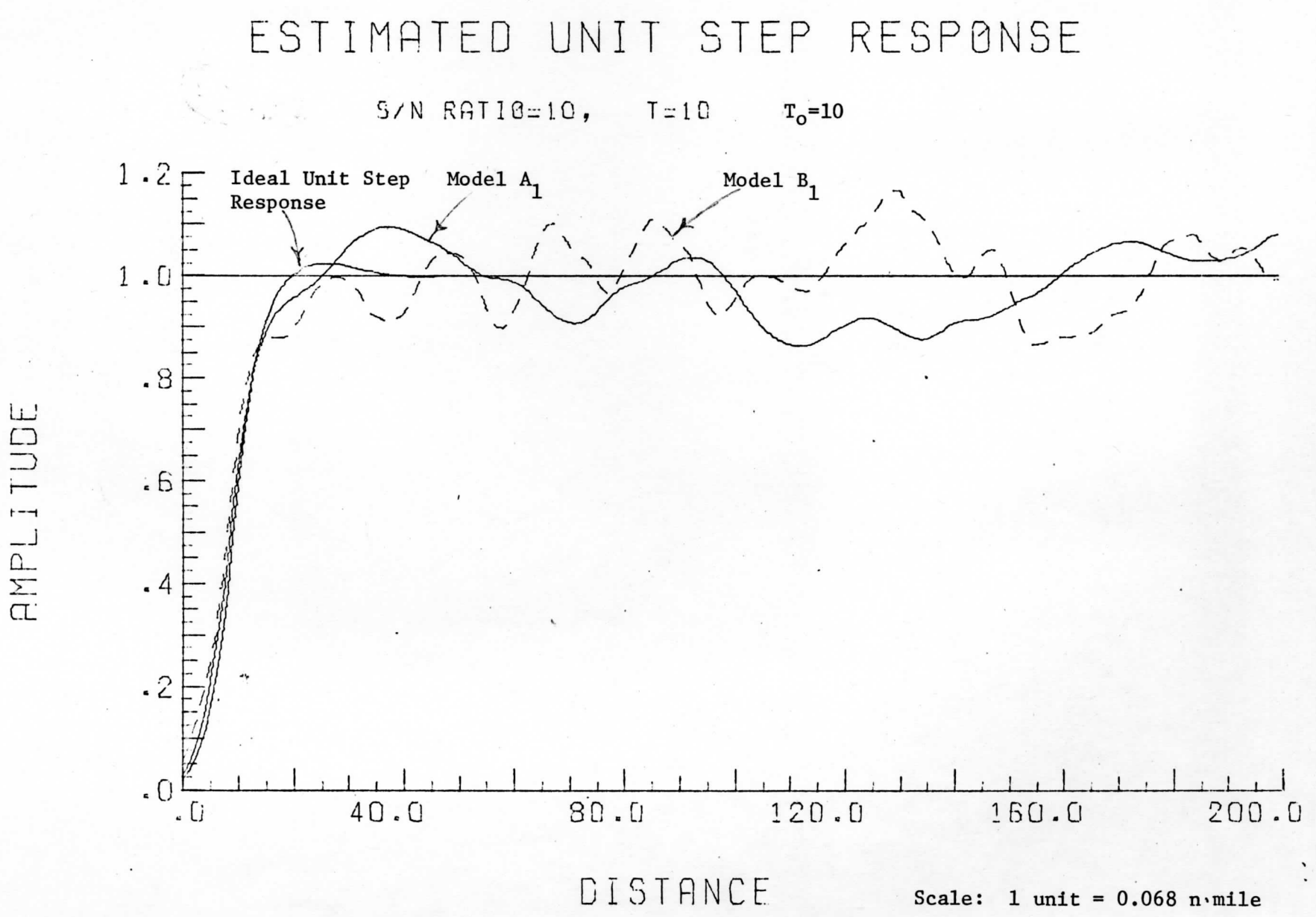
ESTIMATED UNIT STEP RESPONSE
S/N RATIO=10, T=10 $T_o$=10
Ideal Unit Step Response
Model $A_1$
Model $B_1$
AMPLITUDE
1.2
1.0
.8
.6
.4
.2
.0
.0
40.0
80.0
120.0
160.0
200.0
DISTANCE
Scale: 1 unit = 0.068 n·mile

# CHAPTER 3

## USE OF SYMMETRY RELATIONS IN WALSH TRANSFORM CODING

A major problem in the design of image coding systems for the high resolution visual channels of a geostationary orbiting satellite or, for that matter, any digital communication link, is finding a coding method which will minimize the number of code symbols required to describe an image without degrading the quality of the image beyond certain fidelity limits. It is also highly desirable to have a coding method which is less sensitive to channel errors and one which is easy to implement.

Out of the possible encoding methods for satellite scanner system some important methods are DPCM (Differential Pulse Code Modulation), transform coding, and interpolative coding. In DPCM encoding, the differences between adjacent brightness levels are encoded rather than the levels themselves, thereby resulting in savings in bandwidth. DPCM could be performed in both dimensions for transmitting two-dimensional images. Interpolative encoding uses nonuniform sampling methods for bandwidth compression. The disadvantage in this method is that it is difficult to efficiently multiplex several channels. Greater bandwidth reductions than DPCM can be obtained by transform coding techniques. This method also provides certain immunity to channel errors without significant image degradation. It is self multiplexing when applied to a visual scanner which has several parallel channels.

Figure 3.1 shows the block diagram of a generalized transform image coding system. Radiance samples of the image are converted into the

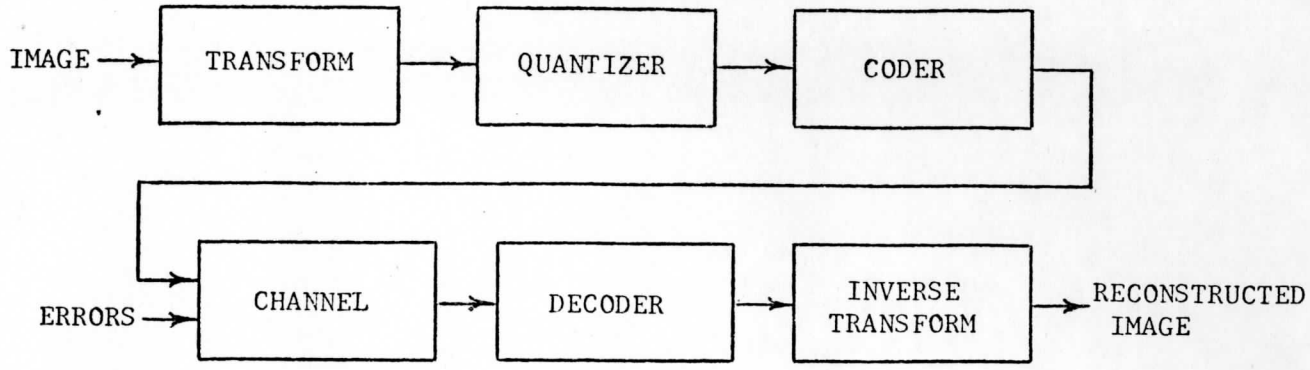


Figure 3.1 Image Transform Coding System.

transform domain using a suitable transform. Transformed samples are then quantized and coded for transmission from the satellite or over a digital link. Received data are decoded at the receiver and an inverse transformation of the decoded data gives the reconstructed image. Now the question arises -- What transform do we use? Do we have a choice? In order to answer these questions we must specify some criteria such as minimum cumulative mean-squared error in the transform domain, minimum cumulative spatial error, etc..

Some of the useful transforms treated in the literature are the Hadamard-Walsh, Haar, Haar-Hadamard, Slant, Slant-Haar, Discrete Cosine, and Kahunen Loueve transforms. Only the Walsh transform is discussed in this report. The sequency-ordered Walsh transform is used here, where sequency has the meaning of the number of zero crossing (sign changes) over the interval.

How do we get more bandwidth reduction by transmitting the transformed samples? It is found that most of the energy is concentrated in the lower sequencies and very little energy is contained in the higher sequencies.

Hence only the lower sequencies are transmitted without greatly affecting the quality of the reconstructed image. If the transformed samples, i.e. sequency coefficients, are correlated it is not necessary to transmit all the coefficients. We can take advantage of possible symmetry properties in the tranform domain to eliminate redundancy in transmitting the coefficients of the tranformed image samples, thereby resulting in a greater bandwidth reduction.

Suppose that a two-dimensional image is to be transmitted efficiently from the satellite scanner to the receiving ground stations using transform coding techniques. Let the sampled brightness levels of the image to be transmitted be arranged in a NxN data matrix. Let [X] be the input data matrix and let [Y] be its two-dimensional Walsh transformed output matrix. Then we can write:

$$[Y] = \frac{1}{N} [\overline{W}] [X] [W] \qquad (3.1)$$

where [W] is the Walsh matrix of order NxN. We are interested only in the symmetry relations between the off diagonal terms having the same horizontal and vertical sequencies, but in the reverse order. Let (i,j) be, respectively, the horizontal and vertical sequency number of [Y]. Then we need to know the symmetry relations between the sequency pair S(i,j); S(j,i), where 'S' stands for the sequency. Sequency pairs S(i,j); S(j,i) are said to be "symmetric" if they are equal both in magnitude and in sign. They are said to be "antisymmetric" if they are equal in magnitude but opposite in sign. All other cases are said to be "unsymmetric". It is not always possible to have perfectly symmetric or antisymmetric [Y] if the input is not totally symmetric. However, it is more useful to know whether the individual sequency pairs are symmetric, antisymmetric or unsymmetric. If they are found to be symmetric then there is no need to calculate the other

corresponding sequency component associated with that particular sequency pair. Thus if we know the symmetry conditions for sequency pairs beforehand then we could test for them while we are computing the transform itself. Because the sequency coefficients are projections of the data on the corresponding Walsh basis function, the symmetry conditions for a particular sequency pair depend upon certain of the Walsh functions. In general, the symmetry conditions for the sequency pair S(i,j), S(j,i) depend upon the Walsh basis function obtained by performing Walsh modulo addition of the basis functions for i and j:

$$\text{Symmetry } \langle S(i,j);\ S(j,i)\rangle \xrightarrow[\text{on}]{\text{Depends}} \text{Basis } (i \oplus_w j) \qquad (3.2)$$

where Walsh modulo addition is defined as:*

$$+ \oplus_w + = +;\quad - \oplus_w - = +$$

$$+ \oplus_w - = -;\quad - \oplus_w + = -$$

Alternatively, if we express the sequency numbers (i,j) in binary form then the Walsh modulo addition becomes modulo 2 addition. For example, the symmetry relations for sequency pairs S(6,3); S(3,6) depend upon the basis function obtained by adding Walsh modulo the basis functions Wal (6,m) and Wal (3,m):

$$\begin{array}{l} + + - - + + - - \text{ Wal } (3,m) \\ \underline{+ - + - - + - +} \text{ Wal } (6,m) \\ + - - + - + + - \text{ Wal } (5,m) \end{array}$$

Alternatively,

$$\begin{array}{l} j \rightarrow \text{sequency 3 in binary} \rightarrow 011 \\ i \rightarrow \text{sequency 6 in binary} \rightarrow \underline{110} \\ \quad\ \text{sequency 5 in binary} \rightarrow 101 \end{array} \quad \oplus_2$$

---

* This truth table can also be obtained using an "exclusive nor" binary operation.

Thus the symmetry relations between the sequency pairs (S(6,3); S(3,6)) depend upon the Walsh basis function Wal (5,m).

In order to find out the exact symmetry dependence we need to consider two cases. The first case involves the sequency coefficients having zero as one of their sequency numbers. These coefficients would be those in the first row and first column of the output matrix [Y]. The second case treats all other off-diagonal sequency pairs. Because most of the low sequency coefficients are coded and transmitted the first case is more important to us than the second case.

For the first case in general the symmetry relations are obtained by first obtaining the Walsh basis function on which they depend. For the sequency pair (S(0,j); S(j,0)) the basis function is $0 \oplus_2 j_B$ where $j_B$ is j expressed in binary form. Note that j runs from 1 through N. Let us call this basis function a "dependence basis function." Having obtained the basis function on which the symmetry relations depend, we sum the data values in [X] lying at the intersection of rows obtained from the locations of 1's in the dependence basis function and the columns obtained from the locations of -1's in the dependence basis function. Then we equate this sum to the corresponding sum obtained on the transpose of the input matrix [X]. The difference between the two sums gives the symmetry difference of that particular sequency pair. If we interchange the role of 1's and -1's, i.e., select the rows corresponding to locations of -1's and columns corresponding to locations of 1's, we get the antisymmetry difference of that particular sequency pair. It can also be shown that:

$$\text{Sequency Symmetry Difference} = \sum_{1\text{'s}} \text{rows} - \sum_{1\text{'s}} \text{columns}$$

$$\text{Sequency Antisymmetry Difference} = \sum_{1\text{'s}} \text{columns} - \sum_{1\text{'s}} \text{rows}$$

where 1's and -1's refer to locations of 1's and -1's in the dependence basis function of that sequency pair. Because the row sums and column sums are obtained during the calculation of the Walsh transform coefficients, we can test for the symmetry relations simultaneously. The symmetry and antisymmetry relations of the sequency pairs having at least one of their sequency numbers as zero are important because the symmetry relations for the higher order sequency pairs depend upon these lower order sequency pairs. The dependence basis function as we have noted earlier is the basis function obtained by adding modulo two the sequency numbers expressed in binary form of the particular sequency pair (S(j,i); S(i,j)) under investigation. This dependence basis function resulting from modulo two addition is always one of the (N-1) basis functions considered for the symmetry relations of those sequency pairs having at least one zero sequency number. Thus for the higher sequencies:

$$\text{Sequency Symmetry Difference} = \sum_{1\text{'s}} \text{rows} - \sum_{1\text{'s}} \text{columns} + \text{other terms due to higher sequencies} \tag{3.3}$$

$$\text{Sequency Antisymmetry Difference} = \sum_{1\text{'s}} \text{columns} - \sum_{-1\text{'s}} + \text{other terms due to higher sequencies} \tag{3.4}$$

where 1's and -1's refer to the locations of 1's and -1's in the dependence basis function. Other terms differ for every pair under consideration. The classification "other terms" can be obtained as follows:

"Other terms" = -2 (terms off the cross diagonal). (3.5)

Terms that are mentioned above are the same terms used in the evaluation of symmetry relations of the lower sequencies lying in the first row and first column. Thus we have defined symmetry relations for all the sequency

pairs of the output matrix [Y]. As the order of the matrix N is increased we have to take all possible cross diagonals. For example, in the 8 x 8 case if we divide the 8 x 8 [Y] matrix into four quarters then each quarter is a 4 x 4 array of sequency coefficients.

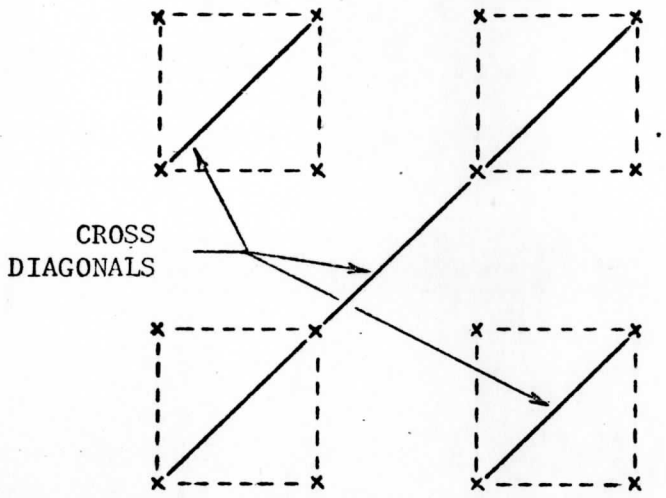


Figure 3.2 The Cross Diagonals of the Walsh Transform Array.

Cross diagonals are formed as shown in Figure 4.2. We collect only the points lying off the cross diagonals.

What is the error in forcing magnitude symmetry between sequency coefficients pairs on the reconstructed image? Certain Apollo VI series pictures are selected for this purpose (see Fig. 3.3). Picture size taken is 512 x 512 (40 n. mi. x 40 n. mi.). Each is divided into 8 x 8 blocks throughout. A two dimensional 8 x 8 transform is performed on each of these blocks and the Walsh coefficients are forced to have magnitude symmetry by averaging their values and preserving the sign. For example, the sequency pair (S(i,j); S(j,i)) is forced to have magnitude symmetry such that:

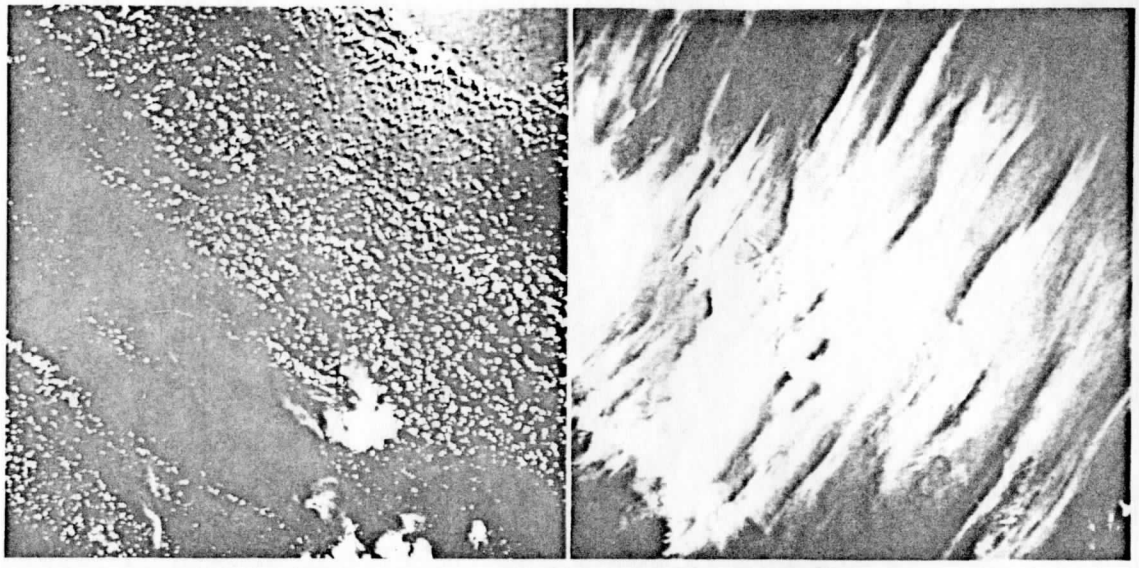

a) Original Apollo AS6-2-877

b) Original Apollo AS6-2-934

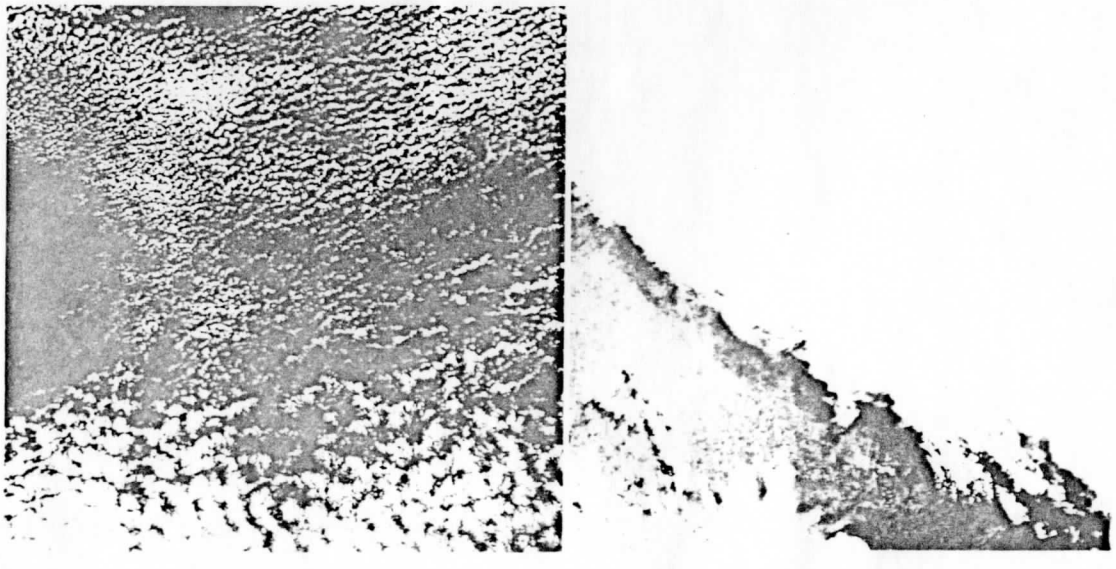

c) Original Apollo AS6-2-1430

d) Original Apollo AS6-2-1469

FIGURE 3.3

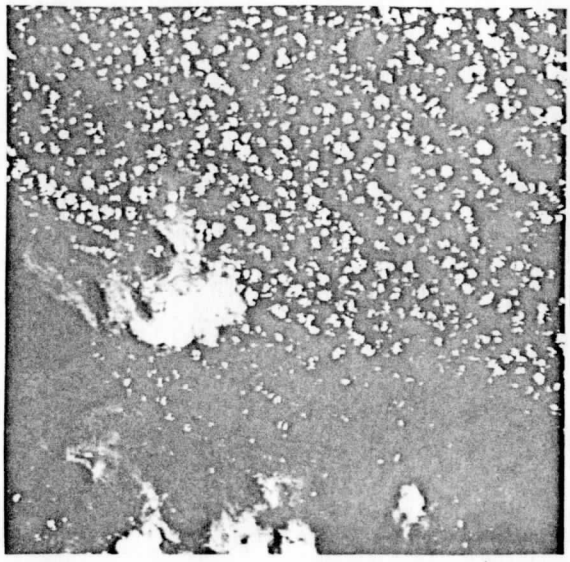

a) Lower right quarter of original Apollo AS6-2-877

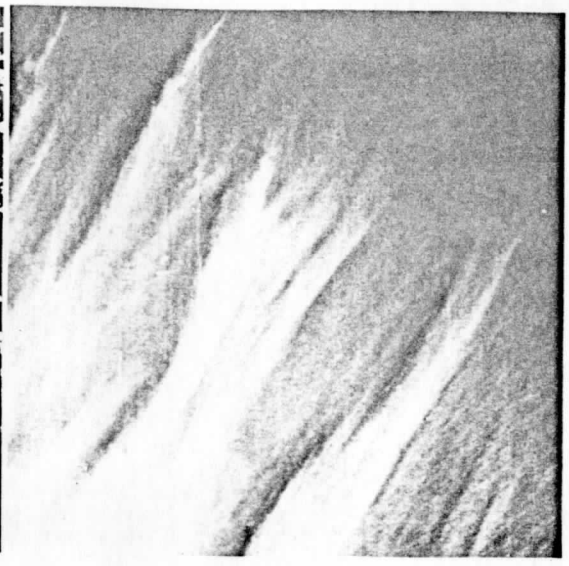

b) Upper right quarter of original Apollo AS6-2-934

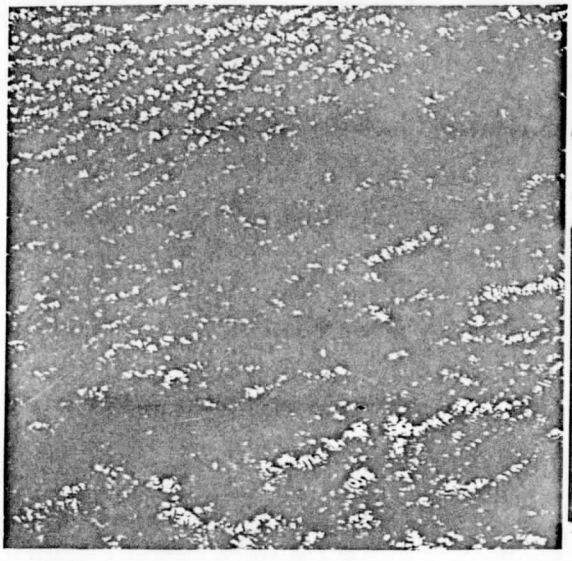

c) Central right quarter of original Apollo AS6-2-1430

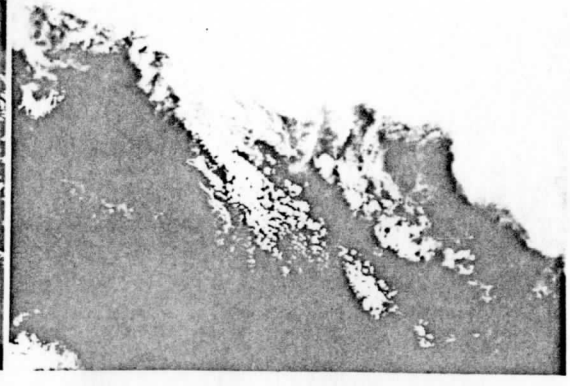

d) Lower right quarter of original Apollo AS6-2-1469

Figure 3.4

$$|\hat{S}(i,j)| = |\hat{S}(j,i)| = 1/2\ [|S(i,j)| + |S(j,i)|] \qquad (3.6)$$

where $\hat{S}(i,j)$ is the new value of the sequency after forcing the magnitude symmetry. Then an inverse two dimensional 8 x 8 Walsh transform is performed to reconstruct the image. As can be seen from the reconstructed images (Figure 3.5) there is very little degradation in the reconstructed picture quality as a result of forcing the magnitude symmetry. Then the histogram of probability of having unsymmetric, symmetric and antisymmetric sequency coefficient pairs over an 8 x 8 block is computed and the results are shown in Figure 3.6. A tolerance of $0.125\sigma$ is allowed where $\sigma$ is the standard deviation of that particular sequency pair. As noted from Figure 3.6 the probabilities in all three cases are nearly the same, meaning that all three types of symmetry cases are equally likely. The Walsh transform distributes the coding error over the whole reconstructed data matrix [X]. Because the magnitude symmetry (which includes both symmetry and antisymmetry) is more likely, the error seen in the reconstructed image is not significant.

Walsh power spectra of selected Apollo VI pictures are run using 512 x 512 data and yielding a 256 x 256 power spectrum matrix. The power spectrum here is the sequency ordered power spectrum. Power spectrum photographs are shown in Figures 3.7,3.8. These photographs reveal some circular symmetry which motivated our study of the symmetry properties of Walsh transform.

In conclusion, symmetry properties of the two dimensional Walsh sequency coefficients are studied and relations developed to test the symmetry and antisymmetry difference. This computation could be done simultaneously with the transform.

If the input data matrix [X] is totally symmetric, then the transformed output matrix [Y] is also totally symmetric. However, it is possible for some of the sequency pairs to be symmetric or antisymmetric even though the input data [X] is not symmetric as the relations for symmetry and antisymmetry depend only upon the sums and differences in particular regions fixed by the sequency pair. It is thus the collective behavior of input brightness levels in certain regions which determine the symmetry and antisymmetry of the transformed brightness levels. Error in forcing the magnitude symmetry between sequency pairs is analyzed using computer runs and plots and reconstructed pictures. Histograms of symmetric, antisymmetric and unsymmetric coefficients are computed and the results plotted. Finally, sequency-ordered power spectral photographs of Apollo VI pictures are shown and reveal fairly circular symmetry.

FIGURE 3.5

FORCED WALSH SYMMETRY RECONSTRUCTIONS

OF SELECTED PHOTOGRAPHS FROM APOLLO VI

Notes:

1. Each quarter-picture is 512 x 512 samples; full photograph scaling (1024 x 1024) is approximately 170km x 170km.
2. The following abbreviations are used:
   a) URQ means "upper right quarter",
   b) CRQ means "central right quarter",
   c) LRQ means "lower right quarter".
3. Sequency-ordered Walsh coefficients of an 8 x 8 array (only 16 coefficients are selected and retained for transmission) are forced to have magnitude symmetry about the principal diagonal of the matrix $\underset{\sim}{Y}$. This is done by averaging the magnitudes of the coefficients on either side of the diagonal while preserving their sign.

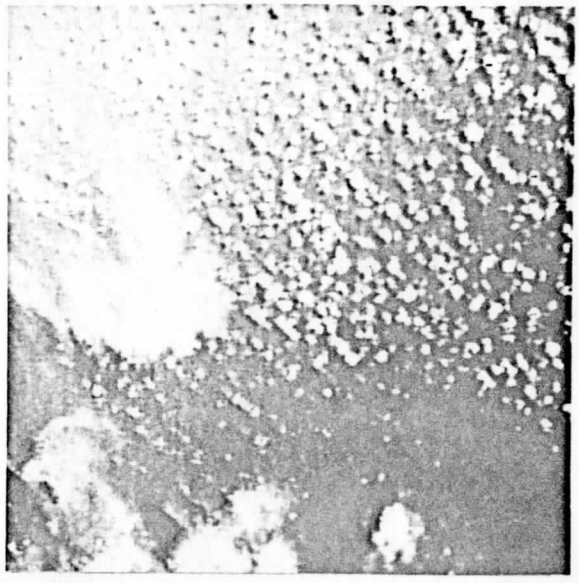

a) Apollo AS6-2-877
Quarter Picture: LRQ

b) Apollo AS6-2-934
Quarter Picture: URQ

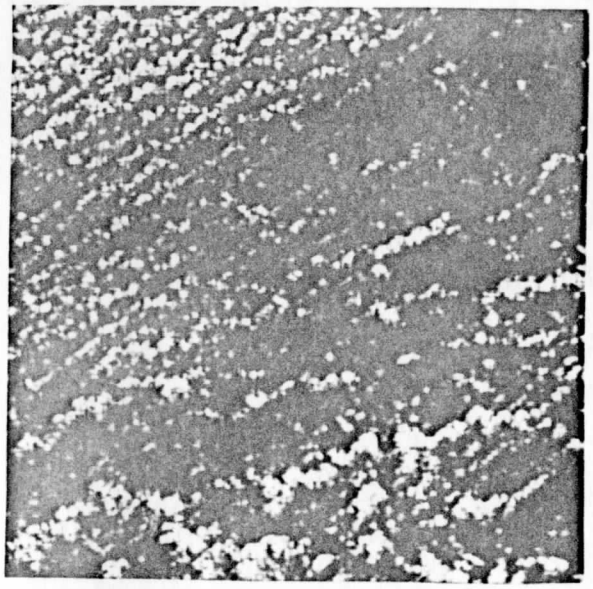

c) Apollo AS6-2-1430
Quarter Picture: CRQ

FIGURE 3.6. HISTOGRAMS OF SYMMETRIC, ANTISYMMETRIC, AND UNSYMMETRIC WALSH COEFFICIENTS OVER A 8 x 8 BLOCK OF APOLLO AS6-2-877 PICTURE.

NOTES: Tolerance used = $0.125\sigma$

where

$\sigma$ = Averaged standard deviation of the sequency coefficients averaged over three pictures (pictures 877, 934, 1064)

1. Histogram of Unsymmetric coefficients.
2. Histogram of Symmetric coefficients.
3. Histogram of Antisymmetric coefficients.

GRAPH PLOT NO. 01

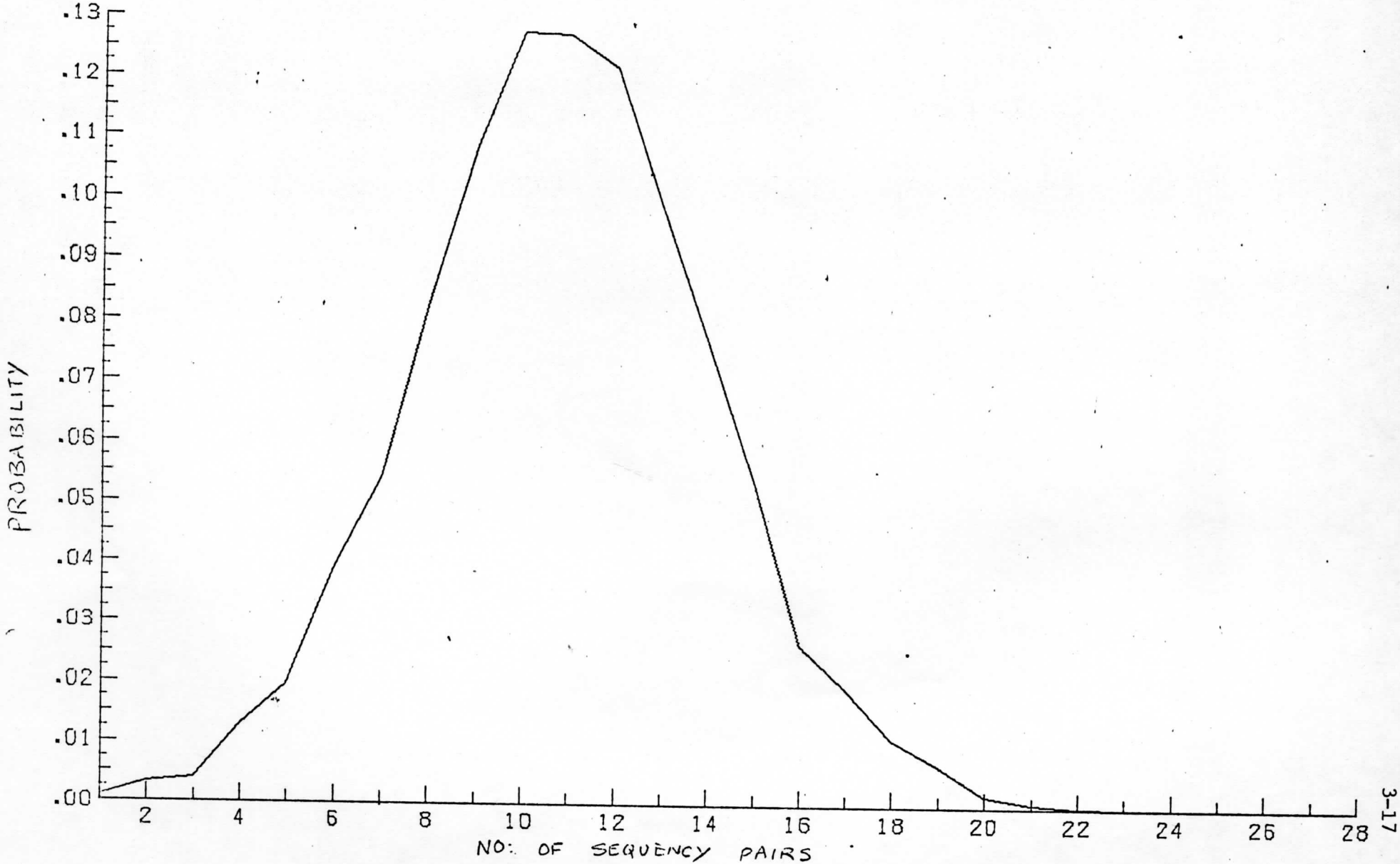


HISTOGRAM OF UNSYMMETRIC WALSH COEFFICIENTS

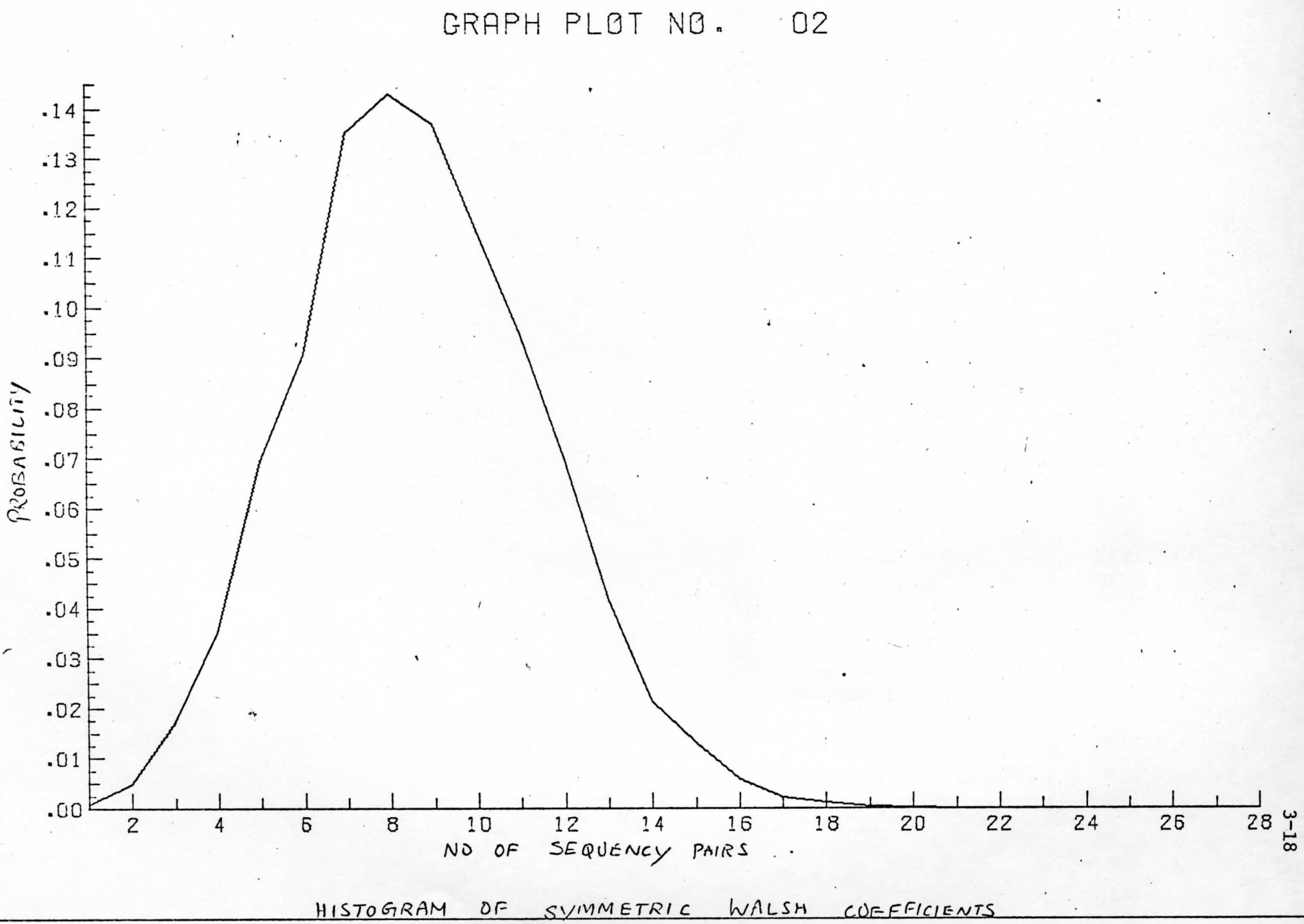


HISTOGRAM OF SYMMETRIC WALSH COEFFICIENTS

GRAPH PLOT NO. 03

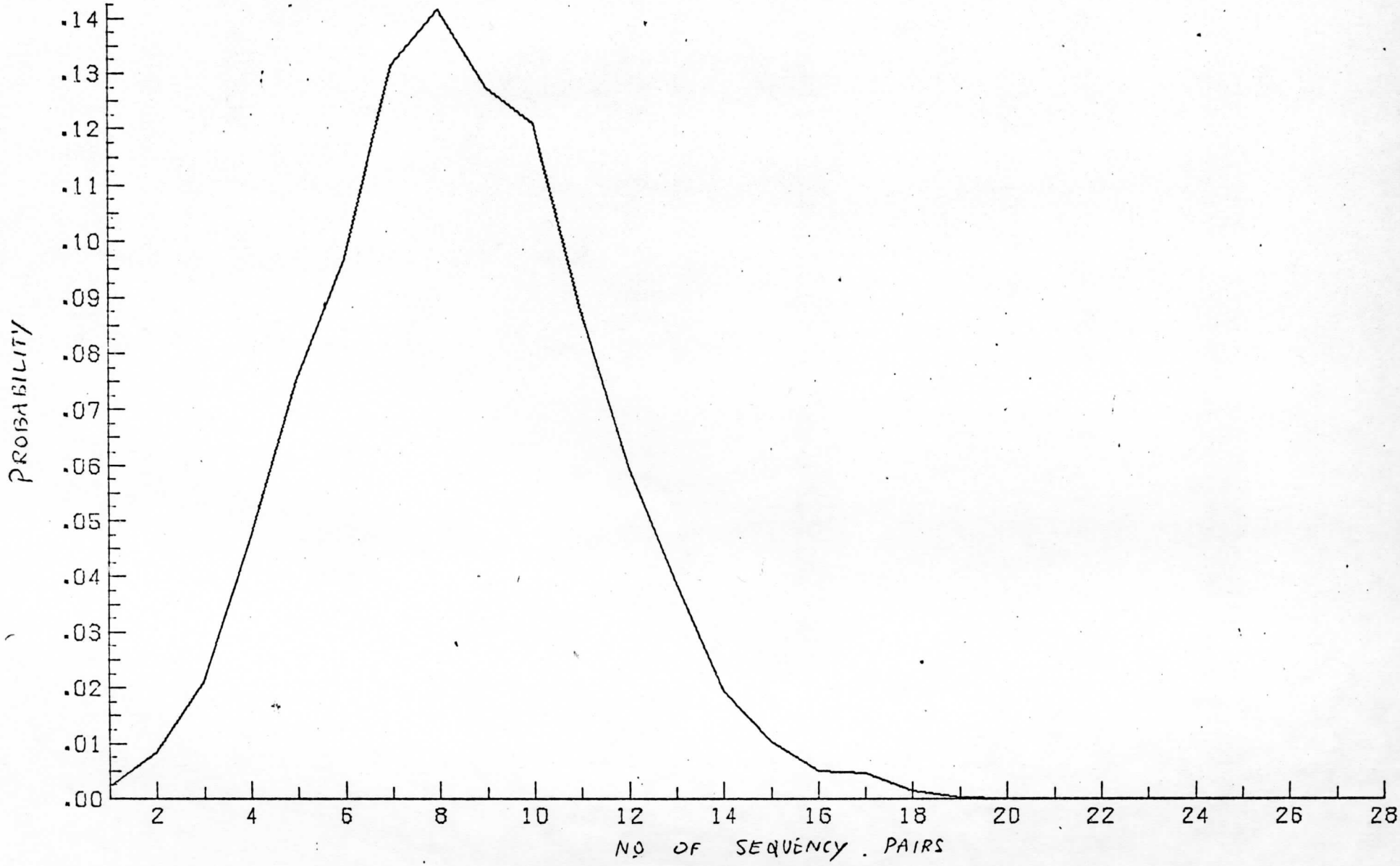


HISTOGRAM OF ANTISYMMETRIC WALSH COEFFICIENTS

FIGURE 3.7

SEQUENCY-ORDERED WALSH POWER SPECTRA

OF SELECTED PHOTOGRAPHS FROM APOLLO VI

Notes:

1. Data quantization is 8 bits and linear with transmissivity of a positive transparency.
2. The zero-sequency ("d.c.") terms are suppressed in these spectral reconstructions.
3. The following abbreviations are used:
   a) ULQ means "upper left quarter",
   b) URQ means "upper right quarter",
   c) LLQ means "lower left quarter",
   d) LRQ means "lower right quarter",
   e) CLQ means "central left quarter",
   f) CRQ means "central right quarter".
4. Each quarter-picture is composed of 512 x 512 spatial samples; each spectral reconstruction is 256 x 256 points.
5. Full photograph scaling (1024 x 1024) is approximately 170km x 170km.

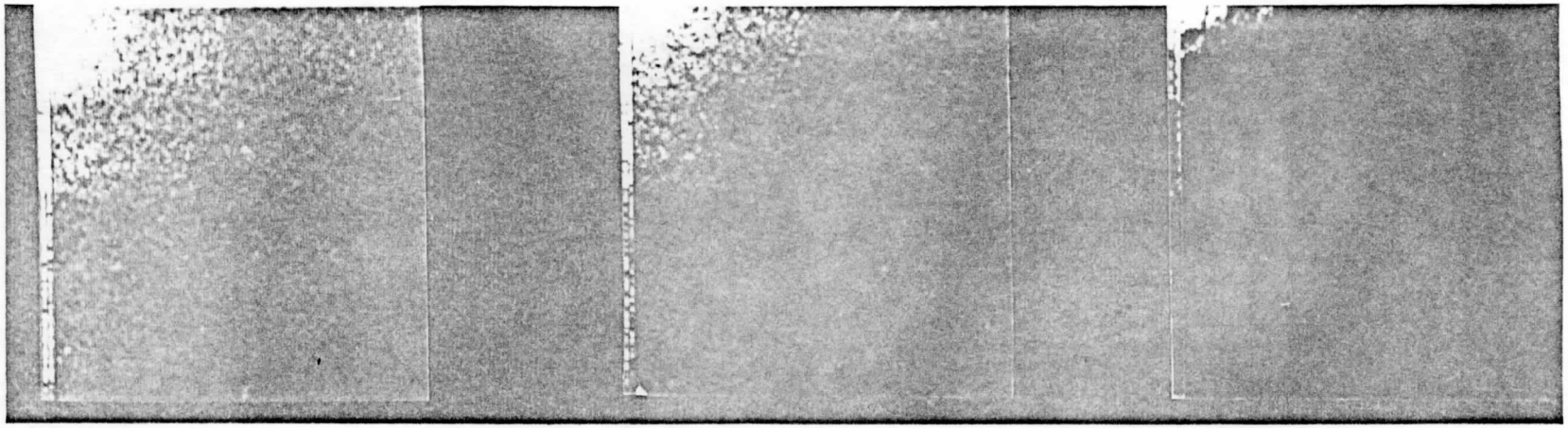

a) Apollo AS6-2-877
Quarter Picture: URQ

b) Apollo AS6-2-877
Quarter Picture: ULQ

c) Apollo AS6-2-934
Quarter Picture: URQ

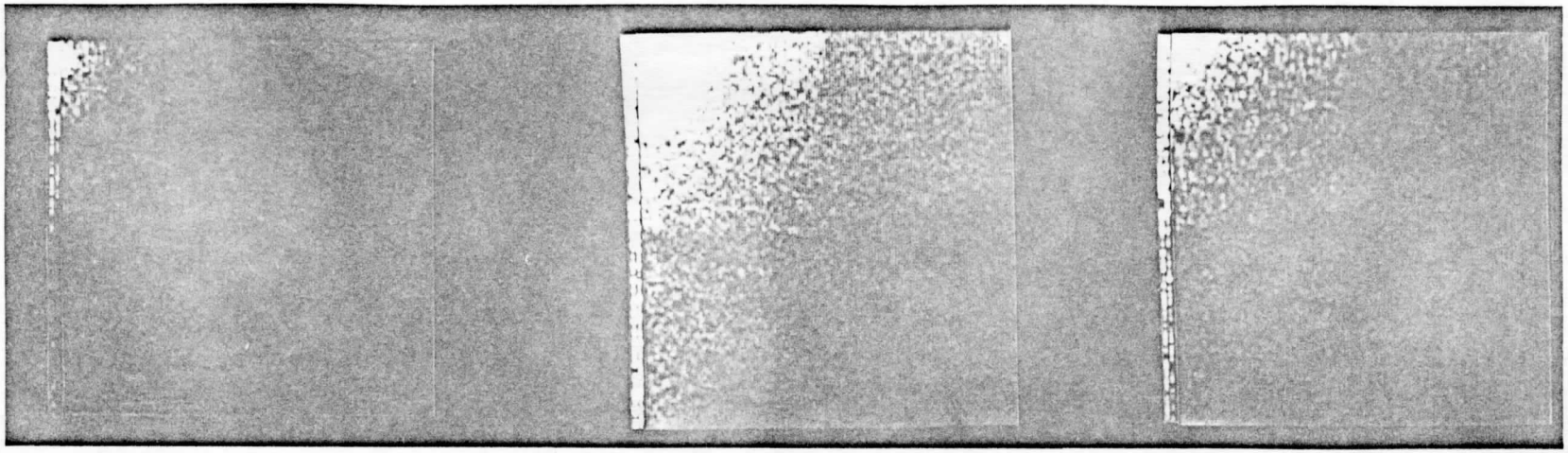

d) Apollo AS6-2-948
Quarter Picture: LLQ

e) Apollo AS6-2-1064
Quarter Picture: URQ

f) Apollo AS6-2-1429
Quarter Picture: LRQ

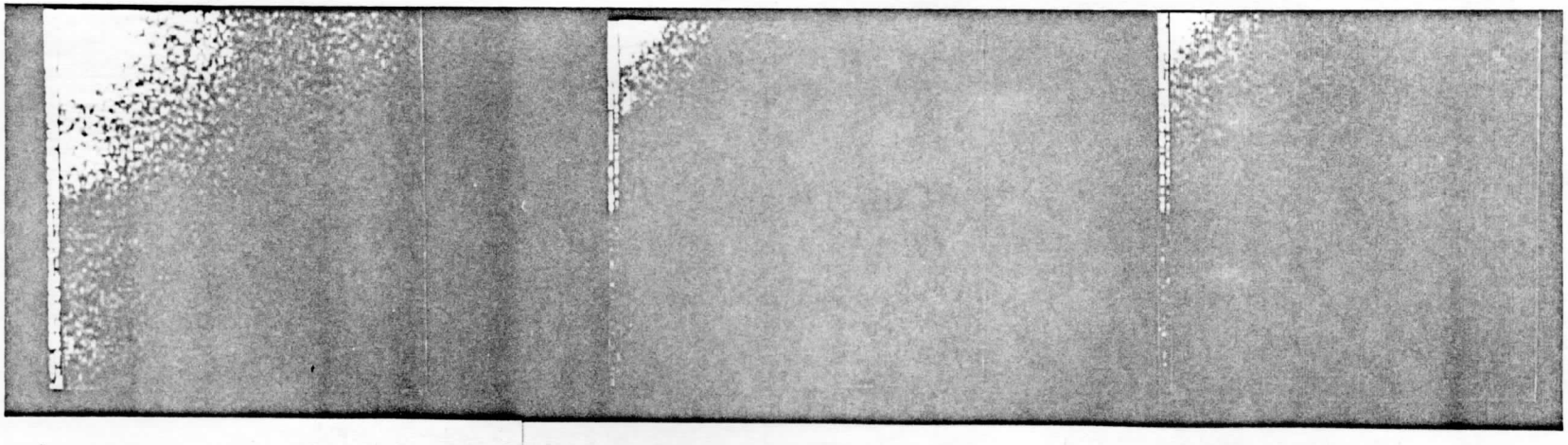

g) Apollo AS6-2-1430
Quarter Picture: CRQ

h) Apollo AS6-2-1467
Quarter Picture: LLQ

i) Apollo AS6-2-1468
Quarter Picture: LRQ

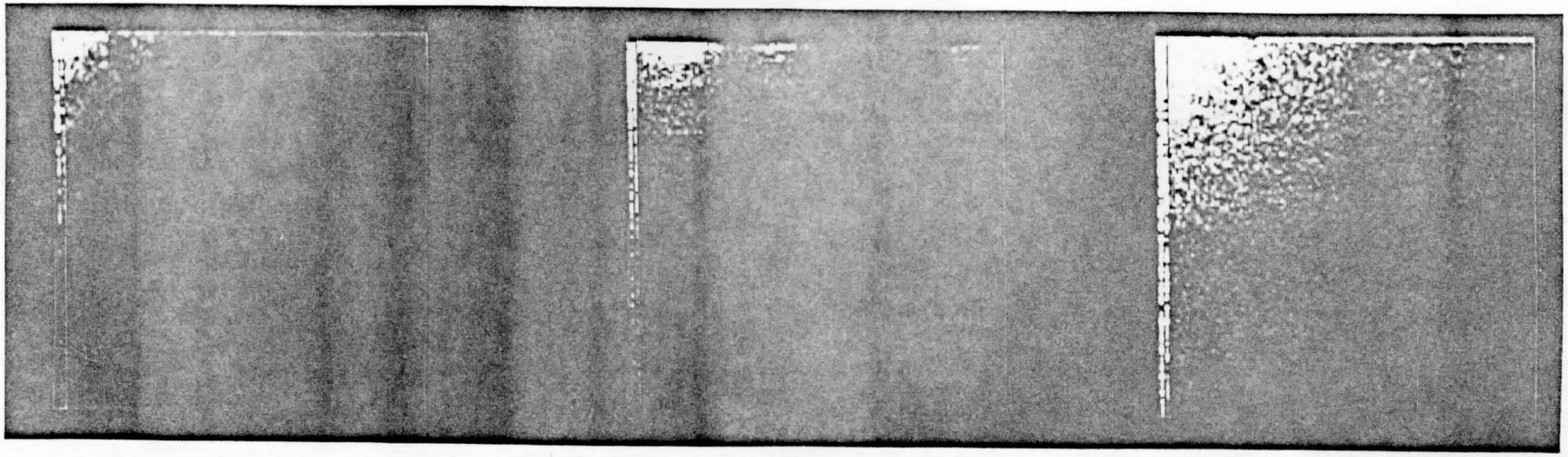

j) Apollo AS6-2-1469
Quarter Picture: LLQ

k) Apollo AS6-2-1484
Quarter Picture: CLQ

l) Apollo AS6-2-1484
Quarter Picture: CRQ

FIGURE 3.8

SEQUENCY-ORDERED WALSH POWER SPECTRA

OF SELECTED PHOTOGRAPHS FROM APOLLO VI

Notes:

1. Data Quantization is 8 bits and compressed by a square root law.
2. The zero sequency ("d.c.") terms are suppressed in these spectral reconstructions.
3. The following abbreviations are used:
   a) ULQ means "upper left quarter",
   b) URQ means "upper right quarter",
   c) LLQ means "lower left quarter",
   d) LRQ means "lower right quarter",
   e) CLQ means "central left quarter",
   f) CRQ means "central right quarter".
4. Each quarter-picture is composed of 512 x 512 spatial samples; each spectral reconstruction is 256 x 256 points.
5. Full photograph scaling (1024 x 1024) is approximately 170km x 170km.

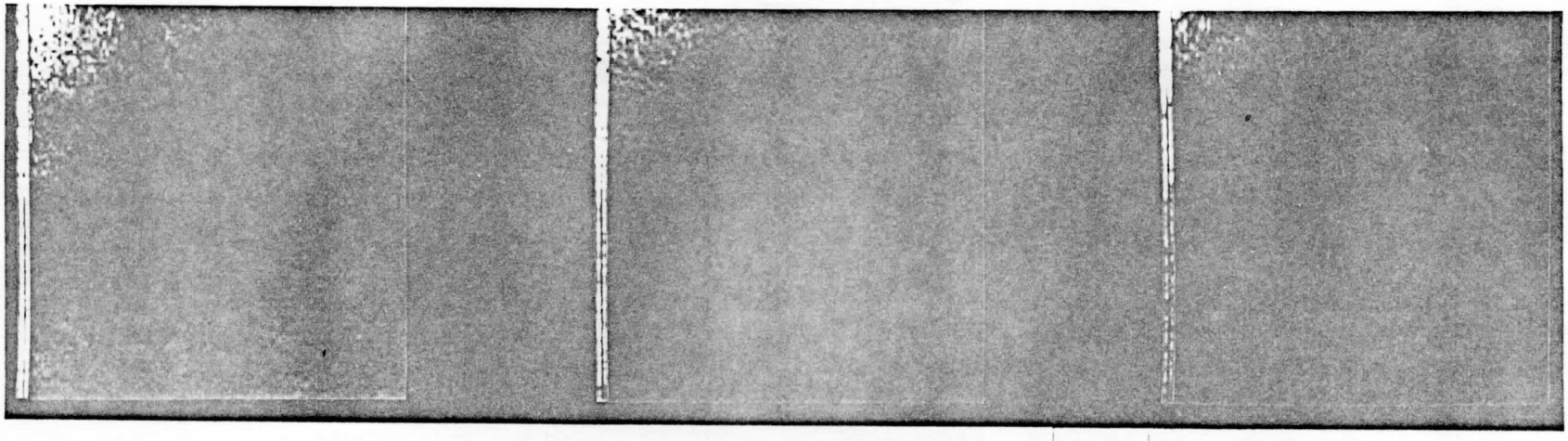

a) Apollo AS6-2-877
Quarter Picture: URQ

b) Apollo AS6-2-877
Quarter Picture: ULQ

c) Apollo AS6-2-948
Quarter Picture: LLQ

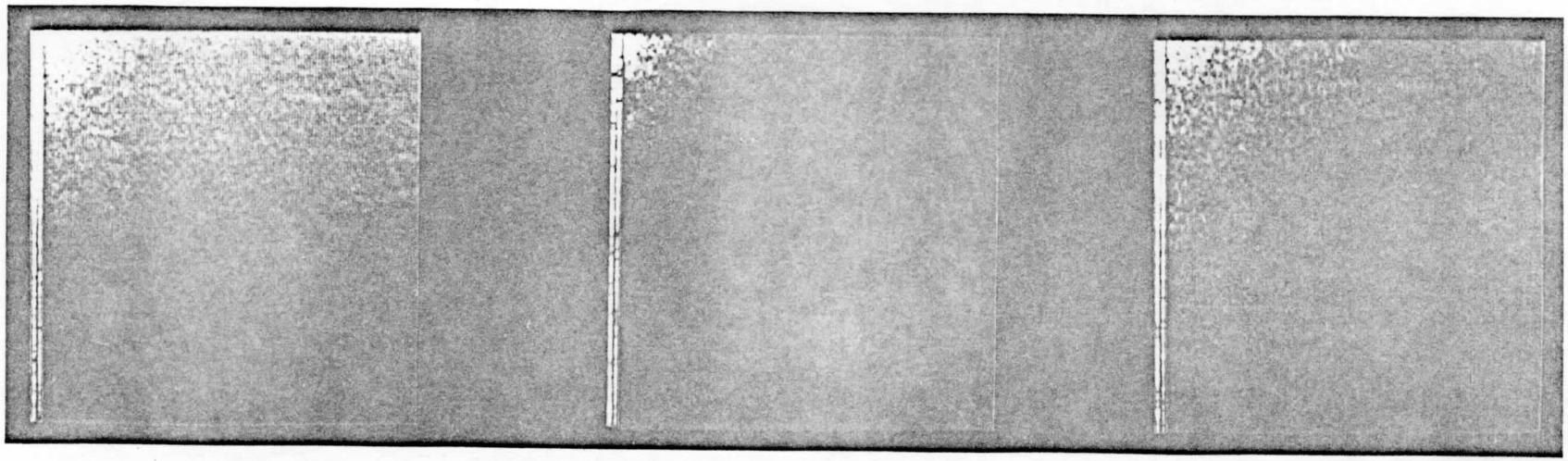

d) Apollo AS6-2-1064
Quarter Picture: URQ

e) Apollo AS6-2-1429
Quarter Picture: LRQ

f) Apollo AS6-2-1430
Quarter Picture: CRQ

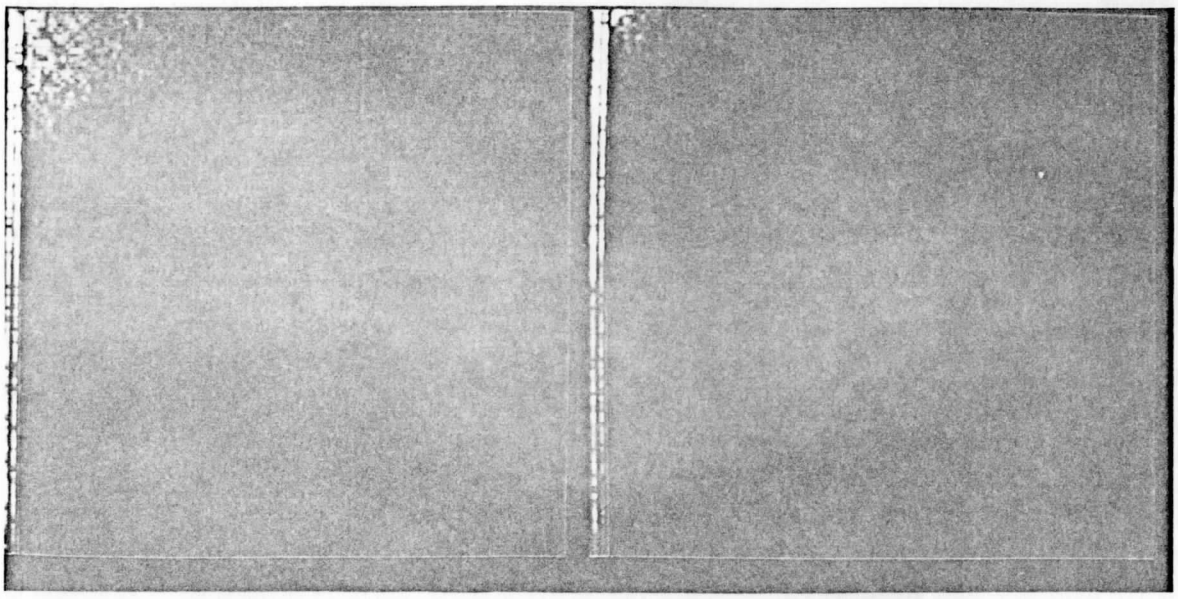

g) Apollo AS6-2-1467
Quarter Picture: LLQ

h) Apollo AS6-2-1469
Quarter Picture: LLQ

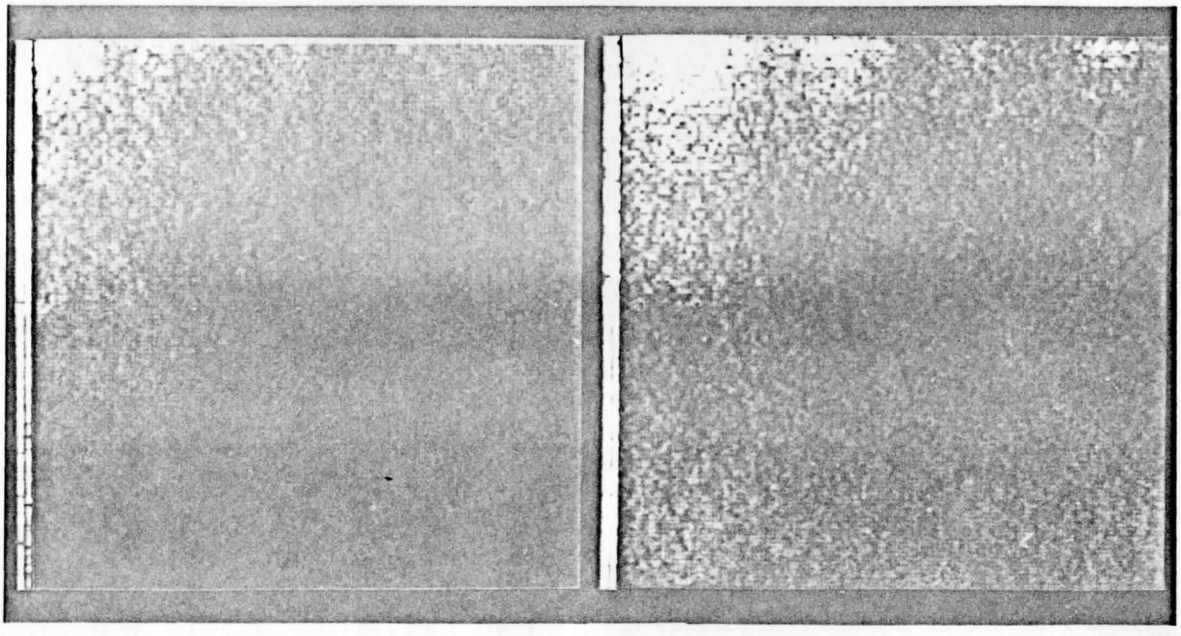

i) Apollo AS6-2-1484
Quarter Picture: CLQ

j) Apollo AS6-2-1484
Quarter Picture: CRQ

# CHAPTER 4

## ENCODING STUDIES USING TWO-DIMENSIONAL WALSH TRANSFORMS

The following serves to summarize our efforts on the encoding schemes for the eight visual channels of the geostationary Synchronous Meteorological Satellite (SMS), with particular emphasis on the work done after our report dated July 1, 1974 (also see Chapter 3). Selected pictures from Apollo VI have been encoded using the Walsh Hadamard Transform (WHT) and suitable quantization procedures have been studied. The pictures reconstructed using the various quantization procedures are shown to demonstrate an appreciable savings in bandwidth. Some new results are also presented. The feasibility of implementing the hardware on board the satellite for the proposed encoding methods is also discussed.

A simple block diagram of the WHT encoder is shown in Figure 4.1. Here

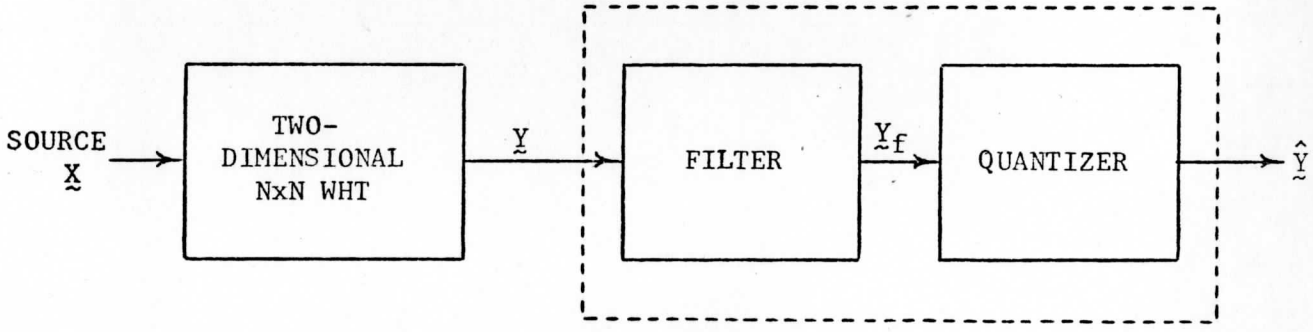


Figure 4.1 Block Diagram of the WHT Encoder.

$\underset{\sim}{X}$ is the NxN image matrix containing the desired picture elements (pels) and $\underset{\sim}{Y}$ is the NxN coefficient matrix containing Walsh coefficients:

$$\underset{\sim}{Y} = 1/N \cdot \underset{\sim}{W}\ \underset{\sim}{X}\ \underset{\sim}{W} \qquad (4.1)$$

where N = 8 for our proposed encoding schemes. The filter serves to delete the Walsh coefficients that are very small and therefore contain little significant information required for reconstructing the original image matrix $\underset{\sim}{X}$. (The filter in Figure 4.1 simply multiplies the elements $y_{ij}$ by either zero or one and so is not a filter in the conventional sense). The filtered version of the Walsh coefficients $y_{k\ell}$ ($k,\ell = 0,1,\ldots,$ N-1) are quantized for transmission through a digital communication channel using PCM. The received coefficients $\hat{y}_{k\ell}$ of $\hat{\underset{\sim}{Y}}$ are decoded and then used to obtain a close approximation to $\underset{\sim}{X}$ using the inverse transformation:

$$\hat{\underset{\sim}{X}} = 1/N\ .\ \underset{\sim}{W}\ \hat{\underset{\sim}{Y}}\ \underset{\sim}{W} \qquad (4.2)$$

In order to reproduce $\underset{\sim}{X}$ with negligible degradation in the reconstructed image quality, the filter and the quantizer have to be suitably chosen. Such choices are investigated and the results are presented below.

The 16 Walsh coefficients shown in Figure 4.2 (i.e., the region bounded by cross-hatched lines in Figure 4.2) are selected for encoding based on their Standard Deviation (SD) over an ensemble of 49,152 subpictures of 8 x 8 size (3 pictures: AS6-2-877,-934,-1430, each of 1024 x 1024 size)*.

---

* See Appendix C of our final report dated July 1, 1974 for a detailed discussion on the selection criteria.

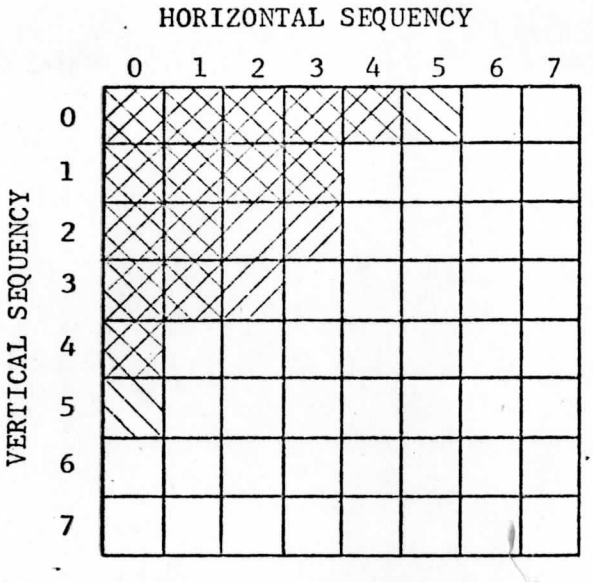


Figure 4.2 Selected Walsh Coefficients.*

Another equally good choice is shown by the diagonal lines in Figure 4.2 and the difference between the two choices in terms of encoding performance is quite insignificant. Each of the selected Walsh coefficients assumes values over different ranges. The first-order Probability Density Functions (PDF) for different coefficients are shown in Appendix C of our final report dated July 1, 1974. From the point of view of implementation, we impose the constraint that only one quantizer with characteristics symmetric about zero is to be used.

In order to quantize each of the selected coefficients with negligible quantization error, the coefficients have to be suitably scaled before quantization. The choice of suitable Scale Factors (SF) and the type of Quantizer (QTR) are studied through computer simulation and the simulation results are presented.

---

* "Sequency" here is defined to be the number of zero crossings.

Without any elaboration we state that for good subjective quality reconstructed images, it is desirable that [Andrews, H.C., 1970]:

1. For a given spatial sequency, the low amplitudes or values have to be more finely quantized;
2. For a given amplitude, the higher sequency coefficients have to be more finely quantized.

If each of the coefficients is divided by its corresponding S D and the resulting coefficients are quantized by a quantizer which has closely spaced output levels for lower amplitudes and relatively coarsely spaced output levels for higher amplitudes, then requirements (1) and (2) are almost met and the resulting reconstructed image quality will then be predominantly influenced by the low pass filtering (Figure 4.1) in the transformed domain. But such a procedure requires a priori the S D's of the encoded Walsh coefficients. So an expression of the form:

$$\hat{\sigma}_y^2(k,l) = a \exp[-(k^2+\ell^2)b] \qquad (4.3)$$

where $\hat{\sigma}_y(k,l)$ denotes the estimate of the S D of the Walsh coefficient with horizontal sequency k and vertical sequency $\ell$, is fitted to the actual computed ensemble S D's. It is found that such a fit is a reasonably good fit to the computed S D values.

The choices available for the quantizer are uniform (i.e. outputs are uniformly spaced), non uniform, and piecewise uniform quantizers. The quantizer outputs and the number of outputs have to be chosen so as to satisfy the chosen fidelity criterion (e.g. maximum entropy, minimum mean-squared error, etc.).

The input to the quantizer is the set of the scaled zero-mean Walsh coefficients with S D of unity and so the input is a random variable which takes on a wide range of values that are the set union of the values assumed

by the individual Walsh coefficients. From histograms of the Walsh coefficients, the PDF of the input to the quantizer is estimated to be Gaussian with a S D of nearly unity. Hence a uniform and a non uniform quantizer are designed which give rise to very little distortion and are also matched to the statistics. The number of quantizer output levels is fixed at 64 (6 bits) to conform to the present A/D converter in the SMS-I.

Another quantizer of interest is the SMS quantizer already in use in the SMS. It has a square-root-type companding law (See Philco-Ford Phase C design report, Volume I, June 30, 1971) which is desirable in view of our requirements (1) and (2) for good quality picture production. It is implemented as a piecewise uniform quantizer on board the satellite. Because the hardware has been built for the SMS quantizer, the proposal of a quantizer of the SMS quantizer type does not call for a new hardware design.

We now outline the different encoding schemes that are used to encode selected portions of the four Apollo VI pictures: AS6-2-877, -934, -1430 and AS6-2-1469. First the validity of the choice of the 16 Walsh coefficients in Figure 4.2 is demonstrated by reconstructing the pictures using only the 16 Walsh coefficients in Figure 4.2 with no quantization of the coefficient amplitudes. Other choices of encoding the Apollo VI picture AS6-2-877 using 24 and 32 coefficients are also compared to illustrate the degradation caused by Walsh domain filtering. Next the choices of the SF's and QTR's are studied by scaling and quantizing the 16 retained Walsh coefficients in Figure 4.2. The degradations introduced by the Walsh domain filtering and the quantization operations can thus be isolated. Certain definitions to aid recognition of the encoding schemes are given below.

## 4.1 Scale Factor (SF)

Type 1: The set of S D's of the Walsh coefficients computed only over one picture.

For example, when type 1 SF's are used to encode the 16 Walsh coefficients of the 8 x 8 subpictures of AS6-2-877, the S D of each Walsh coefficient computed over only the picture AS6-2-877 is used as a scale factor for that particular Walsh coefficient. Hence the type 1 SF's are adapted to the particular picture that is being encoded and so the set of type 1 SF's used to encode the picture AS6-2-934 will be different from that used to encode the picture AS6-2-877.

Type 2: The set of S D's of the Walsh coefficients computed over an ensemble of the three pictures AS6-2-877, -934 and AS6-2-1430 (3 x 128 x 128 = 49,152 subpictures of 8 x 8 size).

This set of type 2 SF's is the same for all the four pictures AS6-2-877, -934, -1430 and AS6-2-1469. This is a more realistic set of S D values because each of the pictures occupies only a fraction of the whole scene scanned by the satellite.

Type 3: The set of S D's in Equation 4.3 obtained by fitting an expression of the form: $a \exp[-(k^2+\ell^2)b]$ to the set of type 2 S D's.

The computed values of a and b are:

$$a = 51.20 \tag{4.4a}$$

$$b = 0.189 \tag{4.4b}$$

The set of type 3 SF's is used to encode the Walsh coefficients of the subpictures of AS6-2-1469 whose statistics are not considered in the computation of the type 2 S D's. Thus an a priori knowledge of the set of S D's of the Walsh coefficients is not required and the set of type 3

SF's may be used for a variety of scenes.

## 4.2 Quantizer (QTR)

Type A: A set of 32 uniformly spaced output levels on either side of zero (total of 64 outputs).

The output levels are so chosen as to minimize the mean squared error (MSE) between the input, whose first-order PDF is assumed to be a zero mean unit variance Gaussian, and the quantizer output. The optimum spacing of the quantizer outputs has been computed to be 0.10376. The associated MSE is 0.0009161234.

Type B: A set of 32 non-uniformly spaced output levels on either side of zero (total of 64 outputs).

Again, the output levels and also the corresponding thresholds are so chosen as to minimize the MSE between the input and the output. The thresholds and the corresponding outputs are not shown. The optimum (in the minimum MSE sense) non-uniform quantizer also gives rise to nearly the maximum output entropy. Unlike the type A uniform quantizer, the type B non-uniform QTR has closely spaced outputs for small input amplitudes and relatively coarsley spaced outputs for large input amplitudes. Thus the subjective quality of the reconstructed image may be expected to be slightly better than that of the image reconstructed using the type A QTR. The MSE of the type B QTR is 0.000522732, about 0·55 times the MSE of the type A QTR. But the type B QTR is harder to implement than the Type A QTR and a comparison of the reconstructed pictures will determine whether the additional complexity associated with implementing a type B QTR can be tolerated.

Type C: A set of 32 non-uniformly spaced output levels on either side of zero (total of 64 outputs)

The type C QTR, also referred to as the SMS QTR, differs from the type B QTR in that the input is first passed through a square root type compander and the compander output is quantized to 32 uniformly spaced outputs. It has been implemented on board the SMS as a piecewise uniform QTR. The associated MSE lies between the MSE's of the type B and the type A QTR's. The type C QTR also possesses the desirable characteristics of having closely spaced outputs for small input amplitudes.

## 4.3 Simulation Results

This describes some of the simulation results using selected Apollo VI picture data and the transform encoding methods described above.

### Effect of Walsh domain filtering:

Comparison of Figures 4.5(a) and 4.6(a) reveals that Figure 4.6(a) is nearly as good as Figure 4.5(a) and that the effect of retaining only the 32 largest variance Walsh coefficients is insignificant. Comparison of Figures 4.6(a) and 4.6(b) reveals that the latter has suffered a very small (hardly noticeable) loss in resolution and that a nearly faithful reproduction of the original image is possible retaining only the 23 largest variance Walsh coefficients. Figure 4.6(c) corresponds to a choice of 19 coefficients which are nearly the 19 largest variance coefficients. In Figure 4.6(c) the absence of high sequency coefficients shows up when one observes that the contours enclosing very small clouds are approximated by abrupt steps. This is analogous to reconstruction of a continuous curve from closely spaced points on the curve using a zero-order hold. Yet the shape of the contour

is preserved because the size of the subpicture is quite small (8 x 8). Because we do not take into account the correlation between the last column (or row) of a subpicture and the first column (or row) of its adjacent subpicture, there is an abrupt change in the average or DC level across the boundary between any two adjacent subpictures. This "checkerboard" effect can be minimized by averaging the brightness in the vicinity of the boundary between two adjacent subpictures.

Figure 4.9(a) is probably the limit to the extent of Walsh filtering. The undesirable "checkerboard" effect is due not only to the absence of high sequency components but also to the abrupt change in the average brightness across the boundary between adjacent subpictures. Nevertheless, it is deemed that the recognition of the existence of minute details is more important to the human observer than the actual minute details themselves and so no meaningful, essential information is lost for visual interpretation due to the Walsh filtering. Also it is possible to estimate, with moderate estimation error, the missing high sequency coefficients from the encoded lower sequency ones and an image enhancement is also possible. However, these techniques have not been experimentally verified by us through simulation.

It is concluded that a 4:1 bit reduction is possible (i.e., 2 bits/pel) without loss of any significant detail in the Apollo VI pictures. All the aforementioned comments also apply to Figures 4.10(a), 4.11(a) and 4.12(a) when one compares them with Figures 4.5(b), 4.5(c) and 4.5(d), respectively. The objectionable "checkerboard" effect is clearly visible in Figure 4.11(a) (note that Figure 4.5(c) has a lot of minute details), just visible over some portions in Figure 4.12(a),and not at all visible in Figure 4.10(a).

For Figure 4.11(a), some form of image enhancement is necessary; yet the existence of detail is clearly recognized in Figure 4.11(a).

Effect of the choice of the SF's:

To observe the above effect, it has to be isolated from the Walsh filtering effect, as only 16 out of the 64 Walsh coefficients are selected and quantized. So all the reconstructed pictures referred to hereafter in this section have to be compared with Figures 4.9(a), 4.10(a), 4.11(a) and 4.12(a).

Comparison of each of the Figures 4.9(b), 4.9(c), and 4.9(d) with Figure 4.9(a) reveals that with adequate quantization guaranteed by way of the use of the type B QTR, the choice of the type of SF's has practically no effect on the quality of reconstructed pictures. The same comments hold good for Figures 4.10(b), 4.10(c), 4.10(d), and Figures 4.11(b), 4.11(c) and 4.11(d). Because the type 1 SF's are adapted to the particular picture being encoded and the fact that the type 2 and type 3 SF's are as good as the type 1 SF's, the type 1 SF's are not essential and so need not be considered. The type 3 SF's are particularly attractive because no *a priori* knowledge of the SD's of the Walsh coefficients is assumed.

Effect of the choice of the QTR:

In this section only the type 2 and the type 3 SF's are used in the encoding of the 16 selected Walsh coefficients. Comparison of each of the Figures 4.9(c), 4.9(e) and 4.9(f) with Figure 4.9(a) reveals that there is practically no difference between the quality of these reconstructed pictures, as the quantization is adequate and nearly optimally done. Hence the added complexity in implementing the type B QTR need not be tolerated

as the type B QTR has no significant advantage (in terms of the quality of the reconstructed picture) over the other QTR's. Further reduction in the number of QTR output levels or different unequal length code-words for each Walsh coefficient are other possibilities to be considered for bit reduction. The latter is deemed to be too complex to implement while the former method is not desirable unless more high sequency Walsh coefficients are also encoded.

Present SMS visual channels use a 6-bit QTR of the same kind as the type C QTR considered here. Hence a QTR with 6-bit outputs (or 64 output levels) is recommended. Instead of considering a trade off between the number of encoded Walsh coefficients and the number of QTR outputs (assuming equal length code words), it is considered better to use a QTR with 6-bit outputs and utilize the correlation between the different Walsh coefficients to estimate the missing high sequency Walsh coefficients from the encoded ones.

The previous comments are applicable to Figures 4.10(d), 4.10(g), 4.10(h) and Figures 4.11(d), 4.11(g) and 4.11(h). In Figures 4.9(g) and 4.9(h) the type 3 SF's have been used. Comparison of Figures 4.9(g) and 4.9(h) with Figures 4.9(e) and 4.9(f), respectively, reveal that all the above conclusions on the effect of the type of the SF's and the QTR's on the quality of the reconstructed pictures are verified. The same conclusions hold good for 4.10(e), 4.10(f), 4.10(h) and 4.10(g) and Figures 4.11(e), 4.11(f), 4.11(h) and 4.11(g) Further verification of the above conclusions on the effect of the type of QTR used is done by comparison of Figures 4.12(a) 4.12(b) and 4.12(c). Hence, on the basis of the above conclusions, we recommend the use of the type 3 SF's and the type 3 QTR.

## 4.4 Further Results

A two dimensional NxN WHT can be done using a one dimensional $N^2 \times N^2$ WHT. The use of one dimensional $N^2 \times N^2$ WHT instead of the two dimensional NxN WHT has many advantages from the implementation point of view even though the number of operations is the same in both cases. In general, a two dimensional 8 x 8 WHT requires 384 operations (additions and subtractions) using the Cooley-Tukey matrix factorization algorithm. If only the 16 coefficients in Figure 4.2 are encoded, then only they need be computed and this results in a saving of about 42% of the original 384 operations. The same saving is achieved in the one dimensional 64 x 1 WHT.

The correlation between the Walsh coefficients of 8 x 8 and 4 x 4 subpictures is studied using suitable models for the first and also the second order statistics of the data. (In particular a two dimensional wide-sense Markov sequence is assumed for a model). It appears that the two dimensional 8 x 8 WHT is very effective in obtaining nearly uncorrelated Walsh coefficients because the off-diagonal terms in the covariance matrix of the Walsh coefficients are quite small. This leaves some doubt whether it is possible to estimate with some confidence the missing coefficients from the encoded ones. Further experiments are necessary to clarify this point, although it is to be borne in mind that the model used need not be suitable for all classes of subpictures. As discussed in Chapter 3, the conditions required on the data or image matrix $\underset{\sim}{X}$ for the magnitudes of some of the Walsh coefficients of the transformed matrix $\underset{\sim}{Y}$ to be equal to those of their transpose elements in $\underset{\sim}{Y}$, are not severe and are satisfied by a significant number of subpictures. Therefore we can modify the magnitudes of the retained Walsh coefficients (i.e., $y_{k\ell}$) as:

$$|y'_{k\ell}| = |y'_{\ell k}| = 1/2\ [|y_{k\ell}| + |y_{\ell k}|] \qquad (4.5)$$

while the signs of the $y'_{k\ell}$'s (modified $y_{k\ell}$'s) are the same as those of the $y_{k\ell}$'s.

Then we do the inverse WHT to see the effect on the reconstructed pictures. Comparison of the reconstructed pictures in Figs. 3.5(a),(b),(c) with the corresponding pictures in Figures 4.5(a), 4.5(b) and 4.5(c) reveals that the assumption in Equation 4.5 has resulted in negligible degradation, if any, of the quality of the reconstructed pictures. Hence only the coefficient $y'_{k\ell}$ and the signs of $Y_{k\ell}$ and $Y_{\ell k}$ need be encoded and it is not necessary to encode both $y_{k\ell}$ and $y_{\ell k}$. Suitable encoding schemes may be designed to utilize the above result. More work is needed in this regard.

Finally, a brief discussion of the feasibility of the implementation of the WHT on board the satellite is in order. Figure 4.13 has the block diagram of one of the eight identical visual channels. Each one of the eight channels is periodically sampled every 2μs (sampling frequency = 500 KHz). So at the end of 2μs eight samples (one from each channel) have been taken. For implementing a WHT, the current system may require a few modifications.

The pre-sampling filter low pass filters the video data to cut down the bandwidth as otherwise the aliasing error will be significant at this sampling rate. Since filtering is done in the Walsh domain, a pre-sampling filter may not be necessary. Perhaps the sampling rate may have to be increased slightly to reduce aliasing. See particulary [1973 SSEC Report] for recommendations on sampling rate. Since the sampling rate is tied to the satellite spin rate which is fixed, a pre-sampling filter is necessary to minimize aliasing. Assume for the present that the sampling period is 2μs. We propose a "64 x 1 dimensional WHT processor" in place of an 8 x 8 two dimensional WHT processor. A 64 x 1 one dimensional WHT processor is a special purpose digital system that accepts 64 samples and outputs the scaled versions of only the selected Walsh coefficients.

It takes 16 μs to obtain 64 samples (8 samples from each of the 8 channels). Computation of all the 64 Walsh coefficients requires a total of 64 $\log_2$ 64 = 384 additions or subtractions using the fast WHT and also frequent transfer of data from one storage element to the arithmetic unit and vice versa. So the logic circuitry that performs these computations has to be integrated if possible on a single silicon chip to avoid interconnections and the associated propagation delays. Also the choice of the devices and circuits may be made by emphasising if necessary speed of operation rather than power consumed during switching.

It is possible to reduce the number of additions or subtractions by computing only the coefficients to be encoded. As has been mentioned eariler, for the two dimensional WHT zonal coding procedure (4:1 sample reduction factor) in Figure 4.2, only 222 additions or subtractions are required as compared to the total 384 operations, a reduction of about 42% of the total number of operations. A similar reduction is possible for the 64 x 1 one dimensional WHT. It is difficult to determine whether the WHT operations can be done in real time or not. If not, a data buffer is required to store and process the data and the size of the buffer is determined by the sampling period (2μs) and the speed of computation of the WHT. But Elliott [Elliott, A.R., Y.Y. Shum, 1973] claims that computation of 64 Walsh coefficients can be accomplished in less than 200 nanoseconds using a high speed digital integrated circuit. Also "in place" algorithms that utilize the same memory elements that store the original data for storing intermediate results and eventually the Walsh coefficients can be used to reduce additional storage requirements. Other researchers have developed hardware to implement two dimensional WHT in real time and some of them have developed the hardware which are suitable for implementation on board the

satellite. Habibi [Habibi, A., and W. K. Pratt, 1974] discusses briefly the hardware for implementing a DCT by sampled analog operations using charge coupled devices and surface acoustic wave devices. All of the above researchers using a WHT use a two dimensional WHT. But use of a corresponding one dimensional WHT can reduce equipment complexity considerably. In view of the above references, we conjecture that a real time implementation of the 64 x 1 one-dimensional WHT on board the satellite is feasible with very little or no buffer storage. Also, Harmuth [Harmuth, H. F., 1972] mentions the possibility of a faster computational procedure using a logical Walsh transform.

The quantization of the selected WHT coefficients poses no problem from the implementation point of view as a bipolar version of the SMS quantizer is easy to implement.

The WHT has some advantages over the current system used in the SMS. Since the WHT coefficients are obtained by linear combination of the samples which are corrupted by the additive PMT noise, the transform process may average out the PMT noise. In particular the zero sequency component $y_{00}$ can be expected to be much less immune to the DMT noise and the reconstructed subpicture can be expected to be less noisy. If only 16 of the 64 coefficients are chosen for encoding, they may be transmitted at a slower rate (1/4 of the SMS sampling rate).

Obviously it is not possible to consider all implementation complexities. An attempt has been made only to demonstrate the feasibility of the WHT on board the satellite based on the SMS system constraints and the experiences of other researchers.

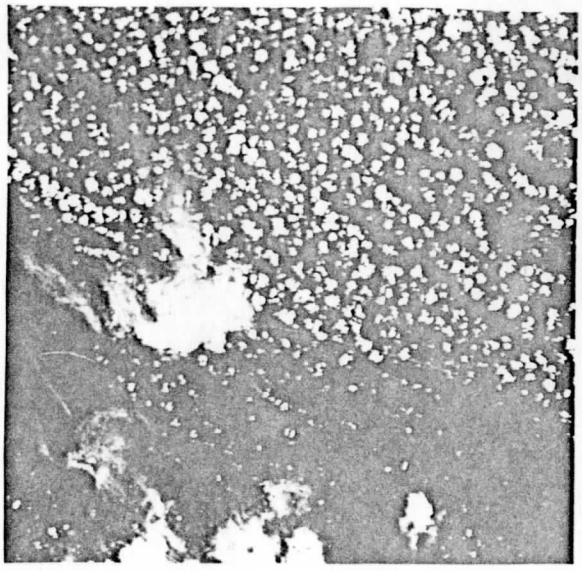

a) Lower right quarter of original Apollo AS6-2-877

b) Upper right quarter of original Apollo AS6-2-934

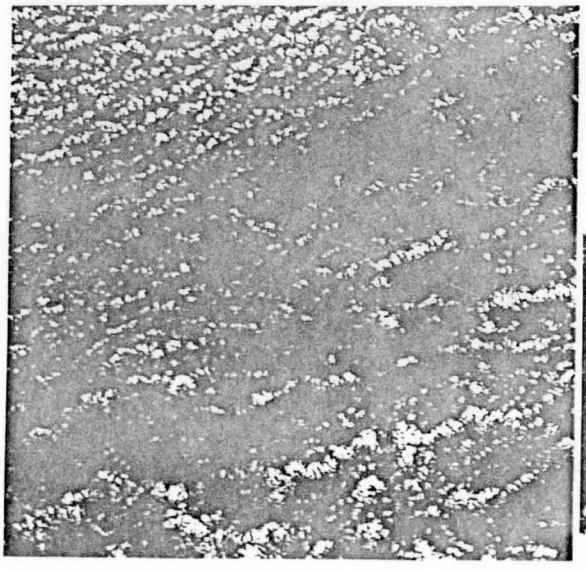

c) Central right quarter of original Apollo AS6-2-1430

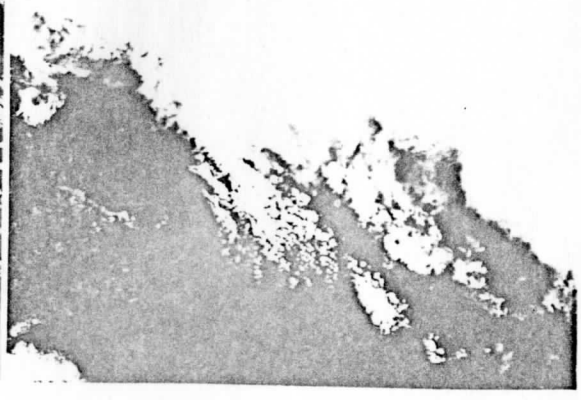

d) Lower right quarter of original Apollo AS6-2-1469

FIGURE 4.5

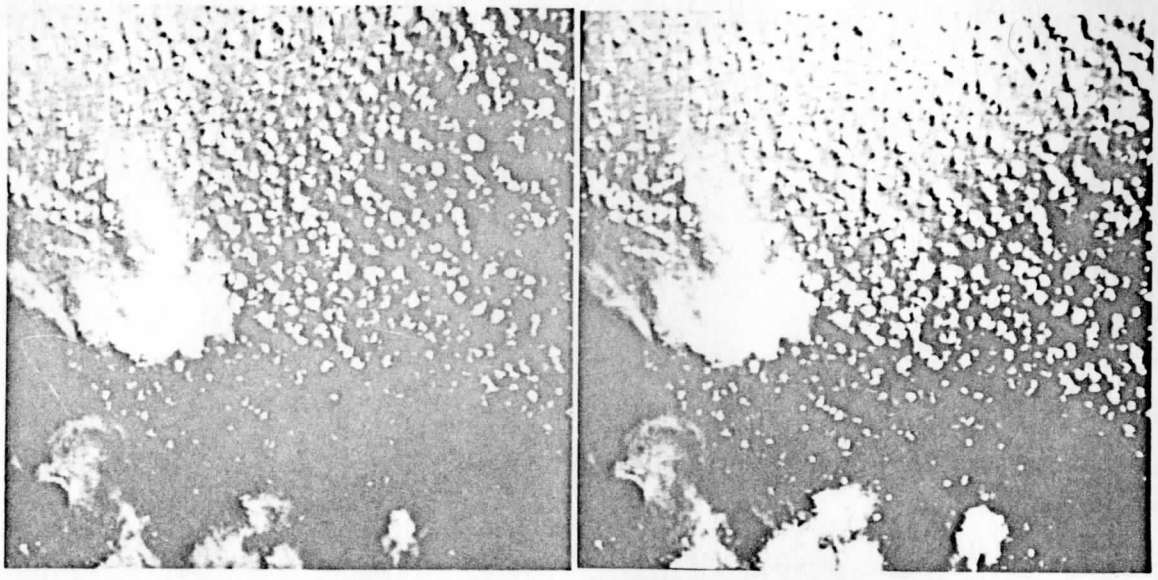

a) Reconstruction of Fig. 4.5a using only the 32 largest-variance Walsh coefficients in Fig. 4.4a (no quantizer used)

b) Reconstruction of Fig. 4.5a using only the 23 largest-variance Walsh coefficients in Fig. 4.4b (no quantizer used)

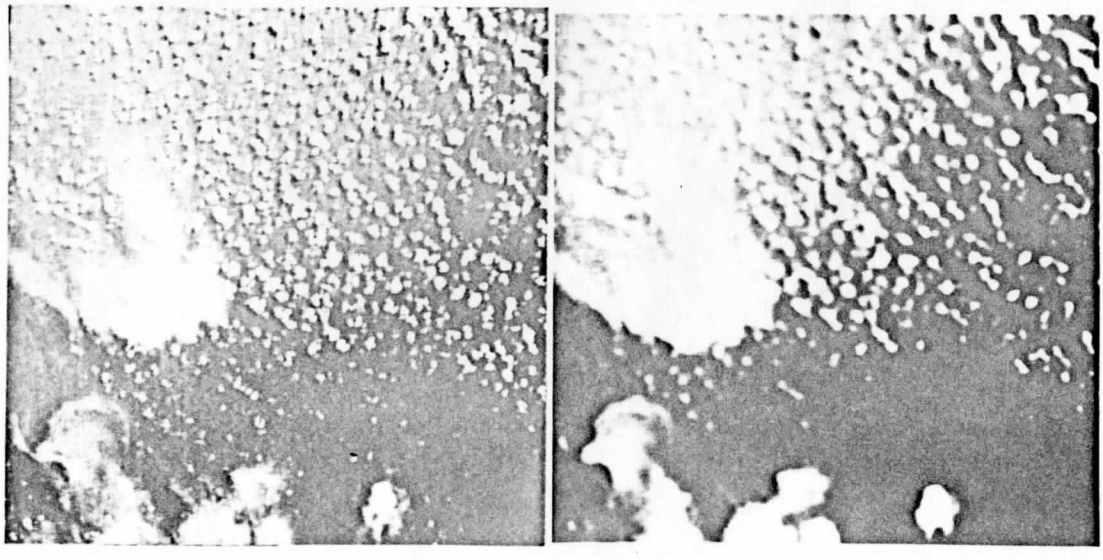

c) Reconstruction of Fig. 4.5a using only the 19 largest-variance Walsh coefficients in Fig. 4.4c (no quantizer used)

d) Reconstruction of Fig. 4.5a after filtering by simulated SMS optics

FIGURE 4.6

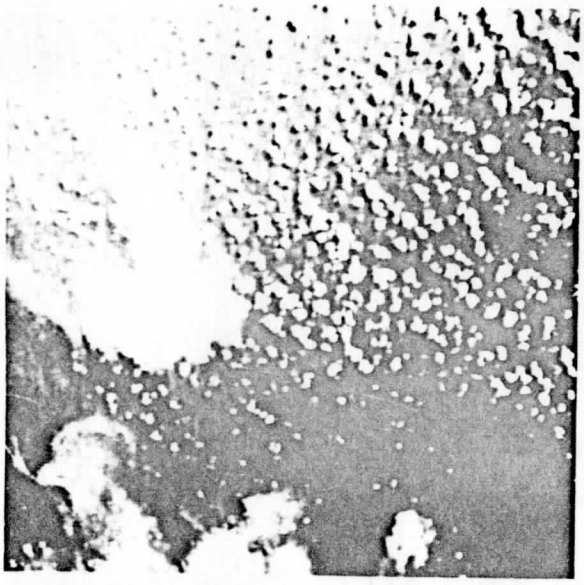

a) Reconstruction of Fig. 4.5a
using only the 23 Walsh coefficients
in Fig. 4.4b, NOPT QTR

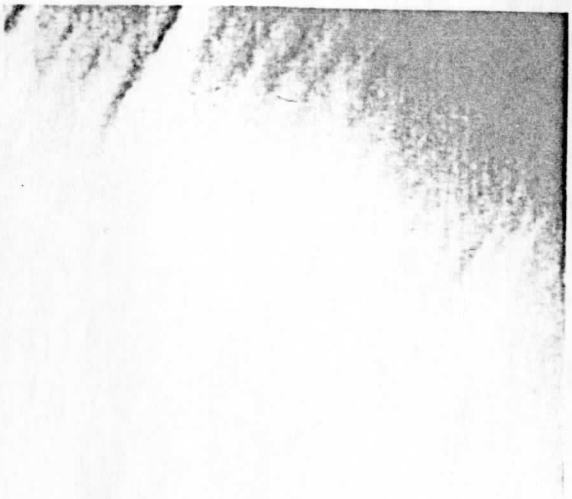

b) Reconstruction of Fig. 4.5b
using only the 23 Walsh coefficients
in Fig. 4.4b, NOPT QTR

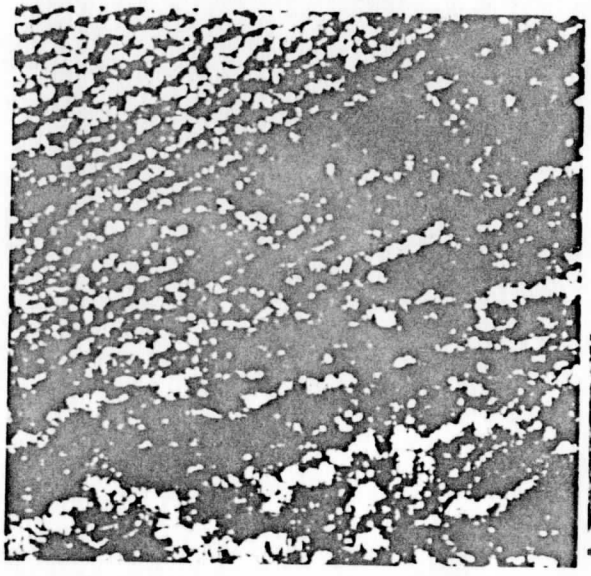

c) Reconstruction of Fig. 4.5c
using only the 23 Walsh coefficients
in Fig. 4.4b, NOPT QTR

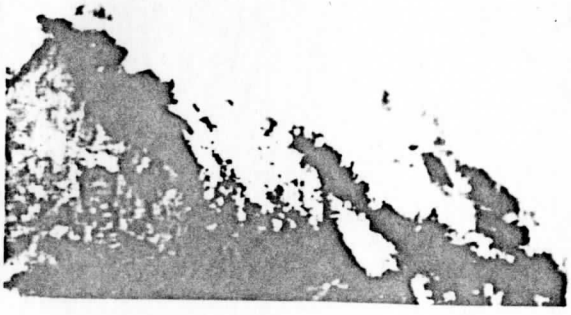

d) Reconstruction of Fig. 4.5d
using only the 23 Walsh coefficients
in Fig. 4.4b, NOPT QTR

FIGURE 4.7

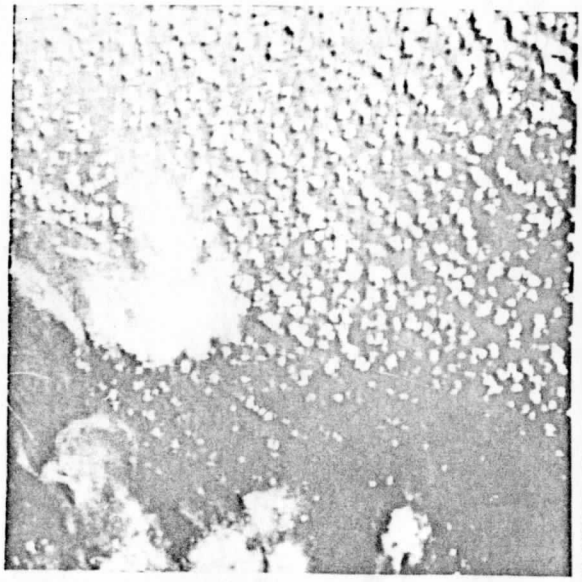

a) Reconstruction of Fig. 4.5a using only the 16 Walsh coefficients in Fig. 4.4d (no quantizer)

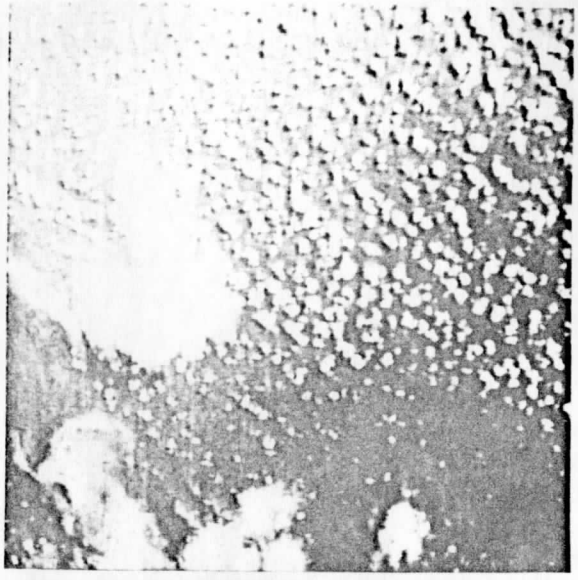

b) Reconstruction of Fig. 4.5a using only the 16 Walsh coefficients in Fig. 4.4d, Type 1 SF, Type B QTR

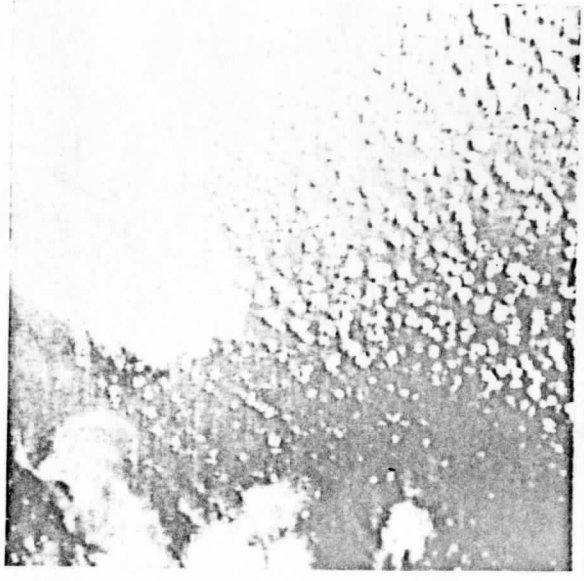

c) Reconstruction of Fig. 4.5a using only the 16 Walsh coefficients in Fig. 4.4d, Type 2 SF, Type B QTR

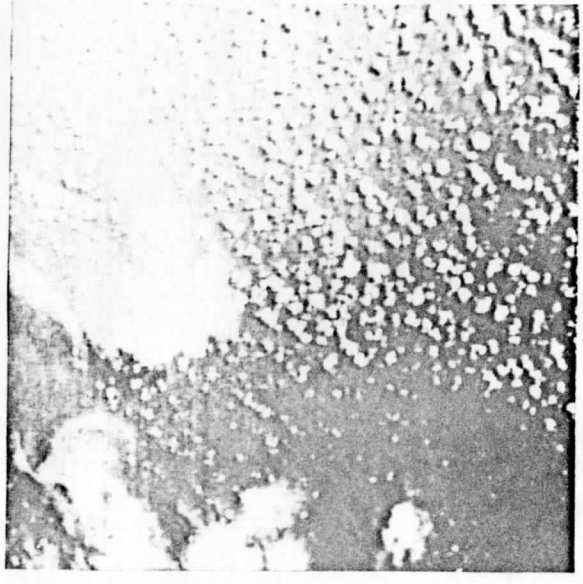

d) Reconstruction of Fig. 4.5a using only the 16 Walsh coefficients in Fig. 4.4d, Type 3 SF, Type B QTR

FIGURE 4.9

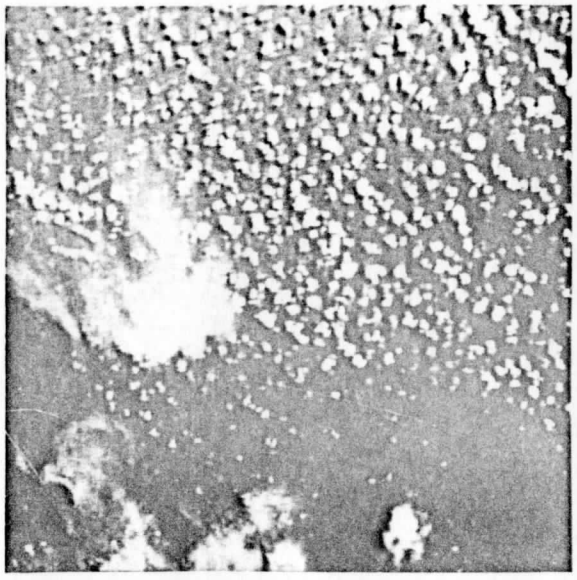

e) Reconstruction of Fig. 4.5a using only the 16 Walsh coefficients in Fig. 4.4d, Type 2 SF, Type A QTR

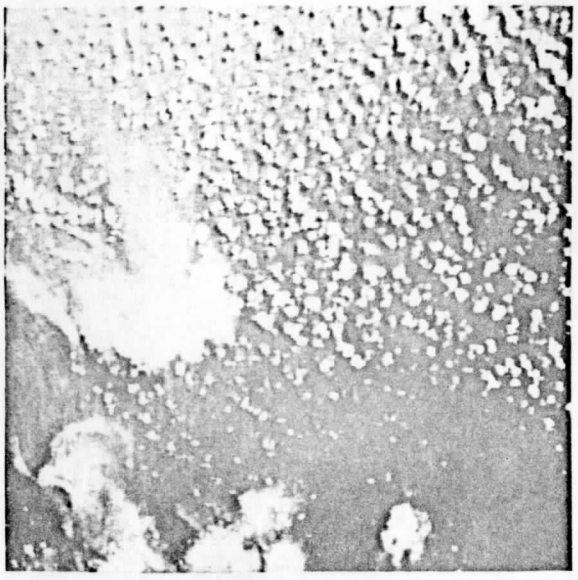

f) Reconstruction of Fig. 4.5a using only the 16 Walsh coefficients in Fig. 4.4d, Type 2 SF, Type C QTR

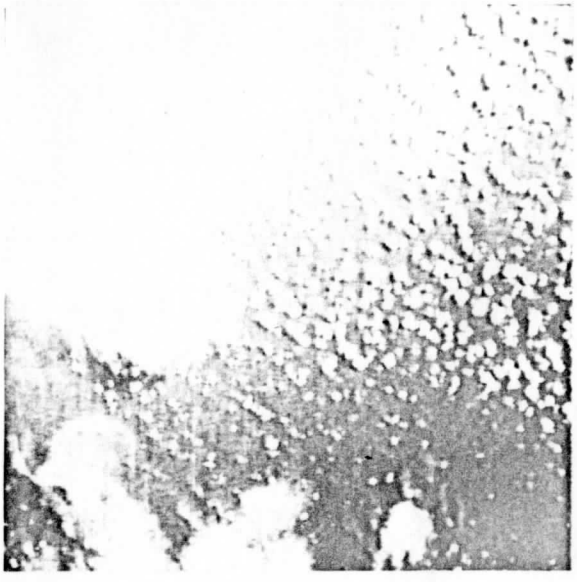

g) Reconstruction of Fig. 4.5a using only the 16 Walsh coefficients in Fig. 4.4d, Type 3 SF, Type A QTR

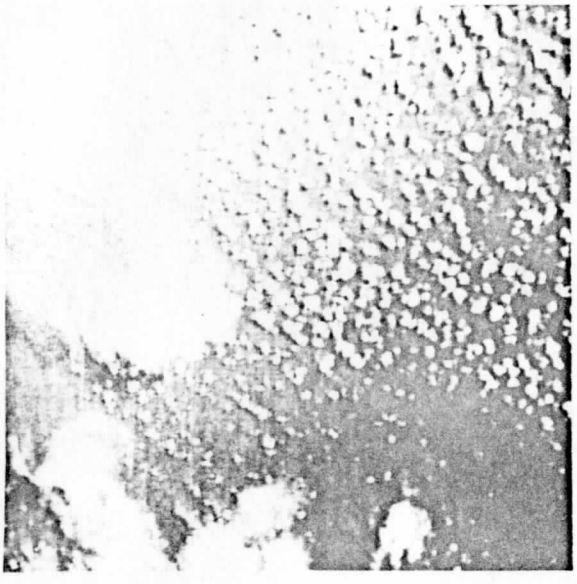

h) Reconstruction of Fig. 4.5a using only the 16 Walsh coefficients in Fig. 4.4d, Type 3 SF, Type C QTR

FIGURE 4.9 (cont'd)

a) Reconstruction of Fig. 4.5b using only the 16 Walsh coefficients in Fig. 4.4d (no quantizer used)

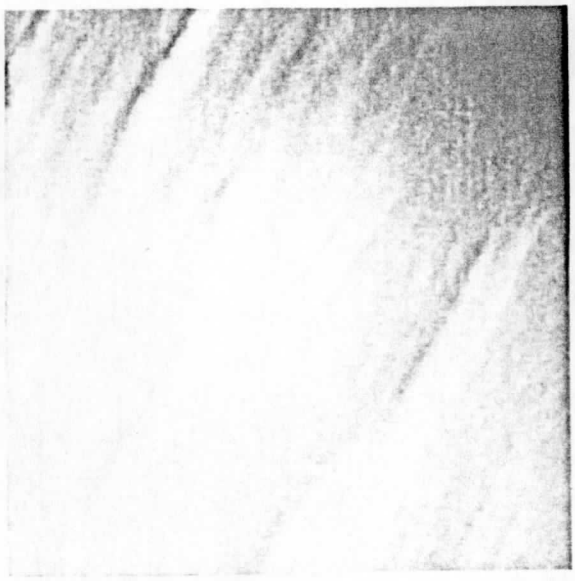

b) Reconstruction of Fig. 4.5b using only the 16 Walsh coefficients in Fig. 4.4d, Type 1 SF, Type B QTR

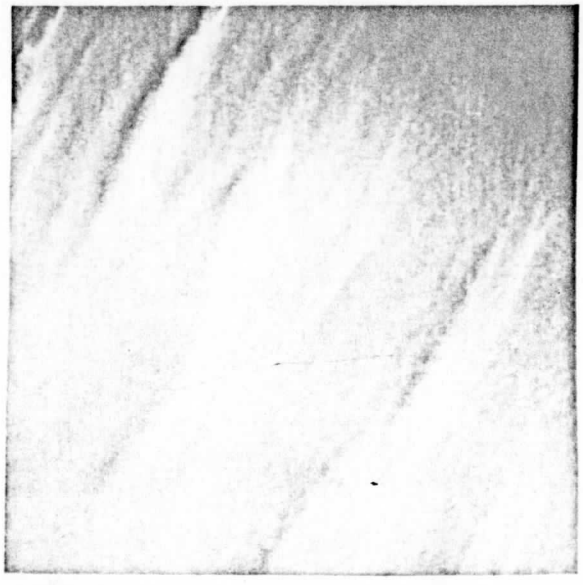

c) Reconstruction of Fig. 4.5b using only the 16 Walsh coefficients in Fig. 4.4d, Type 2 SF, Type B QTR

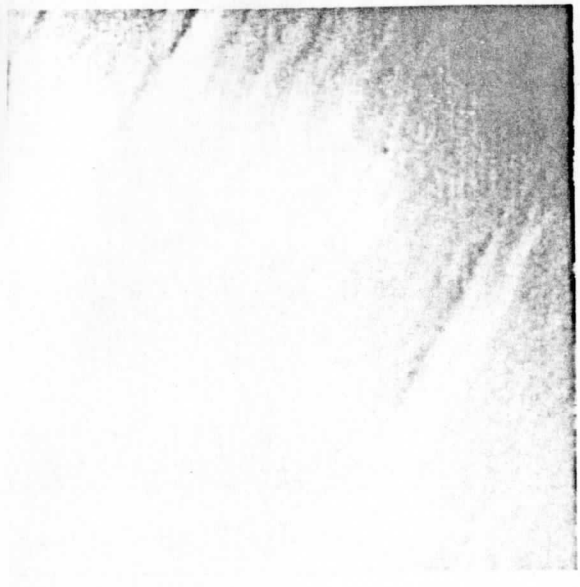

d) Reconstruction of Fig. 4.5b using only the 16 Walsh coefficients in Fig. 4.4d, Type 3 SF, Type B QTR

FIGURE 4.10

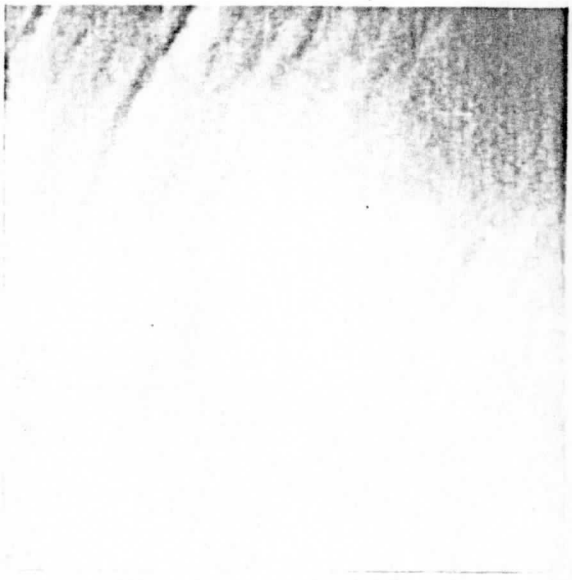

e) Reconstruction of Fig. 4.5b
using only the 16 Walsh coefficients
in Fig. 4.4d, Type 2 SF, Type A QTR

f) Reconstruction of Fig. 4.5b
using only the 16 Walsh coefficients
in Fig. 4.4d, Type 2 SF, Type C QTR

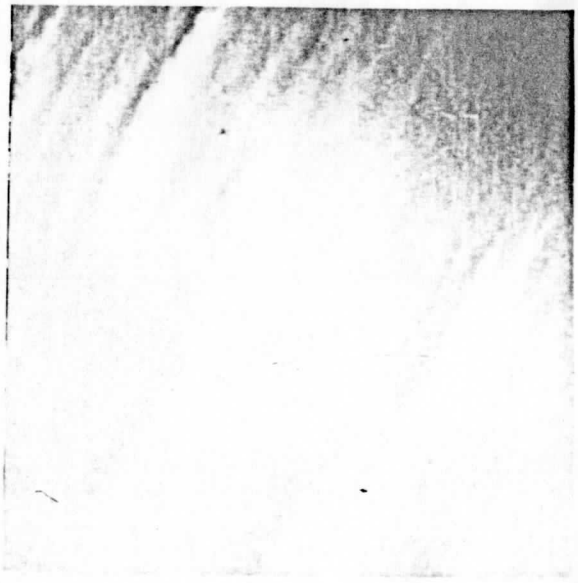

g) Reconstruction of Fig. 4.5b
using only the 16 Walsh coefficients
in Fig. 4.4d, Type 3 SF, Type A QTR

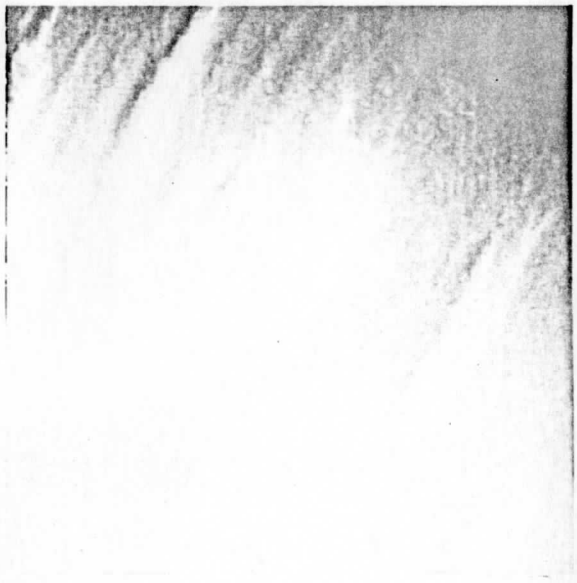

h) Reconstruction of Fig. 4.5b
using only the 16 Walsh coefficients
in Fig. 4.4d, Type 3 SF, Type C QTR

FIGURE 4.10 (cont'd)

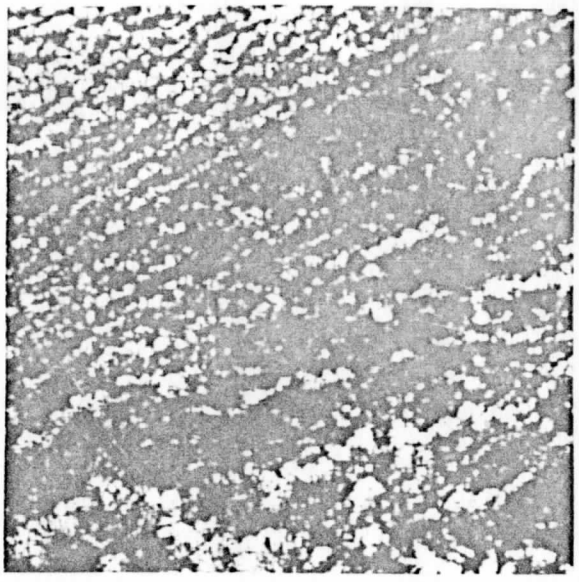

a) Reconstruction of Fig. 4.5c using only the 16 Walsh coefficients in Fig. 4.4d (no quantizer)

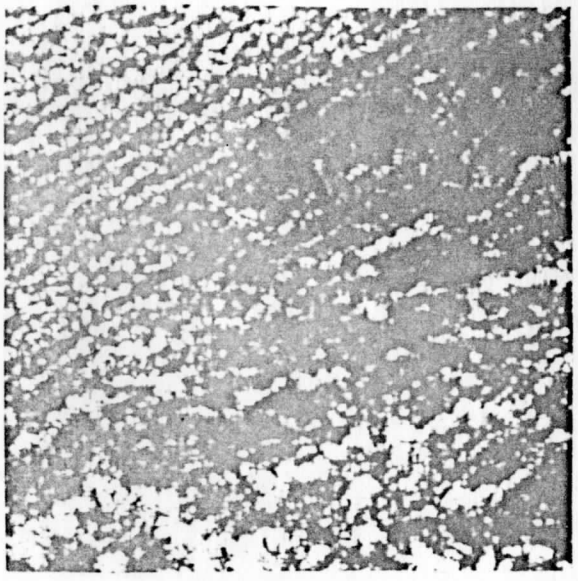

b) Reconstruction of Fig. 4.5c using only the 16 Walsh coefficients in Fig. 4.4d, Type 1 SF, Type B QTR

c) Reconstruction of Fig. 4.5c using only the 16 Walsh coefficients in Fig. 4.4d, Type 2 SF, Type B QTR

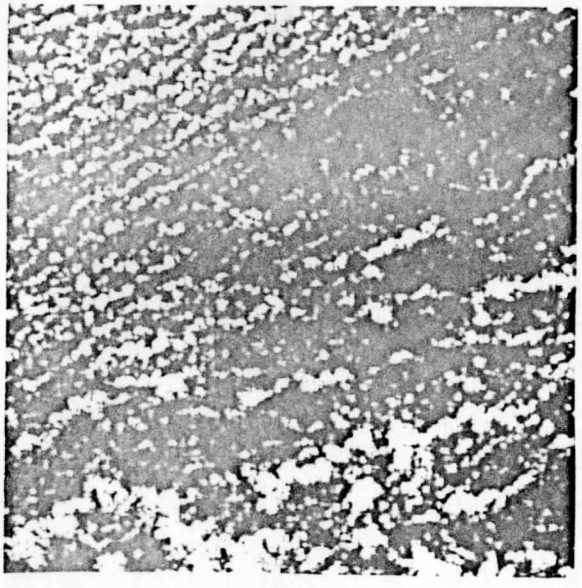

d) Reconstruction of Fig. 4.5d using only the 16 Walsh Coefficients in Fig. 4.4d, Type 3 SF, Type B QTR

FIGURE 4.11

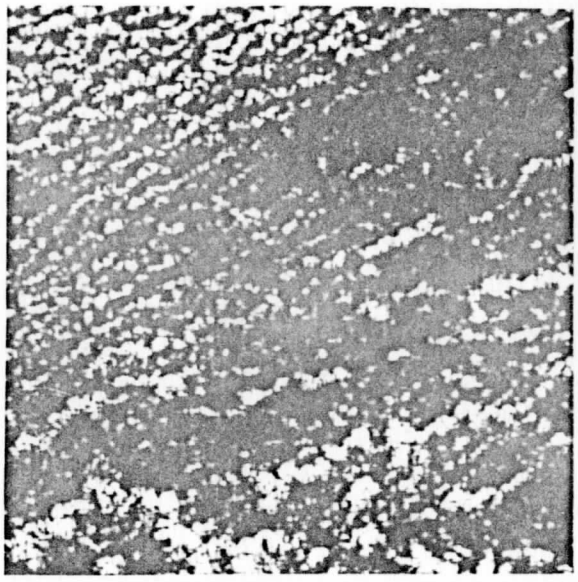

e) Reconstruction of Fig. 4.5c using only the 16 Walsh coefficients in Fig. 4.4d, Type 2 SF, Type A QTR

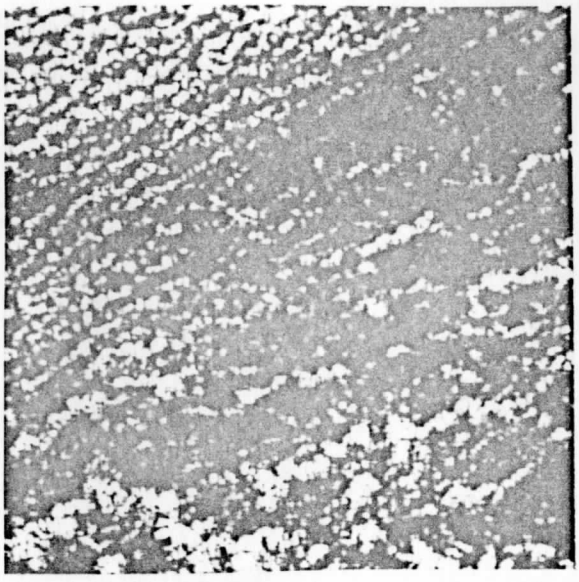

f) Reconstruction of Fig. 4.5c using only the 16 Walsh coefficients in Fig. 4.4d, Type 2 SF, Type C QTR

g) Reconstruction of Fig. 4.5c using only the 16 Walsh coefficients in Fig. 4.4d, Type 3 SF, Type A QTR

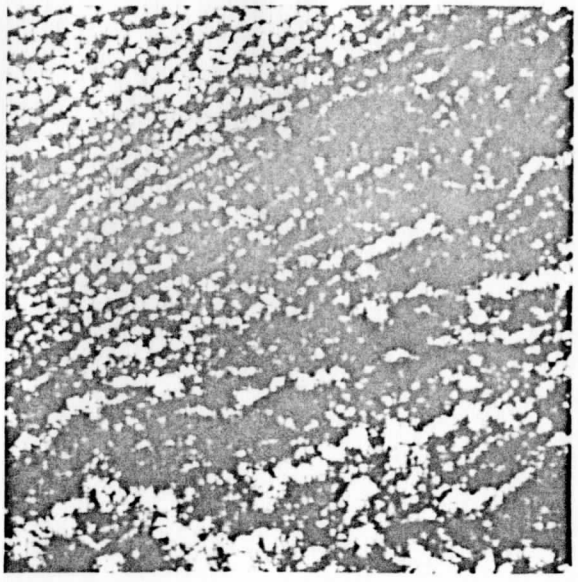

h) Reconstruction of Fig. 4.5c using only the 16 Walsh coefficients in Fig. 4.4d, Type 3 SF, Type C QTR

FIGURE 4.11 (cont'd)

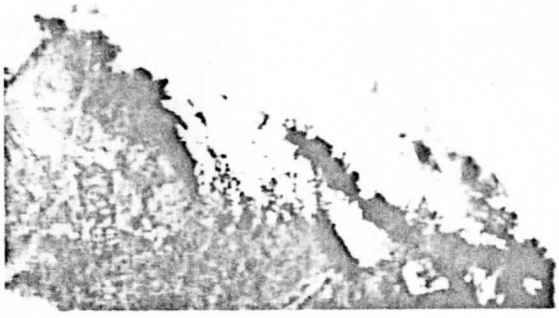

a) Reconstruction of Fig. 4.5d using only the 16 Walsh coefficients in Fig. 4.4d (no quantizer used)

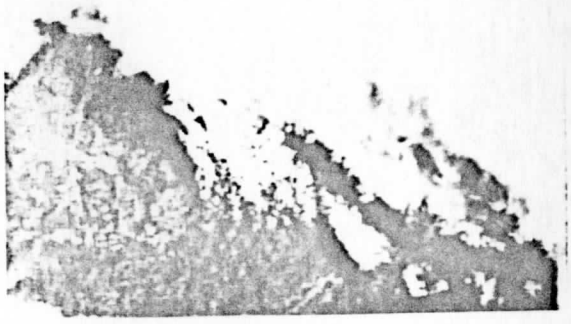

b) Reconstruction of Fig. 4.5d using only the 16 Walsh coefficients in Fig. 4.4d, Type 3 SF, Type A QTR

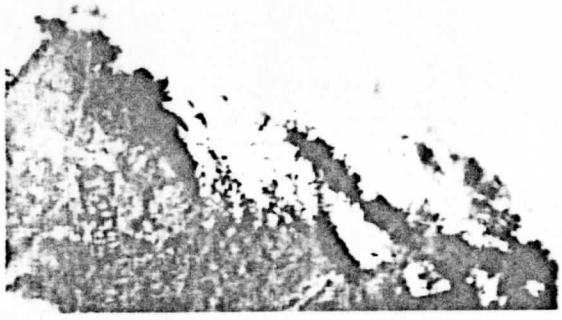

c) Reconstruction of Fig. 4.5d using only the 16 Walsh coefficients in Fig. 4.4d, Type 3 SF, Type B QTR

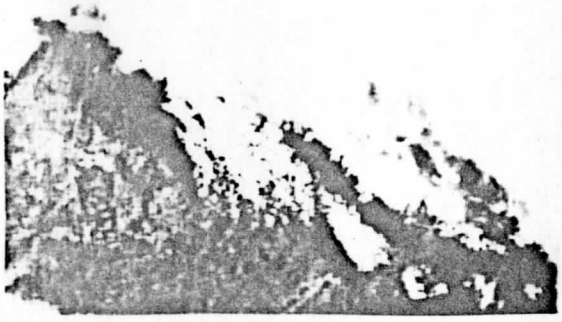

d) Reconstruction of Fig. 4.5d using only the 16 Walsh coefficients in Fig. 4.4d, Type 3 SF, Type C QTR

FIGURE 4.12

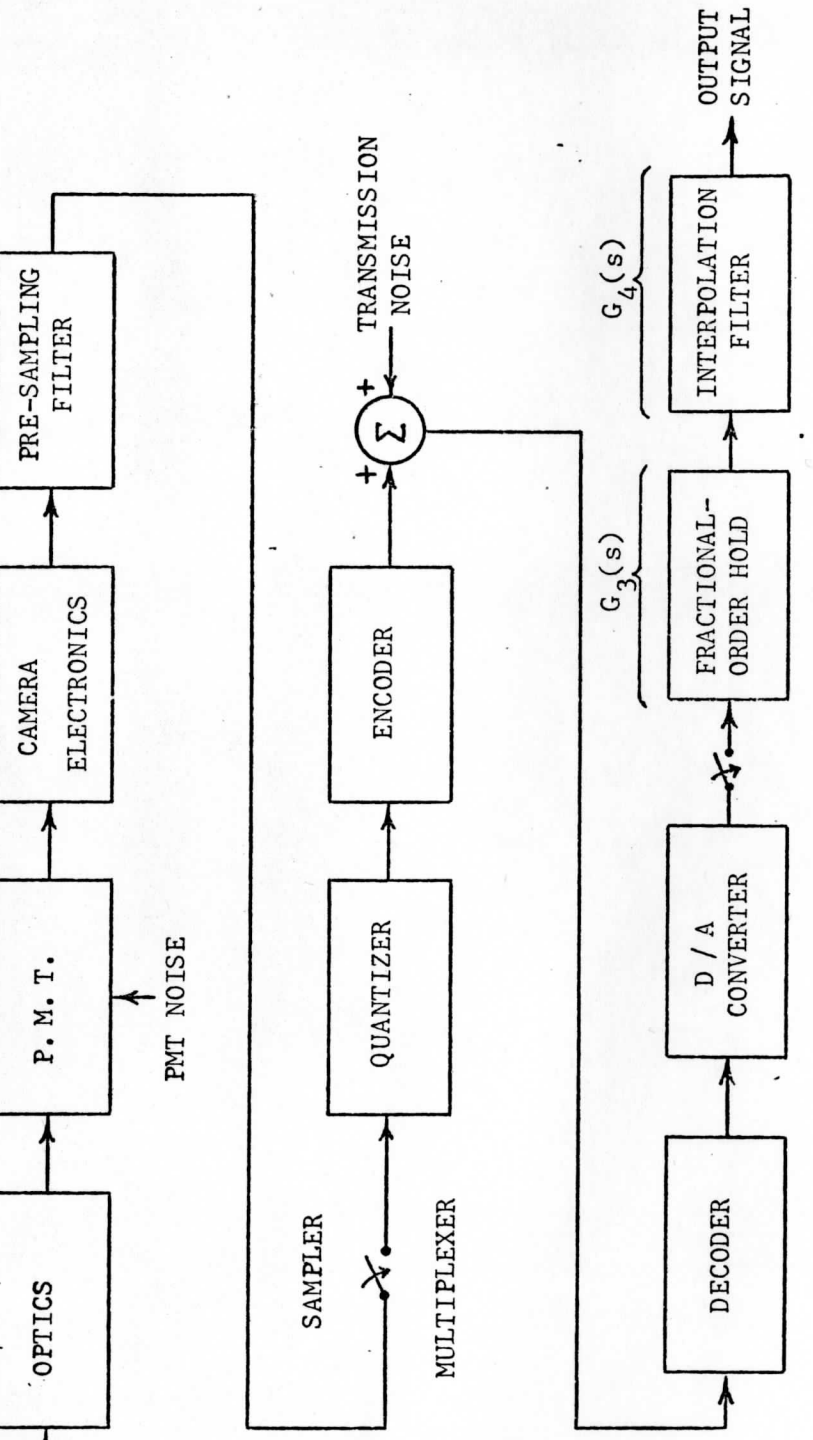


Figure 4.13 Block Diagram of the S.M.S. Visual Channels.

# CHAPTER 5

## CONCLUSIONS

Based only on the MTF data, a minimum-mean-square-error estimator can provide estimates of radiance step changes based on one or two IFOV's. A normalized step signal to rms noise of about 30 is required to make the measurement to an accuracy of 0.1%. The most important parameter is the correct number of observation (sample) points because the algorithm must tailor its response based on this parameter. Therefore the problem becomes more one of estimating the correct observation interval and the compound problem quickly becomes complex. The motivation here has been to provide some bounds on the performance.

Encoding using the two-dimensional Walsh transform is efficient in bandwidth conservation and the 8 x 8 transform seems to be well suited for this purpose. The coefficient selection and quantization rules developed here are easy to implement and provide good and consistent performance without the hazards of adaptive processing using on-board computers. The symmetry relations permit increased efficiency and the use of the one-dimensional processing scheme developed here for the two-dimensional Walsh transform holds promise for satellite applications. The required implementation steps are well within current satellite technology.

## REFERENCES


1. Andrews, H.C., Computer Techniques in Image Processing, Academic Press, N.Y., 1970.

2. Brown, W.M., Analysis of Linear Time-Invariant Systems, McGraw-Hill, N.Y., 1963

3. Elliot, A.R., Y.Y. Shum, "A Parallel Array Hardware Implementation of the Fast Hadamard and Walsh Transforms", Proc. Applications of Walsh Functions Symposium, Wash., D.C., March 1973, 181-183.

4. GSFC Specification, "Advanced Very High Resolution Radiometer (AVHRR)", GSFC S-731-P-118 REV D, July 1974.

5. Habibi, A., W.K. Pratt et al, "Real Time Redundancy Reduction using Transform Coding Techniques," ICC Conf. Record, 18A1-8, Minneapolis, June 1974.

6. Harmuth, H.F., Transmission of Information by Orthogonal Functions, Second Ed., Springer-Verlag, Berlin/N.Y., 1972.

7. Philco-Ford, Phase C Design Report, Vol. I, June 30, 1971.

8. Sage, A.P. and J.L. Melsa, Estimation Theory with Applications to Communications and Control, McGraw-Hill, N.Y., 1971.

9. Stremler, F.G., G.R. Redinbo et al, "Visual Channel Data Analysis for a Synchronous Meteorological Satellite," NOAA Final Report on NG-26-72, July 1973, Space Science & Engineering Center, The University of Wisconsin; revised copy available from The University of Wisconsin Press, Box 1379, Madison, Wis. 53701 and dated February 1974.

10. Stremler, F.G., G.R. Redinbo et al, "A Study of Applicable Encoding Methods for a Geostationary Orbiting Experimental Satellite," NOAA Final Report on 3-35372, July 1974, Space Science & Engineering Center, The University of Wisconsin, Madison, Wis. 53706; revised copy dated February 1975.

11. Van Trees, H.L., Detection, Estimation, and Modulation Theory, Part I, John Wiley & Sons, Inc., N.Y., 1968.

APPENDIX A

# GROUND MAPPING RESOLUTION ACCURACY OF A SCANNING RADIOMETER FROM A GEOSTATIONARY SATELLITE

by

Mohsen A. Khalil, Ferrel G. Stremler, and Robert J. Parent

## Abstract

Measures of the spatial and spatial rate (frequency) mapping of scanned visual imagery from an earth reference system to a spin-scan geostationary satellite are examined. Mapping distortions and coordinate inversions to correct for these distortions are formulated in terms of geometric transformations between earth and satellite frames of reference. Probabilistic methods are used to develop relations for obtainable mapping resolution when coordinate inversions are employed.

This work was supported by NOAA under Grants NG-26-72, 3-35372.

M. A. Khalil is presently with the Image Processing Institute, University of Southern California, Los Angeles, California 90007.

F. G. Stremler is with the Space Science and Engineering Center and the Department of Electrical and Computer Engineering, University of Wisconsin, Madison, Wisconsin 53706.

R. J. Parent is with the Instrumentation Systems Center and the Department of Electrical and Computer Engineering, University of Wisconsin, Madison, Wisconsin 53706.

# I. INTRODUCTION

Use of the spin-stabilized geostationary satellite for scan-type imaging is of continuing importance in remote meteorological sensing. Satellite measurements made using the spin-scan principle are in terms of angular displacements of the satellite whereas global measurements are usually referenced in terms of longitude and latitude. Here we examine the relationships between the two frames of reference and the inherent accuracy limitations and distortions introduced in the coordinate transformation.

The spin-stabilized geostationary satellite is placed in a synchronous orbit approximately 22,300 miles above the earth's surface. At this altitude, its orbital angular velocity matches the rotational angular velocity of the earth so that its position relative to features on the earth's surface is fixed if its orbit is truly equatorial. The satellite is rotated about its axis, which is perpendicular to the orbit plane, at a constant angular rate such that a perpendicular to the spin axis scans across the earth's surface along an east-west or west-east (equatorial) line. The azimuth of the scan angle measured from the line joining the centers of the earth and satellite is labeled as the angle $\beta$ in Fig. 1. An optical aperture and lens on the satellite is used to focus radiation received from sequential elements of a scan onto a photomultiplier tube. The resulting electrical signal is filtered, sampled and digitized for transmission to a ground terminal. To scan the earth's surface in latitude as well as longitude, a stepping mirror deflects the received radiation in the instantaneous field of view (IFOV) of the satellite at a different angle on each rotation. This mirror tilt angle is labeled as the angle $\alpha$. A series of successive scans can be used to reconstruct a replica of the observed scene in terms of the angles $\alpha$, $\beta$.

Imagery on the earth's surface is measured in terms of a longitudinal angle $\theta$ and a latitude angle $\phi$. These angles are measured in the earth's frame

of reference. The transformation between the two reference systems is quite linear for small nadir angles from the subsatellite point and becomes quite nonlinear near the earth's perimeter viewed from the satellite. Some of these effects have been investigated previously for the ATS series of geostationary satellites and were reported in some unpublished work [1]. Some relations of viewing angles in the earth's frame of reference have been published recently in a note by F. Smith [2]. The purpose of this work is to extend some of these results with particular emphasis on a sensitivity analysis of the coordinate transformation between frames of reference in the presence of spatial errors. This has application to the use of computer methods for use of transformations to remove geometrical distortions from imagery viewed from a geostationary satellite.

## II. GEOMETRICAL SCALING AND DISTORTION EFFECTS

In this section we develop geometrical relations between the earth coordinates and the satellite coordinates and the rate of change (frequency) between them. The derivation is restricted to the case of a spin-stabilized geostationary satellite and a spherical earth.

The earth coordinate system is measured in terms of a longitude angle $\theta$ and a latitude angle $\phi$. The satellite coordinate system is measured in terms of a spin-scan angle $\beta$ and a mirror tilt angle $\alpha$. The satellite scanner measures the incident radiation in terms of $\alpha$, $\beta$ and this can be used to estimate the imagery in $\theta$, $\phi$. However, $\dot{\beta}$ is constant so that unequal amounts of time are spent in different parts of the hemisphere, resulting in a nonuniform spatial resolution. Two items of interest are the coordinate mapping from $(\alpha,\beta)$ into $(\theta,\phi)$, and the frequency conversion factor from one reference system to the other.

Let R be the distance between the centers of the earth and the satellite and r be the radius of the earth, as shown in Fig. 2. Also, let $R_1$ be

the distance between the observed point on the surface of a spherical earth and the satellite. In equation form, this can be expressed as:

$$R_1 = R\cos\alpha\cos\beta - \sqrt{r^2 - R^2\sin^2\alpha - R^2\cos^2\alpha\sin^2\beta} \quad (1)$$

The satellite scanner senses incident radiation in the $(\alpha,\beta)$-frame of reference. Imagery is measured in the $(\theta,\phi)$-frame of reference. The mapping between the two can be expressed as:

$$\sin\alpha = \frac{\varepsilon\sin\phi}{\sqrt{1 + \varepsilon^2 - 2\varepsilon\cos\phi\cos\theta}} \quad (2)$$

$$\tan\beta = \frac{\varepsilon\cos\phi\sin\theta}{1 - \varepsilon\cos\phi\cos\theta} \quad (3)$$

In these equations, $\varepsilon$ is the ratio of the earth radius to the radius of a geostationary orbit:

$$\varepsilon = r/R = 0.151 \quad (4)$$

A spherical earth is assumed and for the mapping of a point on its surface to be visible from the satellite we insist that the following inequality holds:

$$\cos\theta\cos\phi \geq \varepsilon \quad (5)$$

In the neighborhood of the subsatellite point (i.e., that point at which: $\theta = 0$, $\phi = 0$), the measured imagery in $(\alpha,\beta)$ can be interpreted directly in terms of $(\theta,\phi)$, the constant of proportionality being the constant: $(1-\varepsilon)/\varepsilon$. Thus we can write:

$$\left\{\begin{matrix}[(1-\varepsilon)/\varepsilon]\alpha \rightarrow \phi \\ [(1-\varepsilon)/\varepsilon]\beta \rightarrow \theta\end{matrix}\right\} \quad (6)$$

This mapping is quite linear for small nadir angles from the subsatellite point but becomes quite nonlinear for large angles. The transfer characteristics corresponding to Eq. 6 are shown in Figs. 3, 4.

The net effects of these nonlinearities in mapping can be portrayed by tracing the loci of constant $\alpha$ and the loci of constant $\beta$ in the $(\theta,\phi)$ coordinate system. Curves of constant $\alpha$ may be obtained from Eq. 2 and curves of

constant β may be obtained from Eq. 3. The resulting loci are shown in Fig. 5. Geometrical distortions in this uncorrected mapping procedure are small for angular differences less than about 30° from the subsatellite point but become appreciable for larger angular differences. Because the relative values of α, β are generally known, a computer algorithm can be employed to remove these distortions on a point-by-point basis as the data is received serially. There are limitations to this procedure, however, and we shall examine these in a later section.

Another set of equations can be derived geometrically for the transformation of measurements in the (α,β) frame of reference to the (θ,ϕ) frame of reference. However, it is easier to make use of reciprocity and it turns out that the desired relations can be written down by observing the following interchanges:

$$\left\{\begin{matrix}\alpha \leftrightarrow \phi \\ \beta \leftrightarrow \theta \\ r \leftrightarrow R_1\end{matrix}\right\} \tag{7}$$

Thus the corresponding set of relations from the satellite coordinates to the earth coordinates is, using Eqs. 2, 3:*

$$\sin\phi = \frac{R_1 \sin\alpha}{\sqrt{R^2 + R_1^2 - 2RR_1 \cos\alpha \cos\beta}} = \frac{\gamma \sin\alpha}{\varepsilon} \tag{8}$$

where

$$\gamma = R_1/R \tag{9}$$

and

$$\tan\theta = \frac{R_1 \cos\alpha \sin\beta}{R - R_1 \cos\alpha \cos\beta} = \frac{\gamma \cos\alpha \sin\beta}{1 - \gamma \cos\alpha \cos\beta} \tag{10}$$

A typical satellite scanner consists of an optical system to image the instantaneous field of view (IFOV) and step the azimuth scan in fixed increments of α and followed by a detector of visible or infrared radiation. The

---

* This seemingly very simple expression may be deceptive; recall that γ is a function of α, β.

output of the detector is an electrical signal whose amplitude is proportional to the incident radiance from within the IFOV. After band-limiting with an electrical filter, this signal is sampled, digitized and multiplexed with other signals before transmission of the data to a ground terminal.

As the satellite rotates about its spin axis with fixed angular rate, an item of interest is the phase velocity scaling between a point source on the earth's surface and the resulting frequency content in the satellite scanner electrical signal. For convenience, we normalize this to the subsatellite point. The relative phase velocity factor $\Gamma$ at any point on the surface of the hemisphere in terms of $\alpha$, $\beta$ is [3]:

$$\Gamma = \frac{\gamma\sqrt{\varepsilon^2 - \sin^2\alpha}}{(1-\varepsilon)\sqrt{\varepsilon^2 - \sin^2\alpha - \cos^2\alpha \sin^2\beta}} \tag{11}$$

Using Eqs. 2, 3, we can reference this to the earth coordinate system and the corresponding result is shown in Fig. 6.

If the scanning aperture of the satellite were infinitesimally narrow, Fig. 6 exhibits the variation of the conversion from spatial frequency content on the earth's surface to electrical frequency as a function of position. Designating spatial frequency content by $f_o$ the resulting scanner signal frequency $f_s$ is then:

$$f_s = (1-\varepsilon)\dot{\beta}R\Gamma f_o \tag{12}$$

For a satellite spin rate of 100 rpm and $f_o$ measured in cycles per n·mi, Eq. 12 becomes:

$$f_s = 0.202\times10^6\ \Gamma f_o \tag{13}$$

Typical values for $f_o$ are on the order of one or two cycles per n.mi. This result indicates that high frequency response is necessary to reconstruct imagery accurately at angular separations more than about 30° away from the subsatellite point as a result of the rapid increase of $\Gamma$. This mode of operation is referred to as the bandwidth-limited case.

The preceding analysis assumed an infinitesimally narrow scanning aperture. In practice, the limits on scanner spatial resolution are determined more by the scanning aperture than the electrical bandwidth. In the aperture-limited case, the increase in scanning phase velocity is offset by an increase in the projected scanning aperture. Thus the spatial frequency response of the scanner is constant with angle and Fig. 6 may be interpreted as the increase of minimum detectable size with position. Early geostationary satellite scanners (e.g., ATS-I) were aperture-limited and used electrical bandwidths wider than the maximum aperture response. Recent trends (e.g., SMS-I) have been to match the electrical bandwidth to the aperture response. Geometrical distortions, in contrast to minimum spatial resolution, are also present but may be removed using a computational algorithm to remedy the distorted data format illustrated in Fig. 5.

Another item of interest is the required antenna pointing angle from the earth to the satellite. Following Smith [2] we define an azimuth angle A such that A is zero when the antenna is directed towards the north when in the southern hemisphere and directed towards the south in the northern hemisphere. The elevation angle to a geostationary satellite above the horizon is e, as seen from the earth site. The angles $\theta$, $\phi$ are the longitude and latitude relative to the subsatellite point. The values of A and e can be computed from:

$$\tan A = \frac{\tan\theta}{\sin\phi} \tag{14}$$

$$\tan e = \frac{\cos\theta \cos\phi - \varepsilon}{\sqrt{1 - \cos^2\theta \cos^2\phi}} \tag{15}$$

Loci of constant A and of constant e can then be computed from:

$$\phi = \sin^{-1}\left[\frac{\tan\theta}{\tan A}\right] \tag{16}$$

and the geometrical equivalent to Eq. 15 [2]:

$$\phi = \cos^{-1}\left[\frac{\sin[e + \sin^{-1}(\varepsilon \cos e)]}{\cos\theta}\right] \tag{17}$$

A plot of the loci of constant A and constant e, as given by Smith [2], is shown in Fig. 7. This plot is important to us here because it portrays the angle of perspective (e) for mapping imagery on the surface of the earth. Use of Eqs. 2, 3 also permits us to refer the angles to the satellite coordinate frame of reference, as shown in Fig. 8. Note that although the loci of constant A and constant e are quite orthogonal for mappings near the subsatellite point, there is an appreciable amount of cross-coupling effects for elevation angles less than $e \approx 30°$.

## III. MEASUREMENT ACCURACY

The position of a ground site may be measured either in the earth or satellite coordinate system. For a given measurement in one of the two reference systems, the other set of coordinates may be obtained by using the geometrical conversion developed in the previous section. Naturally, disturbances exist either in the environment or in the satellite system itself. Some of these disturbance sources and effects are slowly-varying and can be detected (e.g., navigational and orbital variations) and corrected with appropriate computer instructions. Others, however, can best be handled as random disturbances or inaccuracies in the satellite frame of reference (e.g., non-ideal optical response, bandwidth limitations, etc.). These effects limit the attainable mapping resolution even though the required geometrical corrections are made. Here we shall look at some of these problems using probabilistic methods.

We assume that the longitude $\theta$ and latitude $\phi$ within a specified region on the earth's surface are represented by the independent random variables $X_\theta$, $X_\phi$, respectively. The positions in the satellite coordinate system $\alpha$, $\beta$ are random variables because they are functions of $X_\theta$, $X_\phi$. For notational simplicity we use $\theta$, $\phi$ for $X_\theta$, $X_\phi$ whenever it is not confusing.

Within the line-of-sight restriction of Eq. 5, the satellite angles $(\alpha,\beta)$ are single-valued functions of the earth coordinates $(\theta,\phi)$. Using the

well-known rule for the transformation of random variables [4], the joint density function of $\alpha$, $\beta$ can be expressed in terms of the joint density function of $\theta$, $\phi$ as:

$$p_{\alpha,\beta}(\alpha,\beta) = \frac{1}{|J(\theta,\phi)|}\, p_{\theta,\phi}(\theta,\phi) \tag{18}$$

where J is the Jacobian of the transformation as given by:

$$J(\theta,\phi) = \begin{vmatrix} \frac{\partial\alpha}{\partial\theta} & \frac{\partial\alpha}{\partial\phi} \\ \frac{\partial\beta}{\partial\theta} & \frac{\partial\beta}{\partial\phi} \end{vmatrix} \tag{19}$$

and Eqs. 8, 10 can be used to substitute for $\theta$, $\phi$ in the right-hand side of Eq. 18.

While this presents a formal solution, it is complicated and not very convenient for the problem at hand. Because a computation only of the first two moments will suffice, we instead resort to an approximation of the first two moments. Let $g\{\ \}$ represent a single-valued function; then the first moments of $\theta$, $\phi$ are (where $E\{\ \}$ denotes the expectation operator):

$$\begin{aligned} \eta_\theta &= E_\theta\{g(\theta,\phi)\} \\ \eta_\phi &= E_\phi\{g(\theta,\phi)\} \end{aligned} \tag{20}$$

If $p(\theta,\phi)$ is centered near $\eta_\theta$, $\eta_\phi$, and $g(\theta,\phi)$ is "smooth" in the vicinity of this point*, we can write [4]:

$$E\{g(\theta,\phi)\} \cong g(\eta_\theta,\eta_\phi) + \frac{1}{2}\left(\mu_{20}\frac{\partial^2 g}{\partial\theta^2} + 2\mu_{11}\frac{\partial^2 g}{\partial\theta\,\partial\phi} + \mu_{02}\frac{\partial^2 g}{\partial\phi^2}\right) \tag{21}$$

where the joint central moments $\mu_{kr}$ are defined by:

$$\mu_{kr} = E\{(X_\theta-\eta_\theta)^k\,(X_\phi-\eta_\phi)^r\} \tag{22}$$

In a similar manner, an approximation to the variance is:

$$\sigma^2_{g(\theta,\phi)} = \left(\frac{\partial g}{\partial\theta}\right)^2\mu_{20} + \left(\frac{\partial g}{\partial\phi}\right)^2\mu_{02} + 2\,\frac{\partial g}{\partial\theta}\,\frac{\partial g}{\partial\phi}\,\mu_{11} \tag{23}$$

---

* Typical aperture responses — both optical and electrical — tend to easily satisfy these criteria.

We have:

$$\mu_{20} = \sigma_\theta^2 , \qquad \mu_{02} = \sigma_\phi^2 ,$$

and because $X_\theta$ and $X_\phi$ are independent, it follows that:

$$\mu_{11}' = 0$$

For convenience in handling the problem beyond this point we make the assumption that the variances in $\theta$, $\phi$ are equal:

$$\sigma_\theta^2 = \sigma_\phi^2 = \sigma^2 \tag{24}$$

Checking the assumptions made here by using a two-dimensional Gaussian joint density function for $\theta$, $\phi$ using the extremely large value of $\sigma$ = 10 milliradians (about 80 n·mi at the earth's surface) reveals that the approximate evaluation of the first and second moments can be applied in this problem even to this extent within an accuracy of ±0.3%.

## 3.1 Analysis of the Scan Tilt Angle, $\alpha$

If we expand $\alpha(\theta,\phi)$ in a series about $\eta_\theta$, $\eta_\phi$, we find that $\alpha$ can be considered a linear function of $\theta$, $\phi$ in a range of ±7° around $\eta_\theta$, $\eta_\phi$, and within an error of less than one percent. Thus we can write:

$$\alpha(\theta,\phi) \cong \alpha(\eta_\theta,\eta_\phi) + \frac{\partial\alpha}{\partial\theta}(\theta-\eta_\theta) + \frac{\partial\alpha}{\partial\phi}(\phi-\eta_\phi) \tag{25}$$

where

$$\frac{\partial\alpha}{\partial\theta} = \frac{-\varepsilon^2 \sin\theta \sin\phi \cos\phi}{\gamma^2(\gamma^2-\varepsilon^2 \sin^2\phi)^{\frac{1}{2}}} \tag{26}$$

$$\frac{\partial\alpha}{\partial\phi} = \frac{\varepsilon(\gamma^2 \cos\phi - \varepsilon \sin^2\phi \cos\theta)}{\gamma^2(\gamma^2-\varepsilon^2 \sin^2\phi)^{\frac{1}{2}}} \tag{27}$$

For small angular displacements on the order of tens of milliradians $\alpha(\theta,\phi)$ may be considered as a smooth, slowly-varying function and we can use Eqs. 26, 27 in Eq. 23 to give:

$$\sigma_\alpha^2 \cong \frac{\sigma^2\varepsilon^2[(\gamma^2 \cos\phi - \varepsilon \sin^2\phi \cos\theta)^2 + (\varepsilon \sin\theta \cos\phi \sin\phi)^2]}{\gamma^4(\gamma^2 - \varepsilon^2 \sin^2\phi)} \tag{28}$$

where $\gamma$ is the normalized distance between the satellite point and the specified position and is given by Eqs. 1, 9, or the alternate form:

$$\gamma^2 = 1 + \varepsilon^2 - 2\varepsilon \cos\theta \cos\phi \tag{29}$$

The ratio $\sigma_\alpha/\sigma$ is the decrease in mapping source spread on the earth's surface as observed and measured in the satellite coordinate system. It is convenient to normalize this ratio by referring it to the earth coordinate system: $(\gamma/\varepsilon)\sigma_\alpha/\sigma$ so that it is unity at the subsatellite point. A normalized graph is shown in Fig. 9. Note that the plots have been truncated at earth tangency points (cf. Eq. 5).

We shall define the bias in the mean as:

$$\Delta\alpha(\theta,\phi) = E\{\alpha(X_\theta, X_\phi)\} - \alpha(\theta,\phi) \tag{30}$$

Evaluating the second partial derivatives of $\alpha(\theta,\phi)$ and using Eq. 21, we have:

$$\begin{aligned}\Delta\alpha(\theta,\phi) = -\frac{\sigma^2\varepsilon\sin\phi[(\gamma^2 - \varepsilon^2\sin^2\phi)}{2\gamma^4(\gamma^2 - \varepsilon^2\sin^2\phi)^{3/2}} \\ \left[\frac{(\gamma + 3\varepsilon\gamma^2\cos\theta\cos\phi - 2\varepsilon^2\cos^2\theta\sin^2\phi)}{2\gamma^4(\gamma^2 - \varepsilon^2\sin^2\phi)^{3/2}}\right. \\ + \frac{\varepsilon\gamma^2(\cos\theta - \varepsilon\cos\phi)(\gamma^2\cos\phi - \varepsilon\sin^2\phi\cos\theta)}{2\gamma^4(\gamma^2 - \varepsilon^2\sin^2\phi)^{3/2}} \\ \left. - \frac{\varepsilon^2\sin\phi\cos^2\phi\sin^2\theta(3\gamma^2 - 2\varepsilon^2\sin^2\phi)]}{2\gamma^4(\gamma^2 - \varepsilon^2\sin^2\phi)^{3/2}}\right]\end{aligned} \tag{31}$$

A graph of Eq. 31 is shown in Fig. 10. The bias is always negative, quite nonlinear in $\theta$ along lines of constant latitude and becomes quite linear for relative longitude angles greater than 30°.

## 3.2 Analysis of the Spin Scan Angle, $\beta$

A similar procedure may be followed to evaluate the moments of $\beta$. Again, if we expand $\beta$ in a series about $\eta_\theta$, $\eta_\phi$, we find that $\beta$ is smooth and slowly varying in the vicinity of $(\eta_\theta, \eta_\phi)$. The approximate evaluation of the moments applied to $\alpha$ may be applied as well to $\beta$ within almost the same accuracy. Thus we have:

$$\beta(\theta,\phi) \cong \beta(\eta_\theta,\eta_\phi) + \frac{\partial\beta}{\partial\theta}(\theta-\eta_\theta) + \frac{\partial\beta}{\partial\phi}(\phi-\eta_\phi) \tag{32}$$

where

$$\frac{\partial\beta}{\partial\theta} = \frac{\varepsilon\cos\phi(\cos\theta - \varepsilon\cos\phi)}{1 - 2\varepsilon\cos\theta\cos\phi + \varepsilon^2\cos^2\phi} \tag{33}$$

$$\frac{\partial\beta}{\partial\phi} = \frac{-\varepsilon\sin\theta\sin\phi}{1 - 2\varepsilon\cos\theta\cos\phi + \varepsilon^2\cos^2\phi} \tag{34}$$

Using these in Eq. 23, we obtain:

$$\sigma_\beta^2 \cong \frac{\sigma^2\varepsilon^2[\sin^2\theta\ \sin^2\phi + \cos^2\phi(\cos\theta - \varepsilon\ \cos\phi)^2]}{(1 - 2\varepsilon\ \cos\theta\ \cos\phi + \varepsilon^2\ \cos^2\phi)^2} \tag{35}$$

A graph of Eq. 35 is shown in Fig. 11. Again it is convenient to normalize to the earth coordinate system by introducing $\gamma$ (cf. Eq. 29). Note that, in contrast to the result for the tilt angle, the variance of $\beta$ is not monotonic. It is proportional to $\beta$ in the range 0-42° in $\theta$ and inversely proportional to $\beta$ for higher values of $\theta$. Also, it is proportional to $\beta$ in the range 0-47° in $\phi$ and inversely proportional to $\beta$ for higher values of $\phi$. This unusual behavior is the result of a twisting of the angular perspective between the two coordinate systems.

We define the bias in the mean of $\beta$ to be:

$$\Delta\beta(\theta,\phi) = E\{\beta(X_\theta, X_\phi)\} - \beta(\theta,\phi) \tag{36}$$

and use of Eq. 21 yields:

$$\Delta\beta(\theta,\phi) = -\frac{\sigma^2\varepsilon\ \sin\theta(\cos\phi - \varepsilon\ \cos\theta + \varepsilon^2\ \sin^2\phi\ \cos\phi)}{(1 - 2\varepsilon\ \cos\theta\ \cos\phi + \varepsilon^2\ \cos^2\phi)^2} \tag{37}$$

A graph of Eq. 37 is shown in Fig. 11. The bias in the mean of the spin scan angle is proportional to $\sin\beta$ and because $\beta$ varies only over small angles, the bias in $\beta$ is proportional to the value of $\beta$.

The bias in the mean, the variance, and the joint density function of $\alpha$ and $\beta$ all depend on the variance of the given density function and on position, i.e., on the coordinates $\theta$ and $\phi$ of the position, which are in turn the means of the random variables $X_\theta$ and $X_\phi$, respectively.

Basically, the same approach can be followed to solve for the transformation of random variables from the satellite to the earth coordinate system. In other words, the problem would be to find the joint density function, the bias in the means, and the variances of $\theta$ and $\phi$ for a given disturbance of a known density function with zero mean and a given variance $\sigma^2$ in $\alpha$ and $\beta$.

## IV. MAPPING RESOLUTION

The geometric transformation from the earth coordinate system to that of a spin-scan geostationary satellite was described in section 2. In many cases the mapping in $\alpha$, $\beta$ can be interpreted as a linear mapping of a scene in $\theta$, $\phi$ when the angular differences from the subsatellite point are small and the geometric distortion is tolerable. An inverse transformation can be made to remove the geometric distortion and this could be accomplished ideally were it not for the fact that errors and inaccuracies occur in the measurement. These errors may arise from short-term satellite pointing inaccuracies, optical response limitations, bandwidth restrictions, etc. We assume that these inaccuracies can be described in terms of second moments about the true pointing angle. The standard deviation of these inaccuracies is a measure of the mapping resolution in the $(\alpha,\beta)$ coordinate system.

In the previous section we used an approximation for the variation of $\sigma_\alpha$ and $\sigma_\beta$ for a circular source ( of radius $\sigma$ ) positioned at $\theta$, $\phi$ on the earth's surface. As observed, however, there is a twisting or rotational effect between the two coordinate systems for large values of $\theta$, $\phi$. Therefore we define a tangential measured source spread function $\sigma_t$ as:

$$\sigma_t = \sqrt{(\sigma_\alpha^2+\sigma_\beta^2)/2} \quad . \tag{36}$$

A second measure of source spread function is taken along the great circle which includes the line from the satellite and the observed point. This measure $\sigma_n$ is found by the projection of the circular source $\sigma$ through the angle e defined in section 2. Using Eq. 15 we can write:

$$\sigma_n = \sigma \sin\left[\tan^{-1}\left(\frac{\cos\theta\,\cos\phi - \varepsilon}{\sqrt{1-\cos^2\theta\,\cos^2\phi}}\right)\right] \quad . \tag{37}$$

Equation 37 arises as a direct result of the oblique angle of observation in the measurement.

We also define an rms satellite measurement inaccuracy about the true pointing angle by $\sigma_s$. It is convenient to normalize $\sigma_s$ by referring it to $\sigma$ at the subsatellite point. Therefore we define $\sigma_s$ in terms of a parameter k such that:

$$\sigma_s = k\sigma[\varepsilon/(1-\varepsilon)] \tag{38}$$

where k is the ratio of the rms satellite measurement inaccuracies to the source spread $\sigma$. Both are measured at the subsatellite point and the factor $[\varepsilon/(1-\varepsilon)]$ in Eq. 38 refers $\sigma_s$ to the earth coordinate system scaling.

The mapping procedure assumes a circular source at $\theta$, $\phi$ of spread $\sigma$ which is measured in $\alpha$, $\beta$. The measured source spread is $\sigma_\alpha$, $\sigma_\beta$ and inaccuracies in the satellite measurement have a spread $\sigma_s$. The inverse transformation can now be performed to yield the desired reconstruction. Note that the transformation from $(\theta,\phi)$ to $(\alpha,\beta)$ varies with angle but $\sigma_s$ is assumed to be constant and is not dependent on $\alpha$, $\beta$.

As a measure of how well the inverse transformation can be accomplished in a mean-square sense, we define a tangential mapping resolution factor as:

$$\rho_t = \sqrt{1+k^2}\,\frac{\sigma_t}{\sqrt{\sigma_t^2+\sigma_s^2}} \tag{39}$$

where the factor $\sqrt{1+k^2}$ is used to normalize $\rho_t$ to unity at the subsatellite point. In a similar manner, we define a normal mapping resolution factor as:

$$\rho_n = \sqrt{1+k^2}\,\frac{\sigma_n}{\sqrt{\sigma_n^2+\sigma_s^2}} \quad . \tag{40}$$

These two mapping resolution factors have been chosen in such a way that they are always perpendicular and are normalized to unity at the subsatellite point. It can also be shown that $\rho_t \geq \rho_n$.

A plot of the loci of Eqs. 39, 40 is shown in Fig. 13 for the case of $k^2 = 1$ (i.e., mean-square satellite measurement inaccuracies equal to mean-square mapping source size). A second plot for the case of $k^2 = 0.10$ is shown

in Fig. 14. Using a criterion of 0.9 for the mapping resolution factor, we conclude that the rms spread function of the satellite measurement inaccuracies must be on the order of $\sqrt{10}$ less than the minimum IFOV resolution size for acceptable reconstruction out to about 50° from the subsatellite point. A plot of maximum angle from the subsatellite point for acceptable reconstruction within given values of normalized resolution factor is shown in Fig. 15. Figs. 13, 14 can also be used to determine asymmetry in the residual distortion introduced in the mapping.

## V. CONCLUSIONS

Mapping from a spherical earth to a spin-scan geostationary satellite is single-valued but not linear except for small angles. Variation in scanning velocity results in variation of measured frequency content and the system may be limited by electrical bandwidth unless it is aperture-limited. Transformations were developed and could be used to remove effects of geometrical distortion on a point-by-point basis.

The capability of making corrections for geometrical distortions is limited by the inaccuracies of the instrument in the satellite. Two measures of mapping resolution $\rho_t$, $\rho_n$ were introduced which were not sensitive to rotational effects between coordinate systems. Based on a mean-square criterion, satellite measurement inaccuracies on the order of $1/\sqrt{10}$ times the minimum IFOV resolution size are required for good image reconstruction out to about 50° from the subsatellite point.

REFERENCES

1. Schouten, S. K., "Calculations Available from Consol I," Internal Document, Space Science and Engineering Center, University of Wisconsin, Madison, Wisconsin, 1966.

2. Smith, F. L., III, "A Nomogram for Look Angles to Geostationary Satellites," IEEE Trans. Aerosp. Elec. Syst., AES-8, 394, May 1972.

3. Khalil, M. A., "Ground Mapping Accuracy of a Geostationary Satellite," M.S. Thesis in Electrical and Computer Engineering, University of Wisconsin, Madison, Wisconsin, August 1973.

4. Papoulis, A., Probability, Random Variables, and Stochastic Processes, McGraw-Hill, New York, 1965, Ch. 7.

FIGURE CAPTIONS

Figure 1 Satellite Coordinate Frame of Reference

Figure 2 Earth-Satellite Geometry

Figure 3 Characteristic Transfer Curve of the Spin-Scan Angle

Figure 4 Characteristic Transfer Curve of the Scan-Tilt Angle

Figure 5 Mapping from Earth Coordinates to Satellite Coordinates

Figure 6 Normalized Scanning Phase Velocity

Figure 7 Mapping from Earth Antenna Coordinates to Geostationary Satellite in the Earth Coordinate System [2]

Figure 8 Mapping from Earth Antenna Coordinates to Geostationary Satellite in the Satellite Coordinate System

Figure 9 Variance of the Scan Tilt Angle Measured in the Earth Coordinate System

Figure 10 Bias in the Mean of the Scan Tilt Angle

Figure 11 Variance of the Spin Scan Angle Measured in the Earth Coordinate System

Figure 12 Bias in the Mean of the Spin Scan Angle

Figure 13 Loci of Fixed Resolution Normalized to the Subsatellite Point; $\sigma_s = \sigma$

Figure 14 Loci of Fixed Resolution Normalized to the Subsatellite Point; $\sigma_s = \sigma/\sqrt{10}$

Figure 15 Maximum Allowable Angle from Subsatellite Point for Acceptable Image Reconstruction

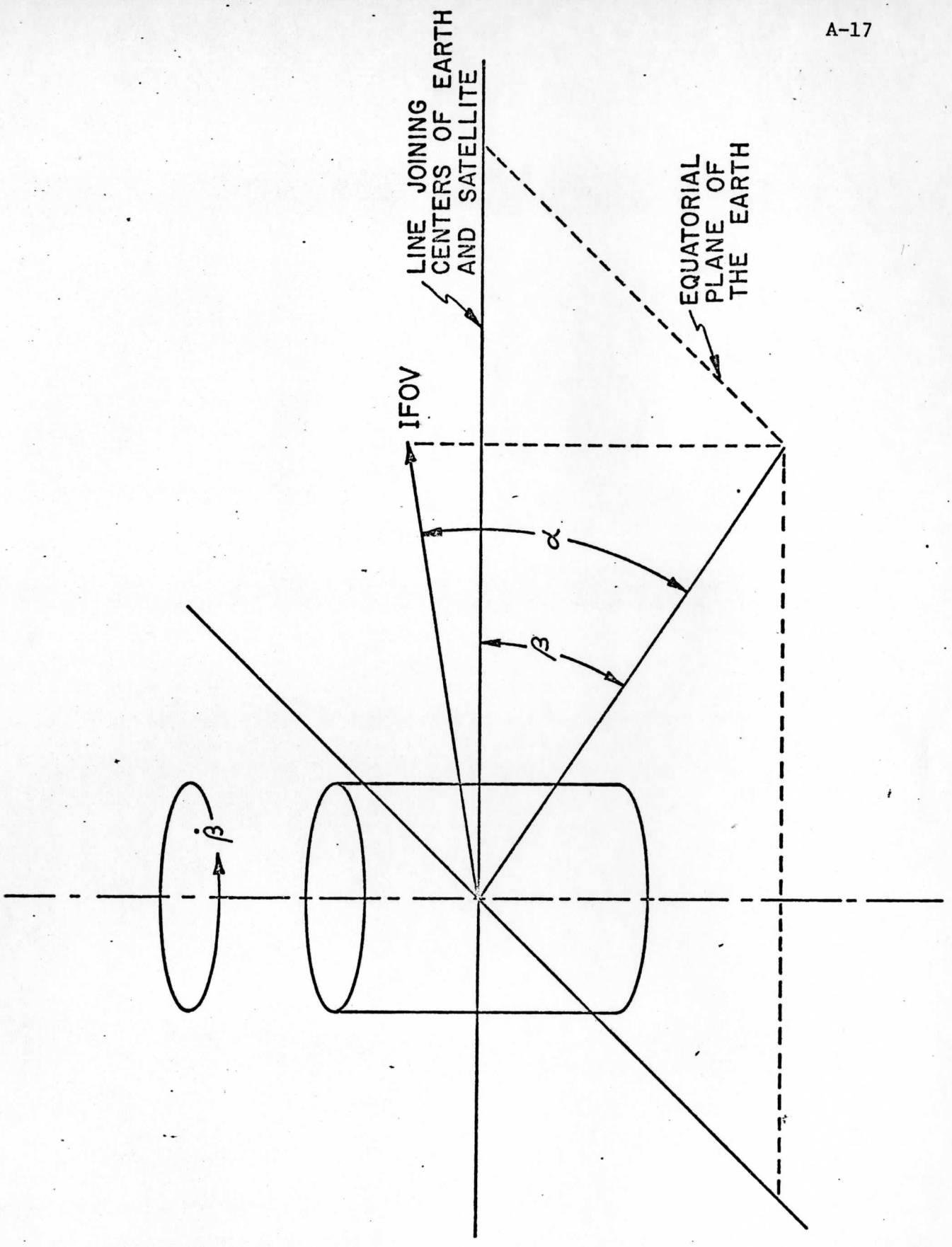
LINE JOINING CENTERS OF EARTH AND SATELLITE
EQUATORIAL PLANE OF THE EARTH
IFOV
α
β
β̇

Fig. 1

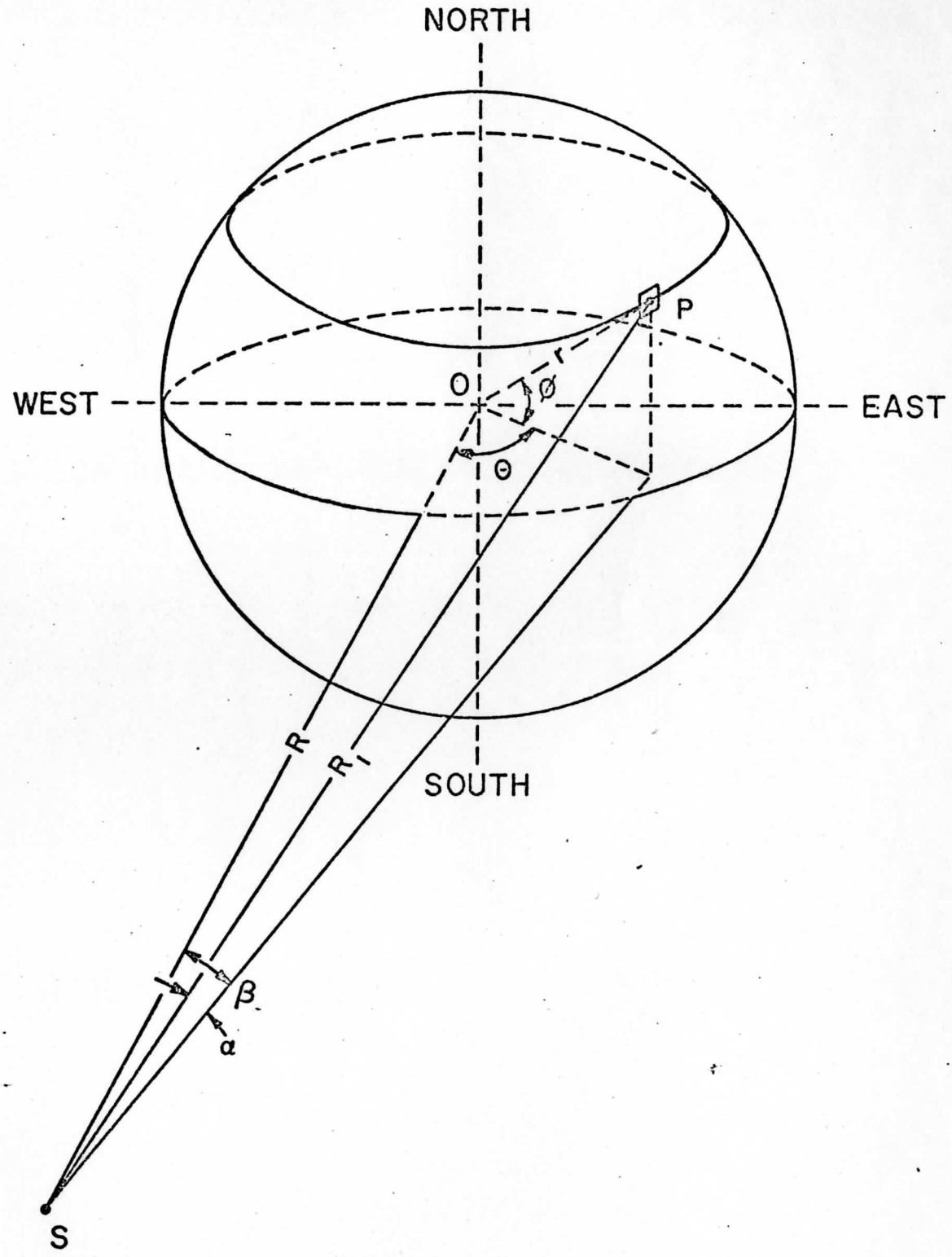


Fig. 2

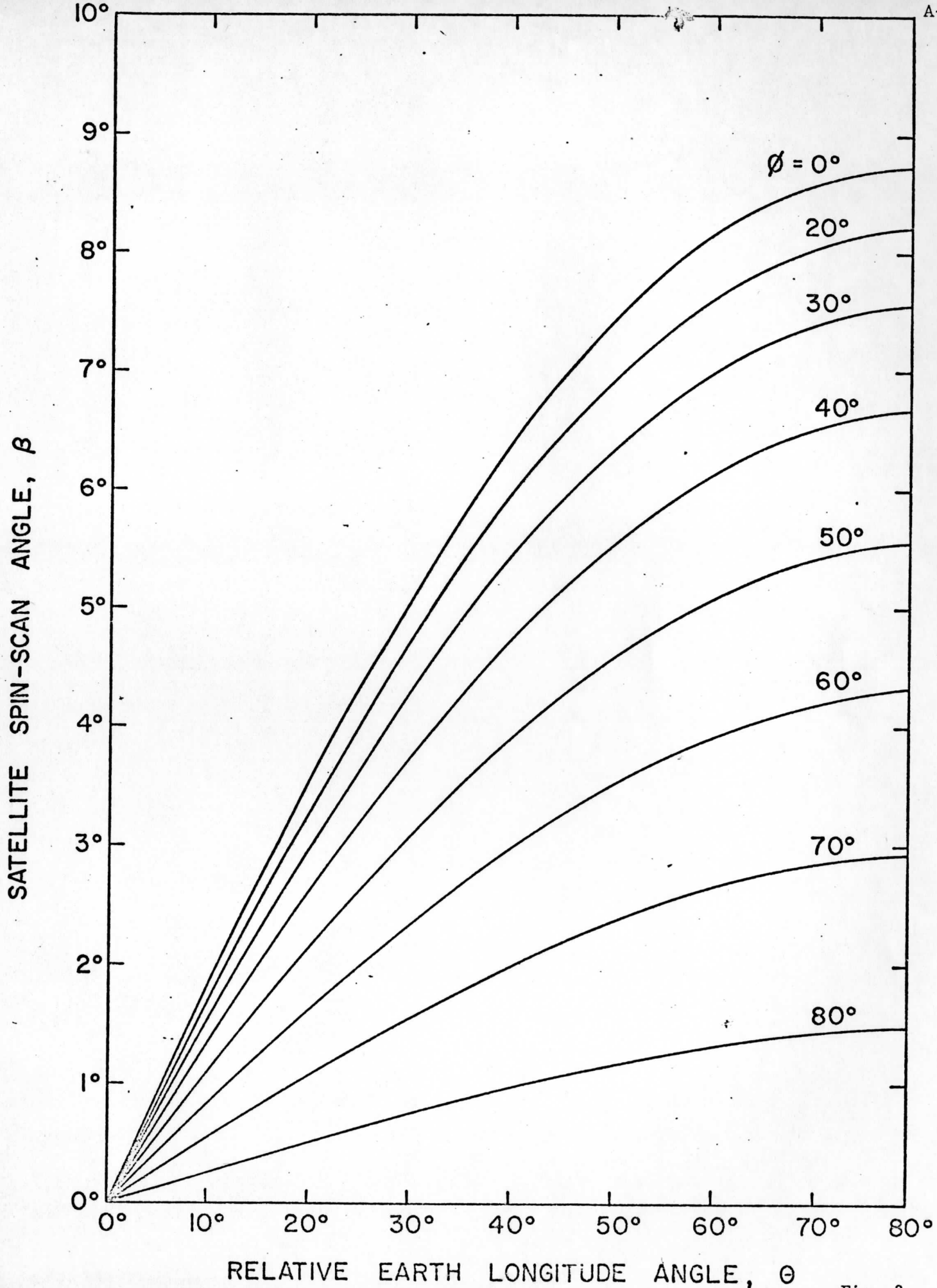
10°
9°
8°
7°
6°
5°
4°
3°
2°
1°
0°
SATELLITE SPIN-SCAN ANGLE, β
Ø = 0°
20°
30°
40°
50°
60°
70°
80°
0°
10°
20°
30°
40°
50°
60°
70°
80°
RELATIVE EARTH LONGITUDE ANGLE, Θ

Fig. 3

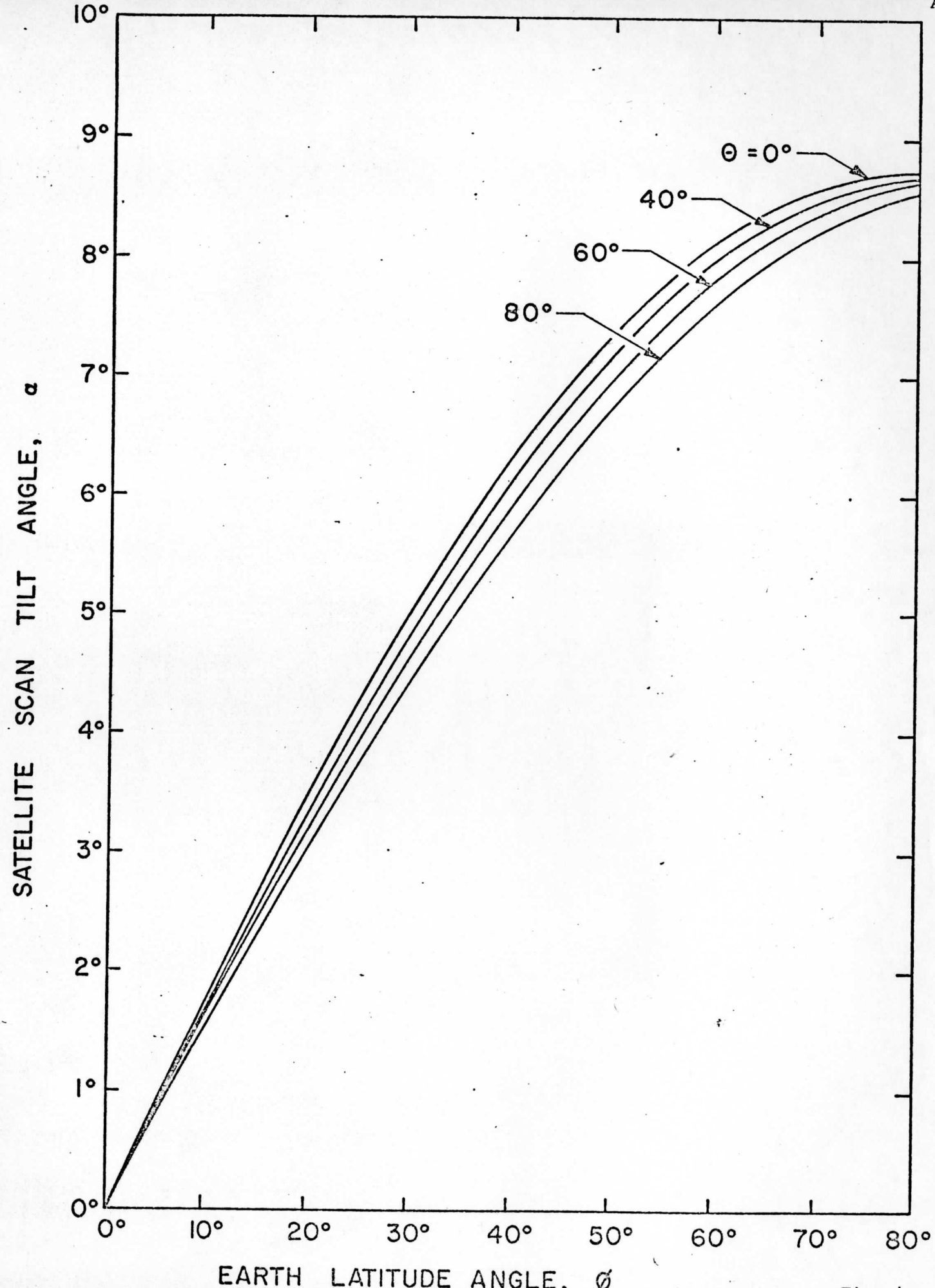
10°
9°
8°
7°
6°
5°
4°
3°
2°
1°
0°
SATELLITE SCAN TILT ANGLE, α
Θ = 0°
40°
60°
80°
0°
10°
20°
30°
40°
50°
60°
70°
80°
EARTH LATITUDE ANGLE, Ø

Fig. 4

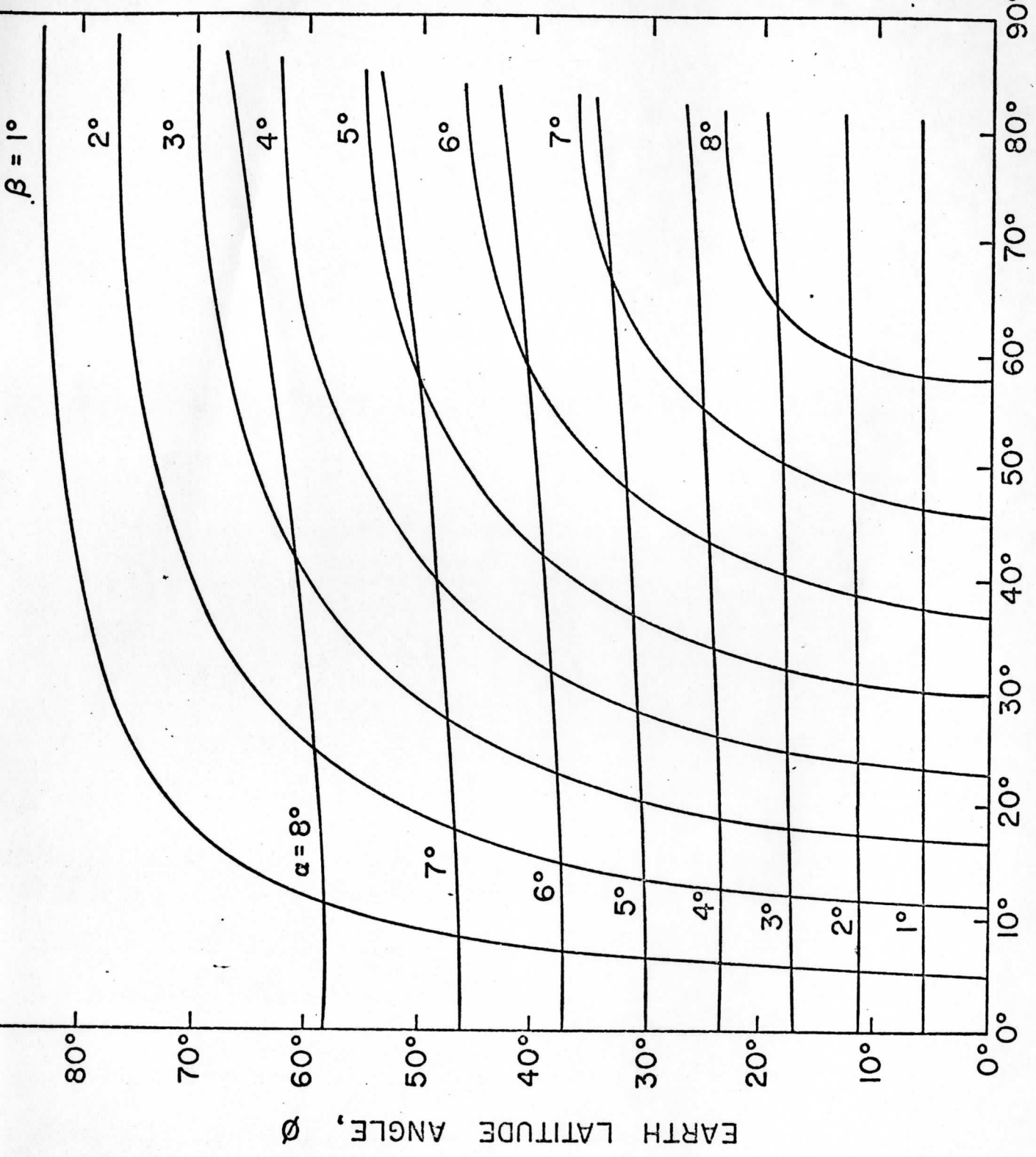
β = 1°
2°
3°
4°
5°
6°
7°
8°
α = 8°
7°
6°
5°
4°
3°
2°
1°
0°
10°
20°
30°
40°
50°
60°
70°
80°
90°
RELATIVE EARTH LONGITUDE ANGLE, Θ
EARTH LATITUDE ANGLE, Ø

Fig. 5

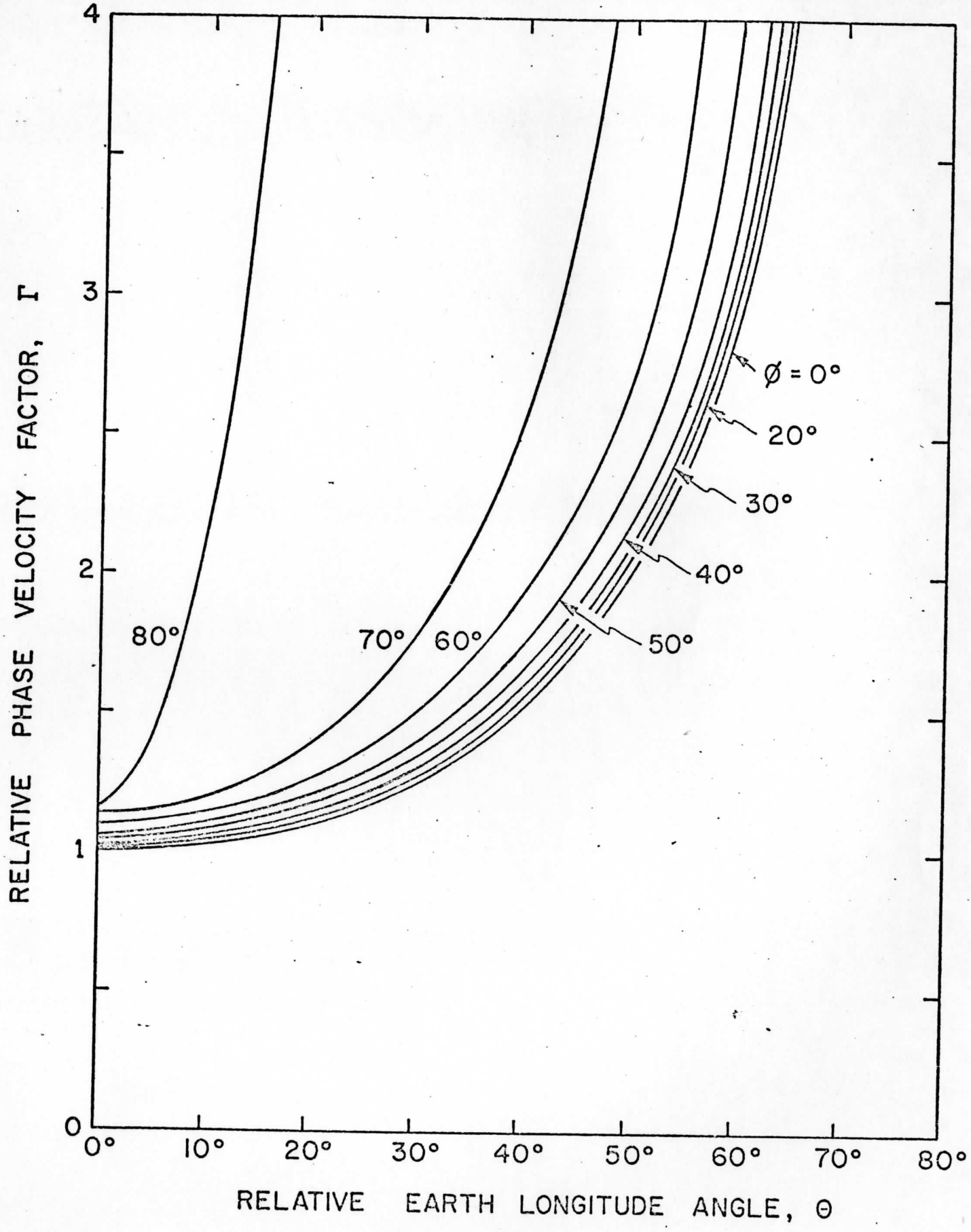
RELATIVE PHASE VELOCITY FACTOR, Γ
4
3
2
1
0
80°
70°
60°
50°
40°
30°
20°
Ø = 0°
0°
10°
20°
30°
40°
50°
60°
70°
80°
RELATIVE EARTH LONGITUDE ANGLE, Θ

Fig. 6

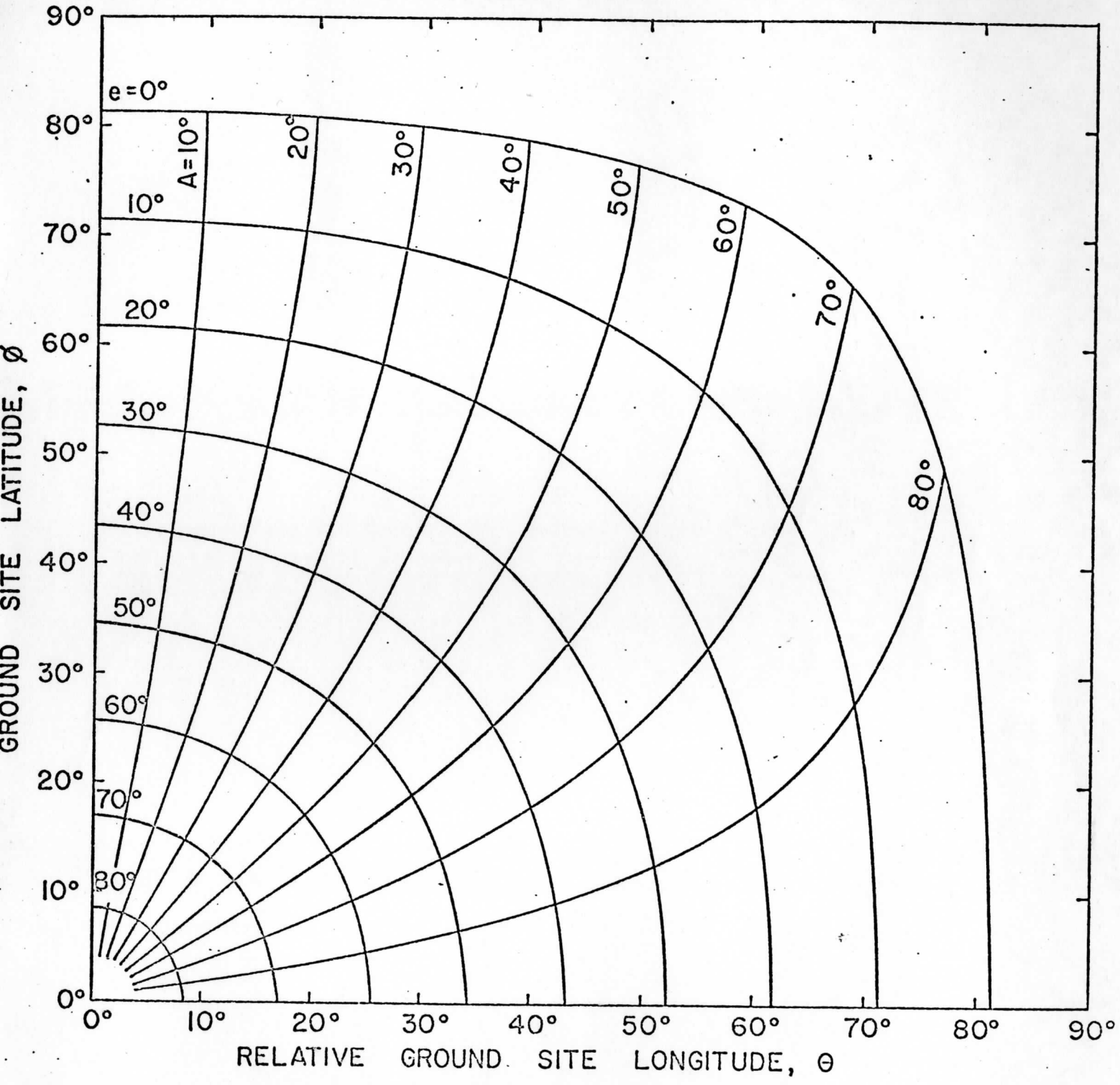
e=0°
A=10°
10°
20°
30°
40°
50°
60°
70°
80°
90°
GROUND SITE LATITUDE, ϕ
RELATIVE GROUND SITE LONGITUDE, Θ

Fig. 7

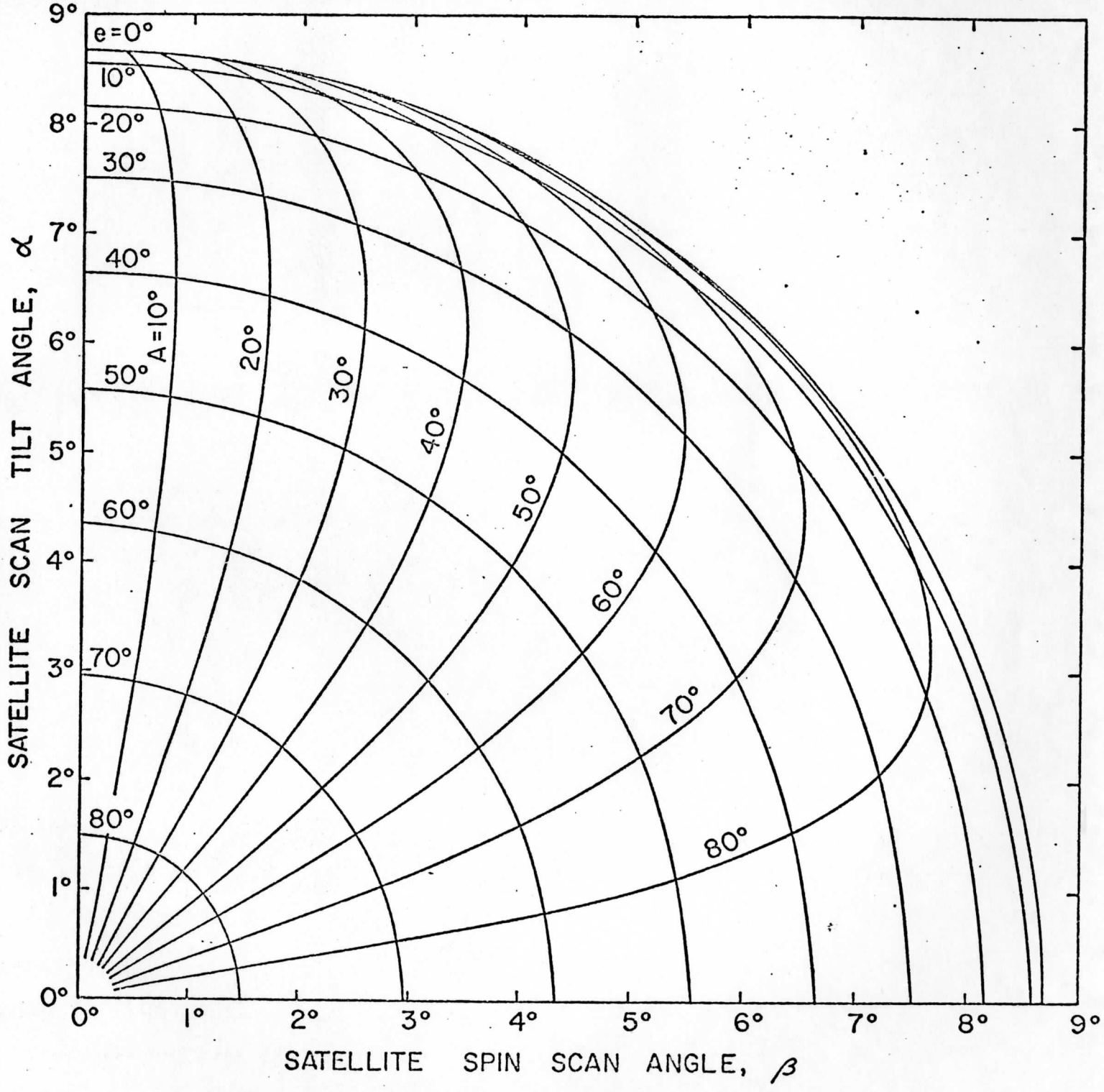
e=0°
10°
20°
30°
40°
50°
60°
70°
80°
A=10°
20°
30°
40°
50°
60°
70°
80°
0°
1°
2°
3°
4°
5°
6°
7°
8°
9°
SATELLITE SCAN TILT ANGLE, α
SATELLITE SPIN SCAN ANGLE, β

Fig. 8

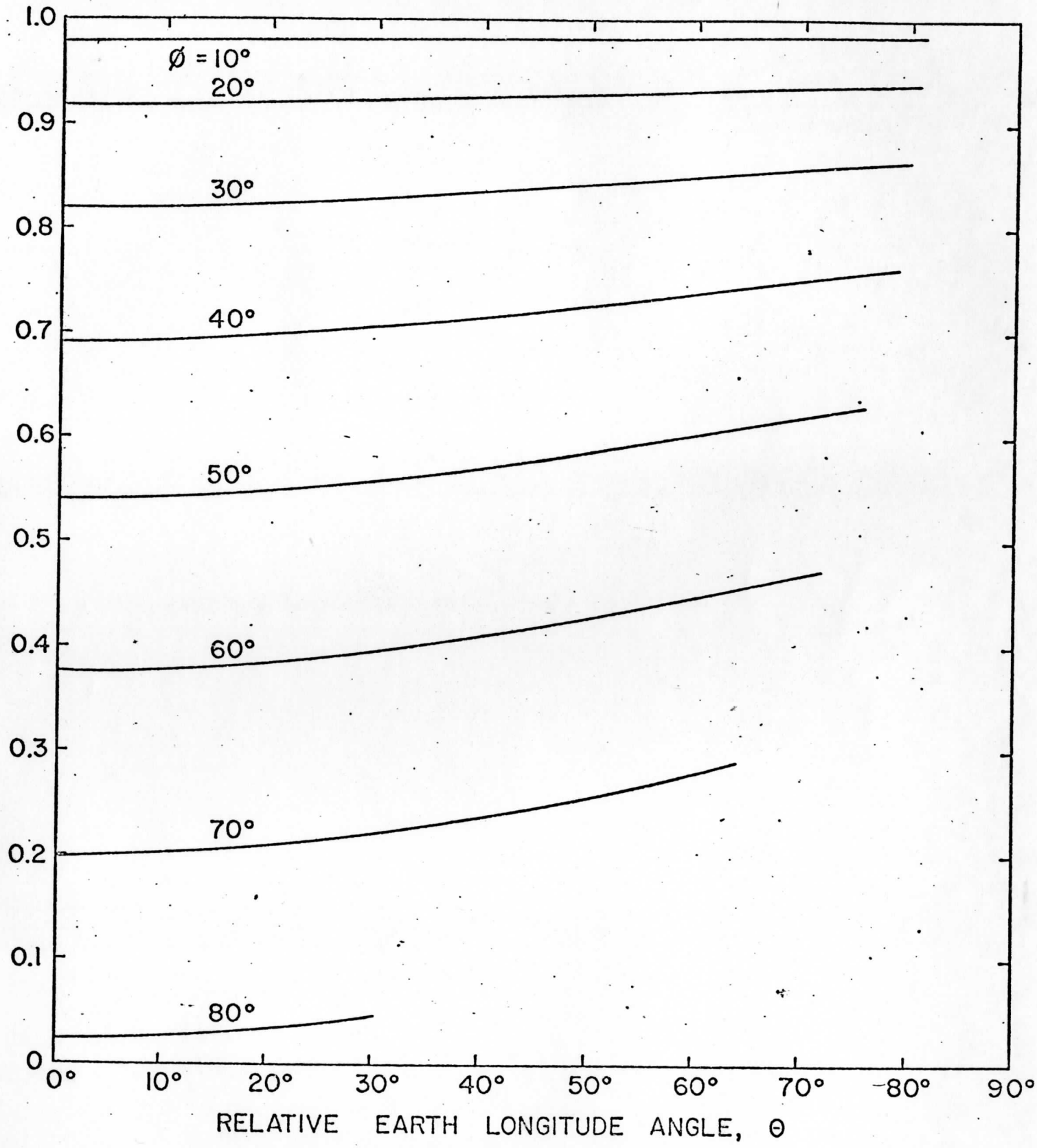
1.0
0.9
0.8
0.7
0.6
0.5
0.4
0.3
0.2
0.1
0
Ø = 10°
20°
30°
40°
50°
60°
70°
80°
0°
10°
20°
30°
40°
50°
60°
70°
80°
90°
RELATIVE EARTH LONGITUDE ANGLE, Θ

Fig. 9

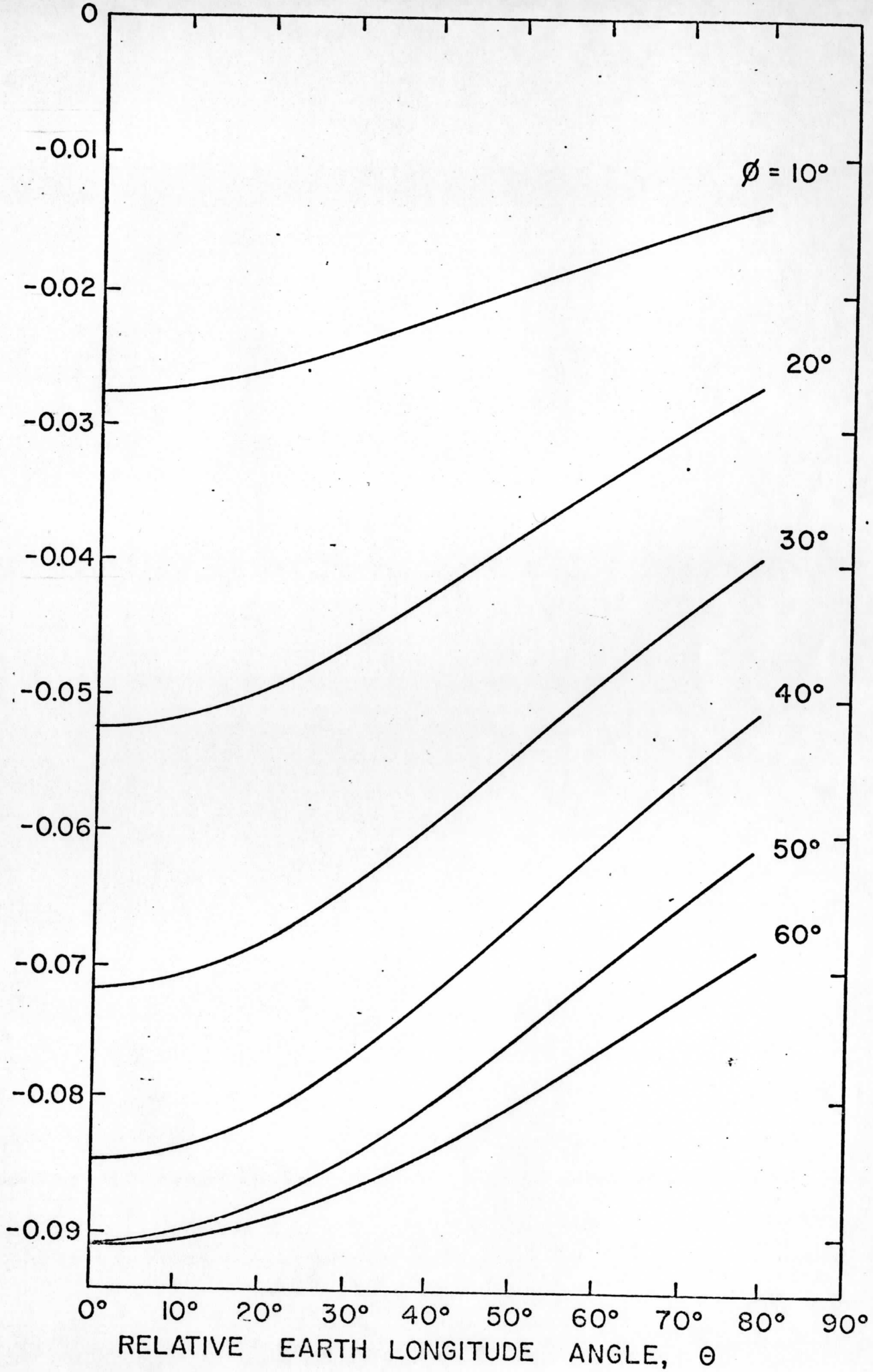
0
-0.01
-0.02
-0.03
-0.04
-0.05
-0.06
-0.07
-0.08
-0.09
Δα/σ² IN DEGREES⁻¹
Ø = 10°
20°
30°
40°
50°
60°
0° 10° 20° 30° 40° 50° 60° 70° 80° 90°
RELATIVE EARTH LONGITUDE ANGLE, Θ

Fig. 10

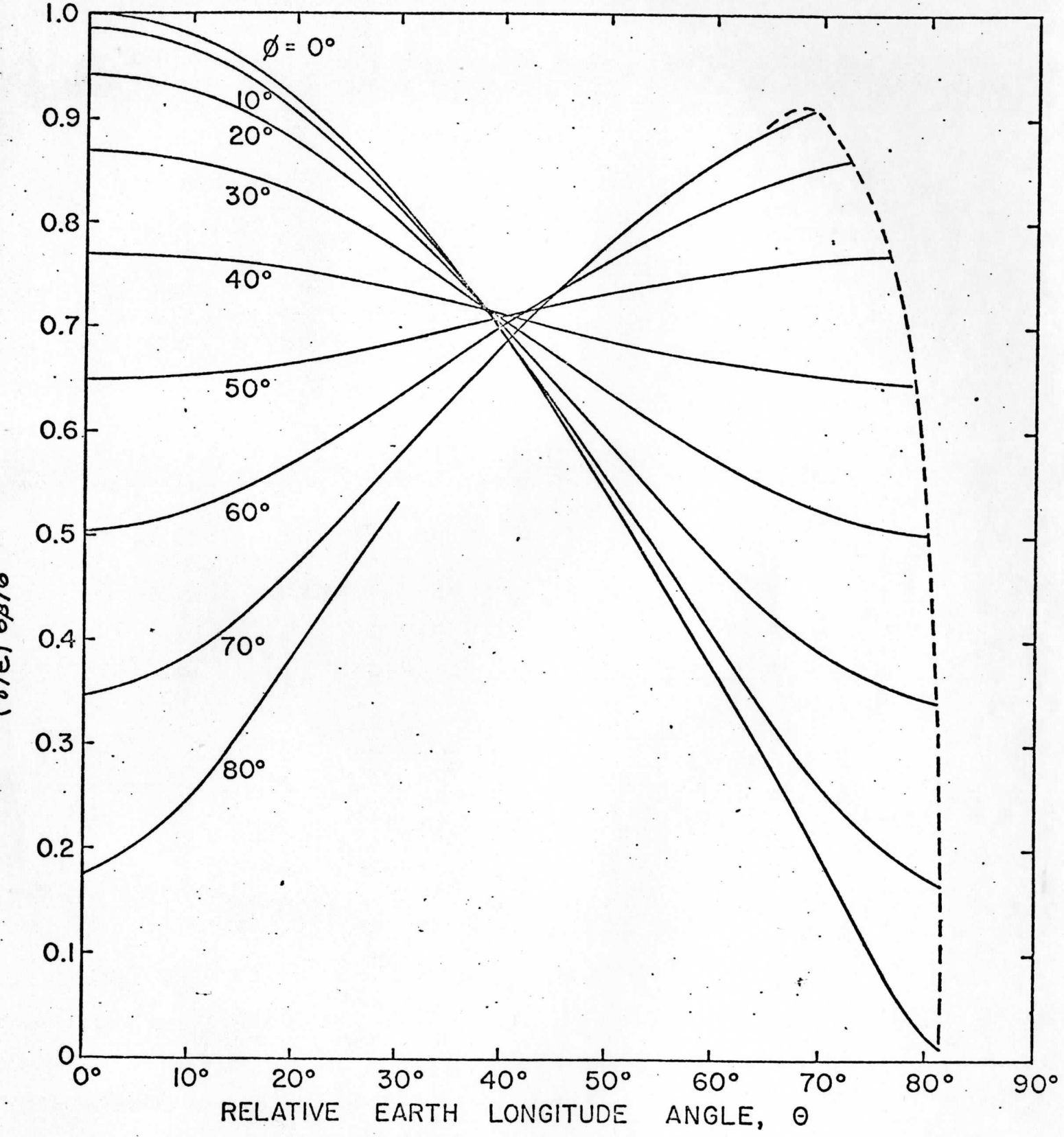
1.0
0.9
0.8
0.7
0.6
0.5
0.4
0.3
0.2
0.1
0
Ø = 0°
10°
20°
30°
40°
50°
60°
70°
80°
0°
10°
20°
30°
40°
50°
60°
70°
80°
90°
RELATIVE EARTH LONGITUDE ANGLE, Θ

Fig. 11

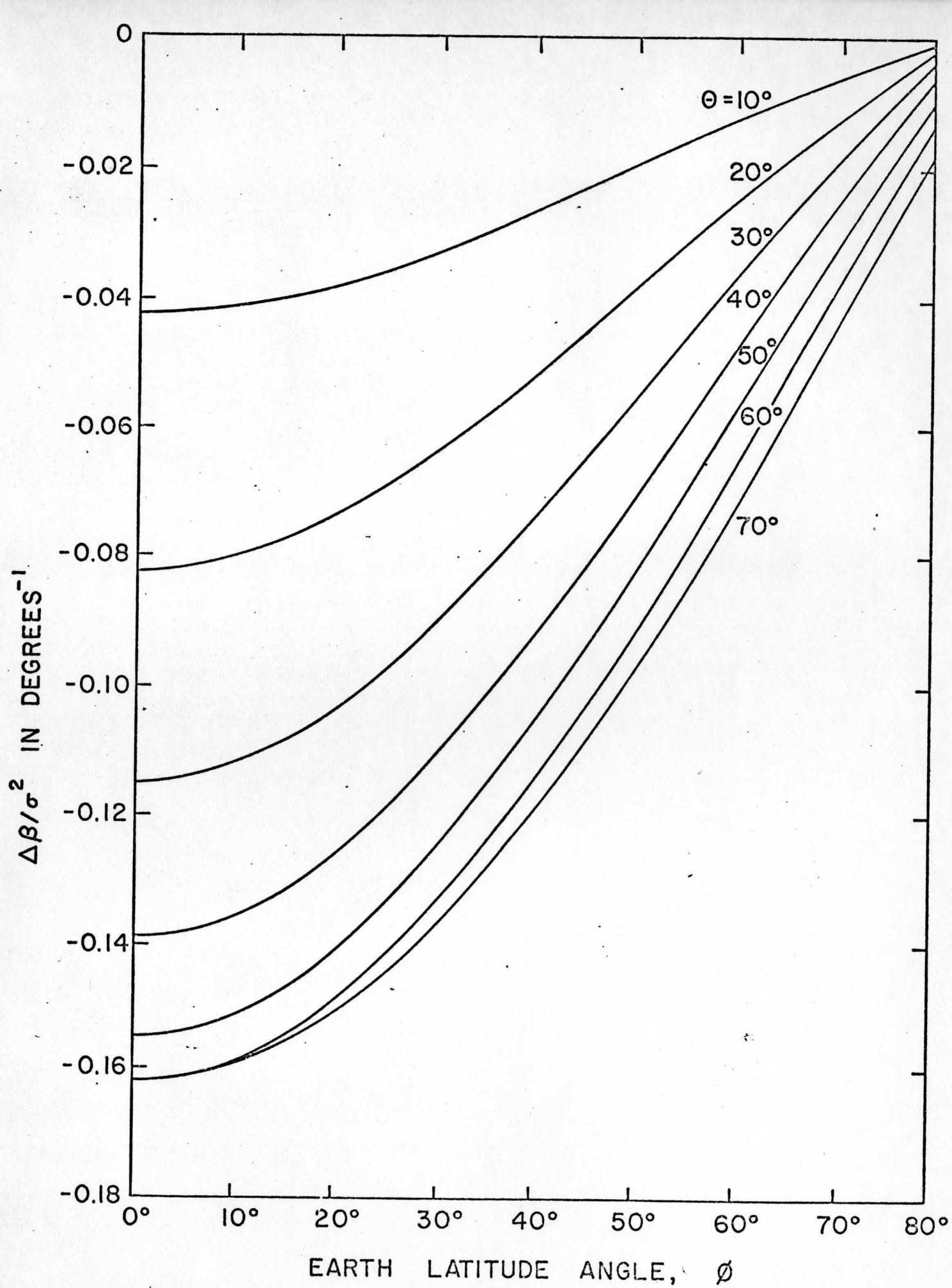
0
-0.02
-0.04
-0.06
-0.08
-0.10
-0.12
-0.14
-0.16
-0.18
Δβ/σ² IN DEGREES⁻¹
Θ=10°
20°
30°
40°
50°
60°
70°
0°
10°
20°
30°
40°
50°
60°
70°
80°
EARTH LATITUDE ANGLE, Ø

Fig. 12

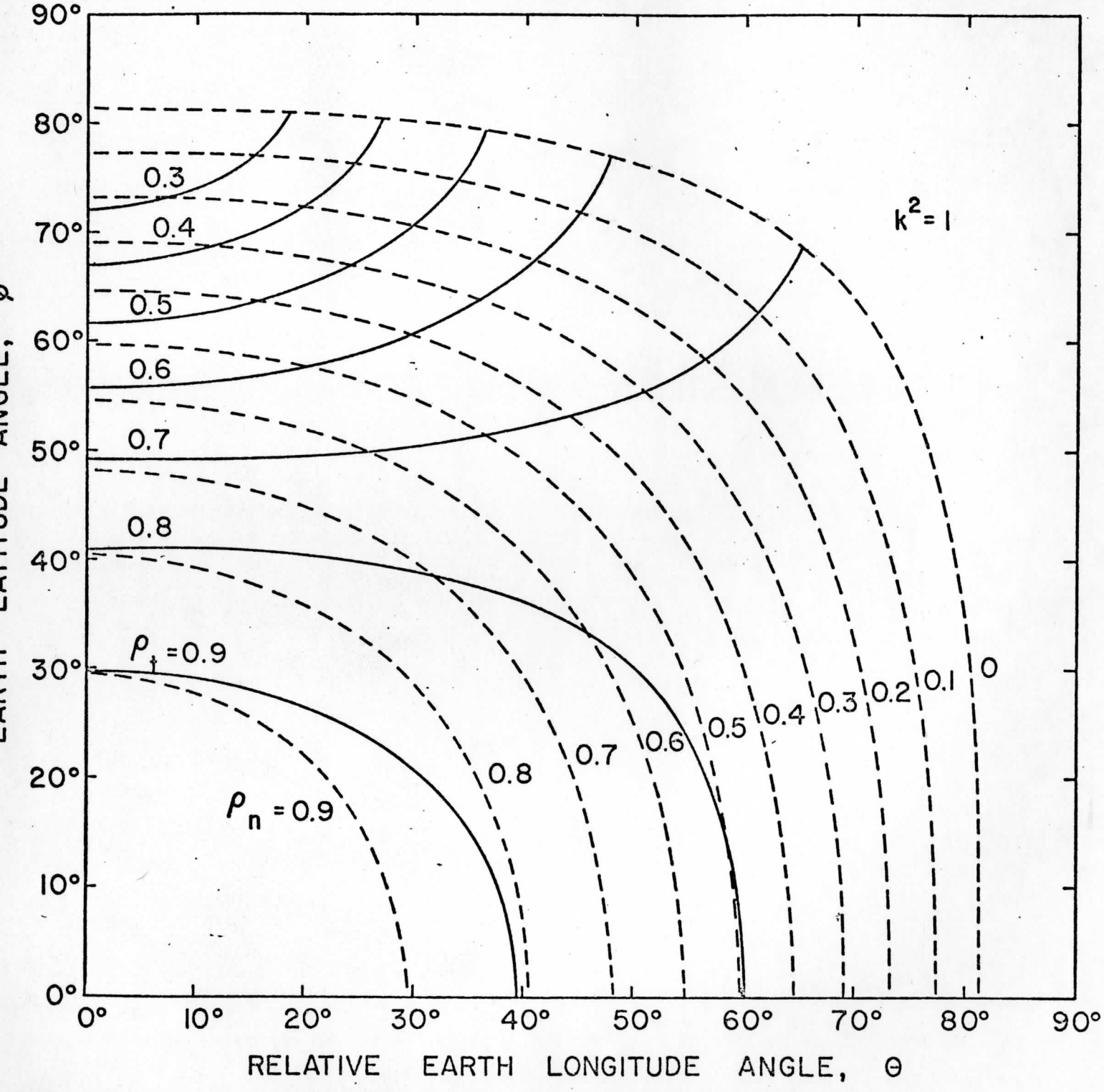
90°
80°
70°
60°
50°
40°
30°
20°
10°
0°
0°
10°
20°
30°
40°
50°
60°
70°
80°
90°
0.3
0.4
0.5
0.6
0.7
0.8
$k^2 = 1$
$\rho_t = 0.9$
$\rho_n = 0.9$
0.8
0.7
0.6
0.5
0.4
0.3
0.2
0.1
0
RELATIVE EARTH LONGITUDE ANGLE, Θ

Fig. 13

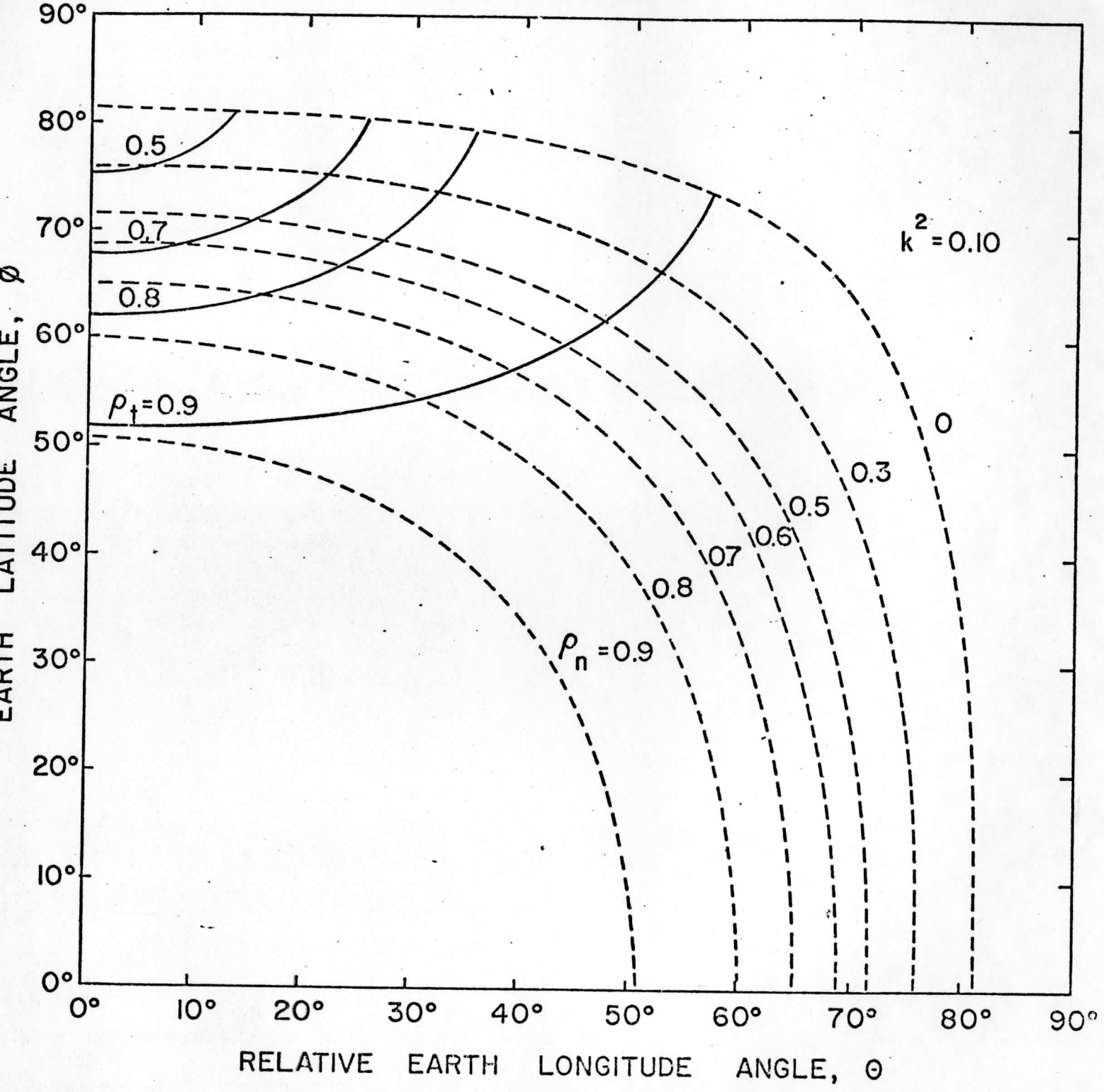
90°
80°
70°
60°
50°
40°
30°
20°
10°
0°
0°
10°
20°
30°
40°
50°
60°
70°
80°
90°
RELATIVE EARTH LONGITUDE ANGLE, θ
EARTH LATITUDE ANGLE, ø
$k^2$ = 0.10
0
0.3
0.5
0.6
0.7
0.8
$\rho_n$ = 0.9
0.5
0.7
0.8
$\rho_t$ = 0.9

Fig. 14

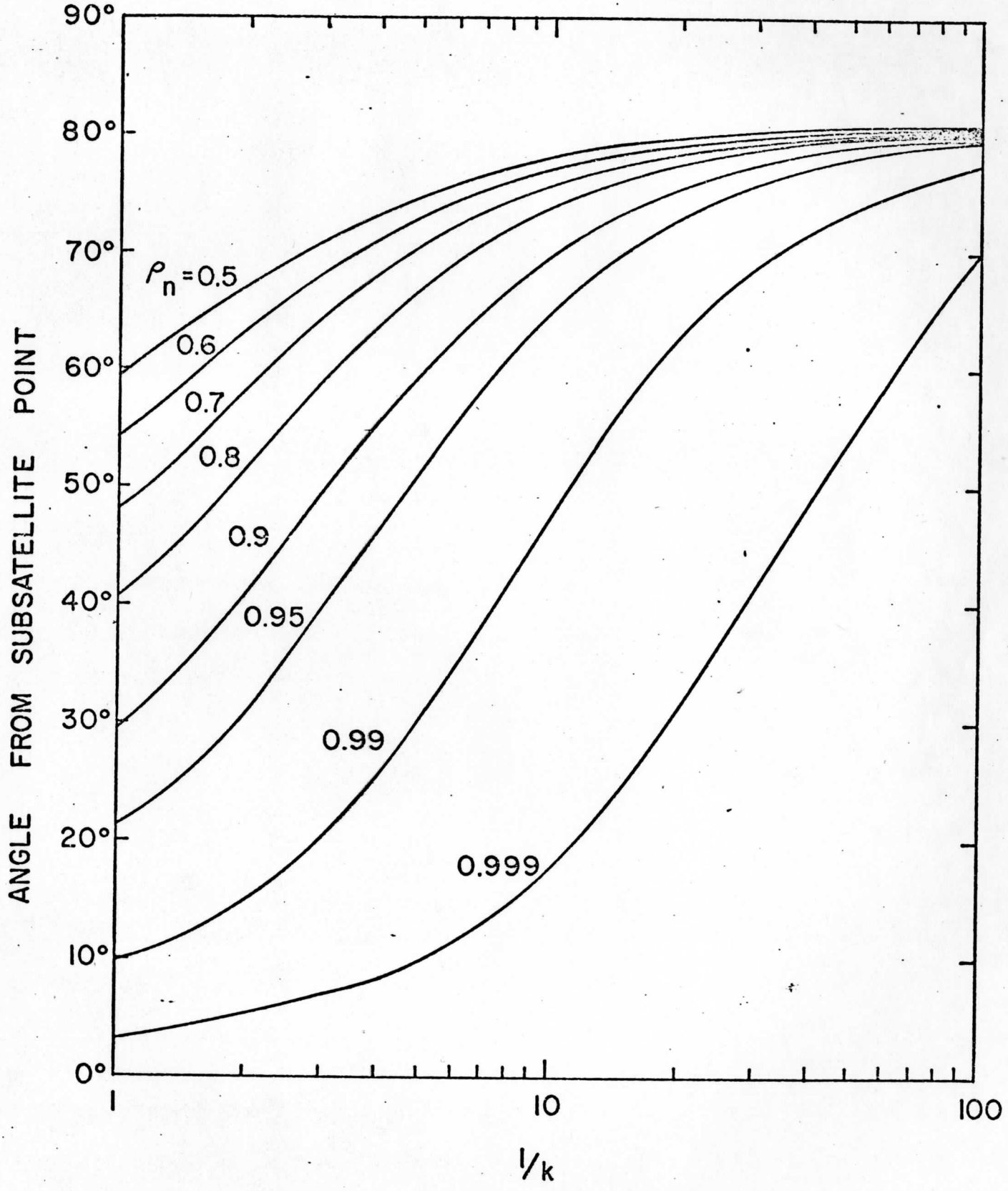
90°
80°
70°
60°
50°
40°
30°
20°
10°
0°
ANGLE FROM SUBSATELLITE POINT
$\rho_n$=0.5
0.6
0.7
0.8
0.9
0.95
0.99
0.999
1
10
100
1/k

Fig. 15

# QUANTIZATION OF PMT SIGNALS FOR METEOROLOGICAL SATELLITES

by

Ferrel G. Stremler

William R. Bryson

## Abstract

Quantization rules are examined for a satellite radiometer in the visual range. Effects of photomultiplier tube noise on the detection of cloud brightness levels are of particular interest because the expected radiance levels are high. Effects of area integration are considered to improve the probability of detection at high radiance levels.

Portions of this work were supported by NOAA under Grants NG-26-72, 3-35372.

F. G. Stremler is with the Space Science and Engineering Center and the Department of Electrical and Computer Engineering, University of Wisconsin, Madison, Wisconsin 53706.

W. R. Bryson is with the Department of Electrical and Computer Engineering, University of Wisconsin, Madison, Wisconsin 53706.

## I. INTRODUCTION

Visual scanners in early geostationary orbiting satellites used analog transmission techniques. However, more recent geostationary orbiting satellites (e.g., SMS-I) use digital techniques after quantizing the detected radiance levels, prior to multiplexing and transmission to a ground terminal. Some consequences of the quantization rules are investigated with an emphasis on how they affect various users of the data for meteorological purposes.

## II. SOME CHARACTERISTICS OF RADIOMETER SIGNALS AND NOISE

The detector commonly used for visual scanners is the photomultiplier tube (PMT). It is sensitive and reliable; it also has the characteristic that the detector noise power is proportional to the incoming radiance level. We assume that this detector noise is the limiting condition in the visual image transmission for a given spatial resolution.

Within this assumption, the detector noise characteristic significantly influences the quantization rule employed for the scanner. One commonly-used criterion is that the quantization rule should yield a uniform probability density function (pdf) at the output. In the absence of a priori information on the statistics of the expected signal, this criterion yields a square-root quantization rule for the PMT. Such a rule provides very good radiance level discrimination at the low levels at the expense of rather poor discrimination at the high levels. It is the type currently in use in such satellites as SMS-I.

An estimate of the statistics of typical data can be determined from photographs. A typical cloud pattern photograph taken on the Apollo VI mission is shown in Figure 1.* The transparency for this photograph was scanned

---

* Apollo VI transparencies are courtesy of the NASA Manned Spacecraft Center, Houston, Texas 77058.

and digitized (linear with respect to transmissivity) to 8-bit accuracy using 1024×1024 non-overlapping samples. The corresponding histogram, plotted to a logarithmic ordinate, is shown in Figure 2.

Based on studies of this and other photographs from the Apollo VI mission, it turns out that the bimodal shape of the histogram exhibited in Figure 2 is quite typical. The maximum at the lower levels results from the average radiance levels of the earth's surface. The maximum at the higher levels results from the radiance levels from the clouds. Variations in the brightness of the clouds and the darkness of the background may cause this pattern to spread out, incident lighting angle changes may cause level shifts, and the proportions of cloud cover to background area may result in relative changes in the proportions between maxima. However, the bimodal shape is typical throughout these variations. Important signal information is contained in the range near the maximum at lower levels if one is interested in details on the earth's surface and is contained in the range near the maximum at higher levels if one is interested in cloud pattern details. Obviously, the PMT detector is more ideally suited to the former than to the latter.

At this point one can apply a method described by Max [1] to determine the optimum quantizer rule. The method is based on a mean-square error criterion and the signal and noise statistics. The numerical procedure is not easy, however, and requires lengthy computational methods. In addition, not all input signal levels may be of equal importance to the user.

The latter point is particularly true in multiple-user systems. Some of the meteorological users of SMS-I data include visual photo classification and interpretation, correlation between successive frames for determination of relative cloud motions, and estimation of cloud brightness levels. The first use is quite tolerant of adjacent-level errors and coarse level increments at high radiance levels. Good performance for the second user is primarily

dependent on retention of good spatial (edge) response and moderately good level discrimination at the lower radiance levels to locate recognizable landmarks for frame alignments. The third user needs data in only the top 15-20% of the radiance level range and is quite tolerant of some loss of spatial detail. The latter is very susceptible to quantization choices which affect the higher levels. Because this is a problem with existing scanner systems, we shall investigate this problem in more quantitative detail.

## III. PROBABILITY OF ADJACENT-LEVEL ERROR

As a model for the PMT, we assume that the maximum useable signal level is 5000 times the minimum signal level (i.e., a 74 dB dynamic range). The noise is assumed to be an additive conditional Guassian random process with zero mean and a standard deviation of:

$$\sigma = k\sqrt{S} \tag{1}$$

where S is the signal level and k is a parameter of the PMT used.

A criterion of performance is the net probability of error resulting from detector noise. However, this will depend somewhat on the signal statistics, so instead we consider the probability of adjacent-level errors assuming equal a priori adjacent signal level probabilities. On a comparative basis, this will normally be proportional to the net probability of error for picture data.

For a linear quantizer with quantizing level increments of $\Delta$, the probability of an adjacent-level error, $p_\varepsilon$, is:

$$p_\varepsilon = 2\int_{\Delta/2}^{\infty} \frac{1}{\sqrt{2\pi}} \exp\left(\frac{-x^2}{2\sigma^2}\right) dx = \operatorname{erfc}\left(\frac{\Delta}{2\sqrt{2}\,\sigma}\right) \tag{2}$$

where $\sigma$ is given by Eq. 1. A graph showing $p_\varepsilon$ versus signal level for a 6-bit linear quantizer, within the above dynamic range restrictions, is shown in Figure 3.

A nonlinear quantizer whose level increments are tailored to yield a uniform output noise pdf for a PMT results in a square-root quantization rule.

For the above dynamic range and 6-bit quantization, each of the 64 levels will be spaced by approximately 1.25 $\sigma$ so that the resulting probability of adjacent-level error is, from Eq. 2, a constant given by:

$$p_\varepsilon = \text{erfc}(0.442) = 0.53 \quad . \tag{3}$$

This is also shown in Figure 3. Use of this nonlinear quantizer, however, results in only 6 quantizing steps within the top 15% of the range. This compares to 8 quantizing steps in the top 15% of the range using the linear quantizer. The probability of an adjacent-level error for the linear quantizer in this part of the range is (on a single-point basis) about 73% (cf. Figure 3).

## IV. AREA INTEGRATION VS NOISE EFFECTS

The square root quantization rule yields a uniform rms output detector noise level per quantization step and therefore a constant probability of adjacent-level error. At high radiance levels, however, the quantization steps become quite coarse and this may seriously degrade attempted measurements at these levels. On a single-point (i.e., single resolution element) basis it may be argued that the probability of error becomes so high as to make any meaningful measurements impossible anyway. This may be true for a single resolution element but such measurements as cloud brightness generally involve an area covering several resolution elements. Thus we next investigate what effect an area integration has on reducing the probability of error.

Relatively little information is available on this question [2,3] and so a closed-circuit television system was used to investigate.* Geometric shapes (mostly squares) with different numbers of resolution elements and of different contrast ratios were placed against a uniform background. This was used as the subject for a closed circuit television camera, as shown in Figure 4. A second

---

* The choice of a television system was a natural one because we currently use television monitors to display cloud patterns from geostationary orbiting satellites.

closed-circuit camera was focused on the screen of a television monitor which was tuned to an empty channel. This supplied a source of random noise in the measurement.

The outputs of both televisior cameras were added using a television waveform and then recorded on videotape. The S/N ratio was obtained by observing the composite picture signal level and the average noise level. The S/N ratio was set equal to zero at the point where the composite signal was not quite visible in the noise.

The resulting videotape was played back and stopped repeatedly using a "hold-frame" switch. This latter step eliminated time-integration effects in observations of fixed patterns in time-varying noise. The smallest detectable areas visible for each contrast ratio and S/N were recorded. The order was interchanged and many measurements were made. The results were averaged in an attempt to make the results as objective as possible. All measurements were made above the resolution limits of the system. The normalized results when plotted to a log-log scale are shown in Figure 5. A straight-line fit is also indicated.

These tests give an indication of the tradeoffs between area integration (i.e., target size) and detectable signal level. For example, the probability of adjacent-level error of the highest level using a 6-bit linear quantizer in additive conditional Guassian noise is, from Eqs. 1, 2:

$$p_\varepsilon = \text{erfc}(0.226) = 0.75 \quad . \tag{4}$$

Assuming that all of the noise which limits the detection is PMT detector noise, an increase in one order of magnitude in target area gives (cf. Figure 5) about a 3 dB improvement so that the new probability for adjacent-level error is:

$$p'_\varepsilon = \text{erfc}[\sqrt{2}\ (0.226)] = 0.65 \quad . \tag{5}$$

Thus the linear quantization rule can result in more information at the higher levels, even though the noise levels are high, as long as the patterns of interest are relatively large.

Finally, a word should be added about what may appear to be abnormally large probabilities of adjacent-level error. For a 6-bit linear quantization rule, the probability of an adjacent-level error is not detectable using film or television monitoring. For example, a high-quality film transparency is capable of reproducing about 5 bits of information per sample point while photograph prints and b/w television are more on the order of 3-4 bits. Also, the probability of errors for levels more removed than the adjacent levels decreases rapidly so that a picture with an adjacent-level probability of error of 50% actually may look quite good to the observer, particularly if the contrast is high. Therefore these measures are used on a comparative basis.

## V. CONCLUSIONS

Photomultiplier tube noise power increases linearly with input radiance level. Based only on noise statistics, a square-root quantization rule therefore yields a uniform output probability density. Signal statistics from broken cloud patterns result in a bimodal probability density. However, the variations from scene to scene make it difficult to design a system solely on the basis of the signal statistics. The square-root quantization rule gives best level discrimination in ranges where the data is of least meteorological value and penalizes attempted measurements in the upper part of the range. It has been shown that linear quantization in the upper part of the range results in higher noise levels on a single-point basis but area integration can be used to reduce the equivalent noise level.

## VI. REFERENCES

1. Max, J., "Quantizing for minimum distortion," IRE Trans. on Info. Theory, IT-6, 1960, 7-12.

2. Bates, A. D., "Measuring the discernibility of visual information," Proc. of Electronic Imaging Systems Symp., Palo Alto, Calif., April 1970.

3. Moore, T. H. and E. A. Reitz, "Effects of resolution and noise on picture quality," Proc. of Electronic Imaging Systems Symp., Palo Also, Calif., April 1970.

## Figure Captions

Figure 1. Altocumulus cloud pattern over the Pacific Ocean off the coast of Mexico; Apollo AS6-2-1429; scale is approximately 170×170 km.

Figure 2. Log-histogram plot of Apollo AS6-2-1429 data using 8-bit linear quantization and 1024×1024 samples.

Figure 3. Probability of adjacent-level error for a 6-bit linear and a 6-bit square-root-law quantizer in the presence of conditional Guassian PMT noise.

Figure 4. Experiment to determine area integration and S/N ratio tradeoffs.

Figure 5. Average number of resolution elements visible vs S/N ratio.

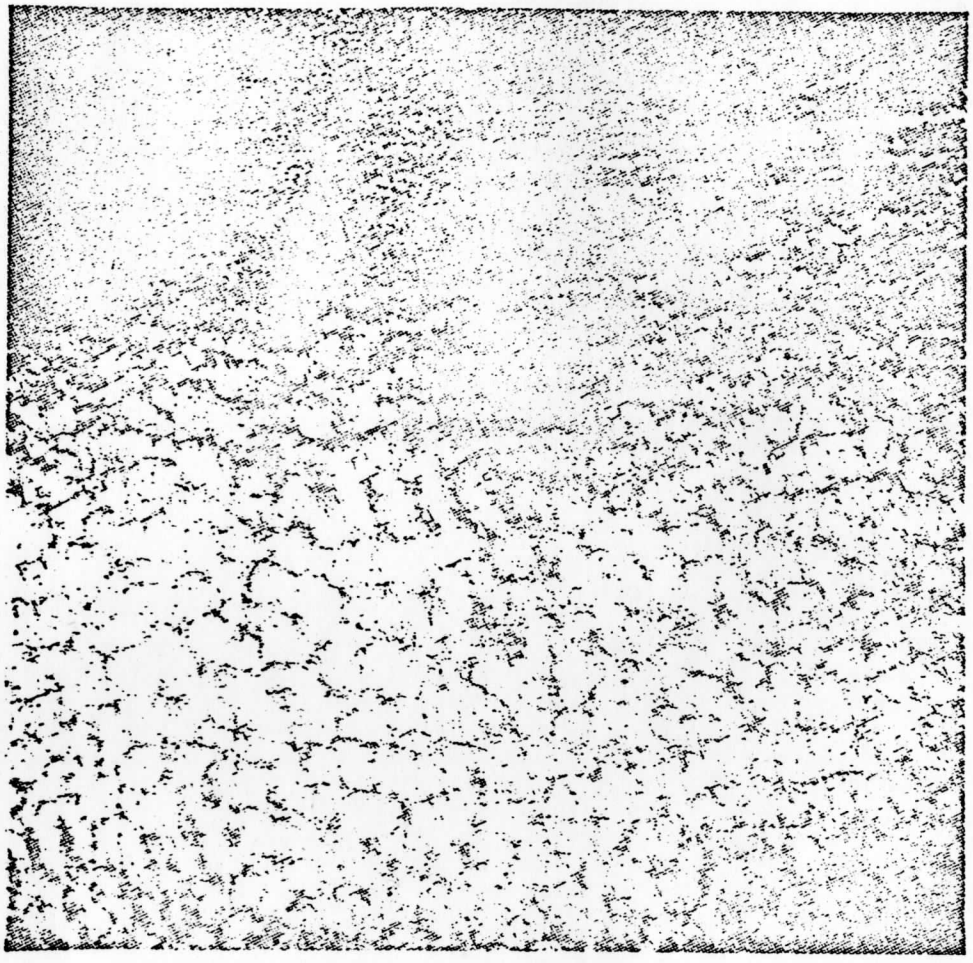

FIGURE 1

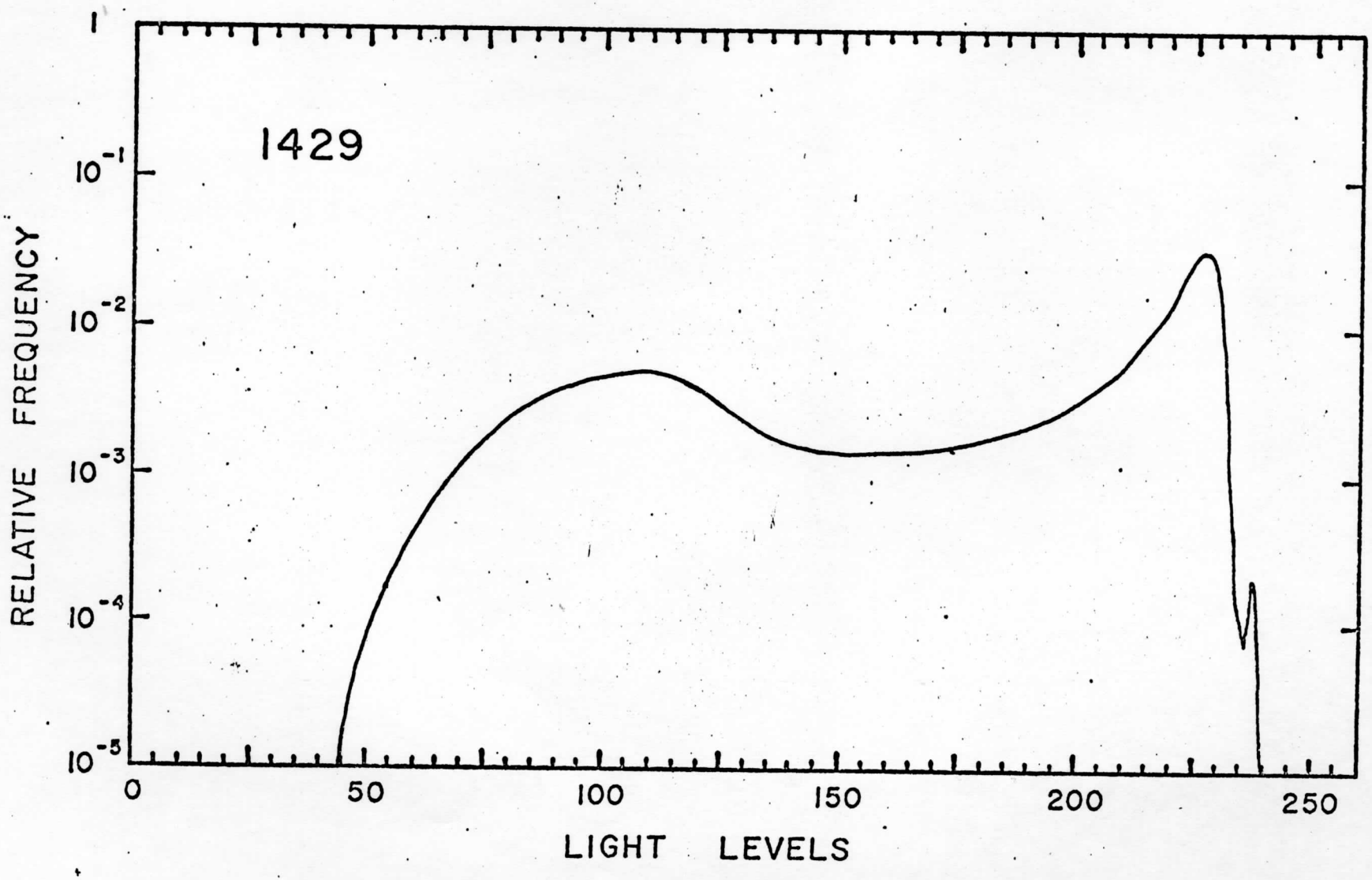
1429
RELATIVE FREQUENCY
1
$10^{-1}$
$10^{-2}$
$10^{-3}$
$10^{-4}$
$10^{-5}$
0
50
100
150
200
250
LIGHT LEVELS

FIGURE 2

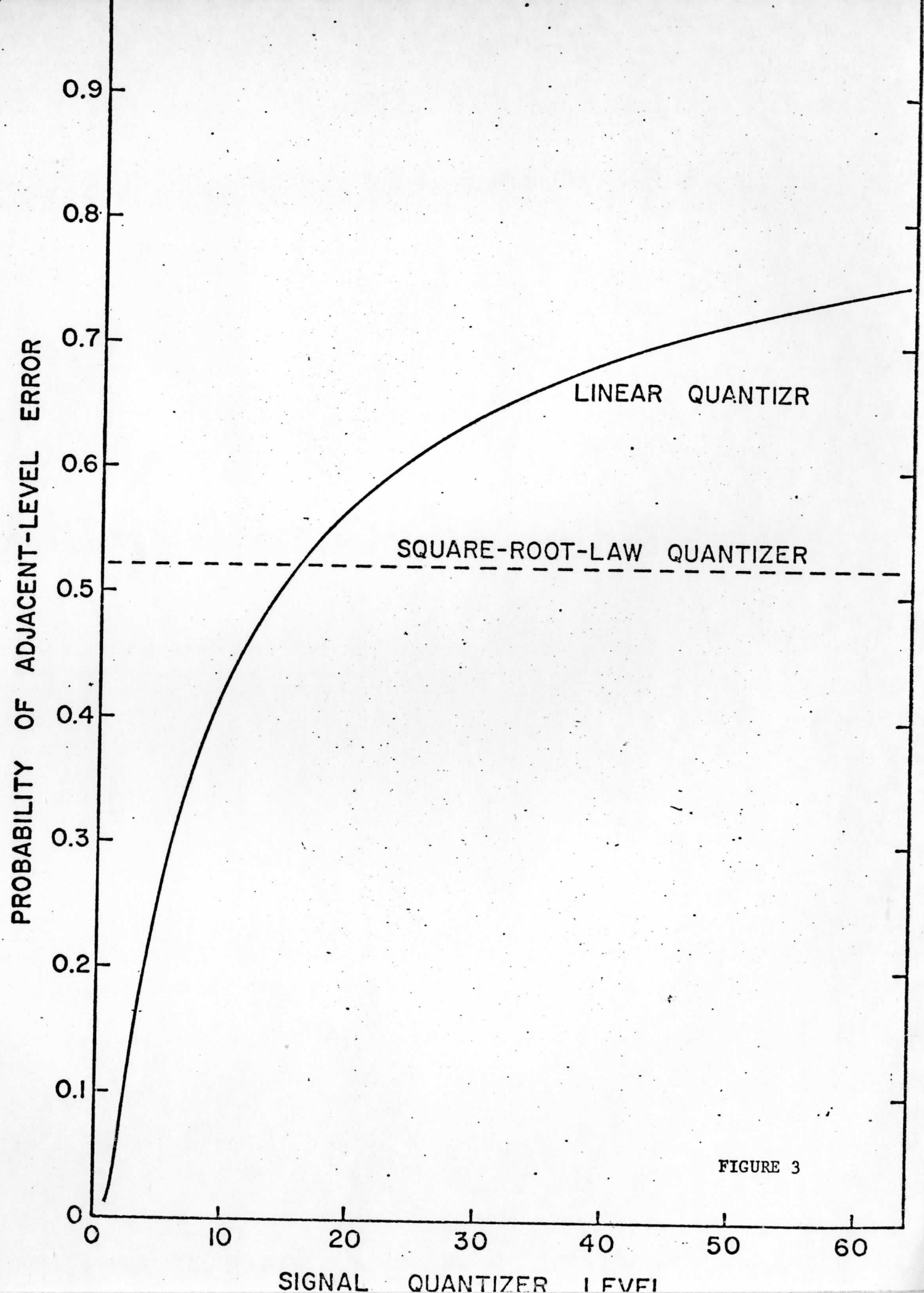
PROBABILITY OF ADJACENT-LEVEL ERROR
0.9
0.8
0.7
0.6
0.5
0.4
0.3
0.2
0.1
0
LINEAR QUANTIZR
SQUARE-ROOT-LAW QUANTIZER
0
10
20
30
40
50
60
SIGNAL QUANTIZER LEVEL

FIGURE 3

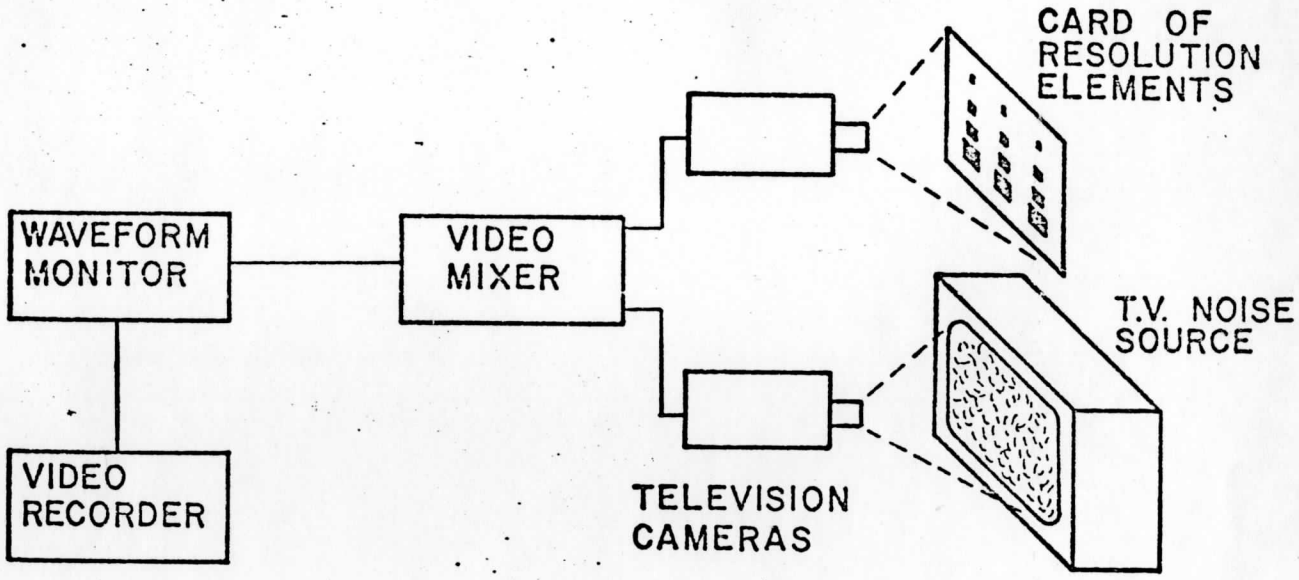
CARD OF
RESOLUTION
ELEMENTS
WAVEFORM
MONITOR
VIDEO
MIXER
T.V. NOISE
SOURCE
VIDEO
RECORDER
TELEVISION
CAMERAS

FIGURE 4

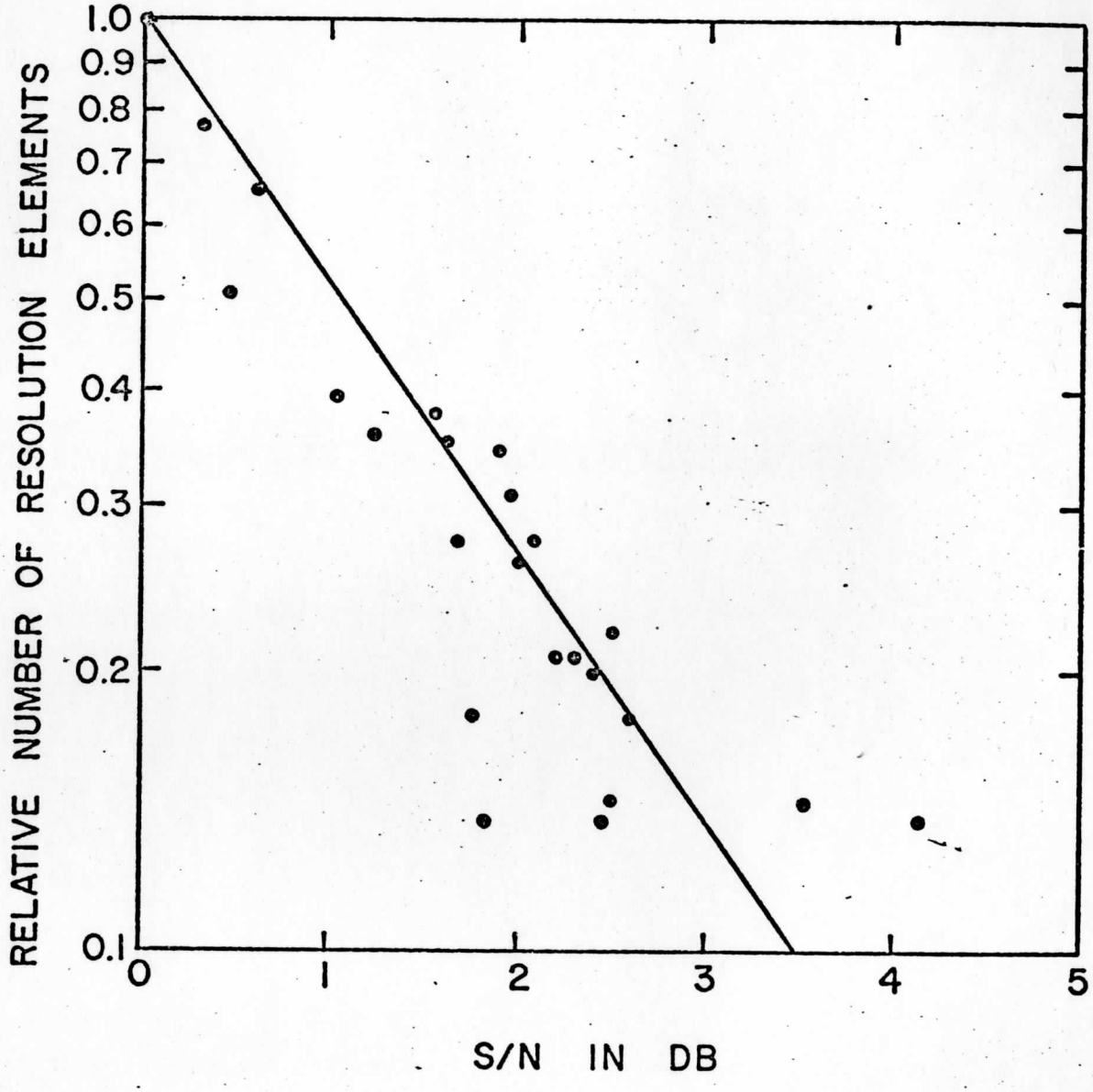
RELATIVE NUMBER OF RESOLUTION ELEMENTS
1.0
0.9
0.8
0.7
0.6
0.5
0.4
0.3
0.2
0.1
0
1
2
3
4
5
S/N IN DB

FIGURE 5